Università degli Studi di Ferrara

DOCTORAL COURSE IN
ENGINEERING SCIENCE

CYCLE XXXII

DIRECTOR Prof. TRILLO STEFANO

INFLUENCE OF ALLOYING ELEMENTS AND MELT TREATMENTS ON MICROSTRUCTURE AND MECHANICAL PROPERTIES OF THE AlSi7Mg ALLOY

Scientific/Disciplinary Sector (SDS) ING-IND/21

Candidate
Dott. Lattanzi Lucia

(signature)

Supervisor
Dott. Merlin Mattia

(signature)

Years 2016/2019

Ever tried, ever failed
No matter
Try again, fail again
Fail better

Worstward ho, 1983
Samuel Beckett

In memory of Professor Gabrielli

ABSTRACT

During the last decades, the employment of AlSi7 cast alloys in the automotive industry has significantly improved because vehicles result lighter and more eco-friendly. Thus it is crucial to increase the knowledge about the properties of such alloys in order to optimise them through precise control of chemical composition, well-performed melt treatments and tailored heat treatments. The present work focuses on the influence of alloying elements and melt treatments on microstructure and mechanical properties of the AlSi7Mg alloy.

The main alloying elements involved in the AlSi7Mg systems are magnesium (Mg), titanium (Ti), copper (Cu) and nickel (Ni) and each element has a specific effect on the microstructural features. They influence the solidification curves of the alloy, and some of them can also interact with the grain refiners and eutectic modifiers added for melt treatments. In light of this, thermal analysis is useful to record the cooling curves and to detect temperature changes during solidification. These parameters, when carefully interpreted, help to predict the success of alloying additions and melt treatments, and thus to define the expected microstructure.

The improvement of the mechanical properties of the alloy often relies on the addition of Cu and Ni as alloying elements. The first significantly increases the tensile properties before and after heat treatment, and the second provides excellent high-temperature mechanical properties to the alloy. *In-situ* fatigue tests in the scanning electron microscope (SEM) coupled with digital image correlation (DIC) and Charpy impact tests on Cu-added and Ni-added AlSi7Mg alloys, respectively, help to deepen the role played by these elements during crack nucleation and propagation. Cu strengthens the primary α-aluminium matrix via solid solution and crack propagation remains trans-granular and trans-dendritic as the copper content increases. Ni, on the other hand, forms brittle phases that do not influence the as-cast mechanical properties but significantly affect them after T6 heat treatment.

SOMMARIO

Nel corso degli ultimi decenni l'impiego di leghe di alluminio AlSi7Mg è notevolmente aumentato nell'ambito dell'autoveicolo, in quanto le vetture ne risultano alleggerite e più ecologiche. Pertanto è di cruciale importanza approfondire le conoscenze riguardo le proprietà di tali leghe in modo da poterle ottimizzare tramite preciso controllo della composizione chimica, trattamenti della lega liquida ben operati e trattamenti termici sviluppati *ad hoc*. Il presente lavoro riguarda l'influenza che gli elementi in lega ed i trattamenti della lega liquida hanno sulla microstruttura e sulle proprietà meccaniche della lega AlSi7Mg.

I principali elementi alliganti coinvolti nel sistema AlSi7Mg sono magnesio (Mg), titanio (Ti), rame (Cu) e nichel (Ni), e ciascun elemento ha uno specifico effetto sulla microstruttura. Tali elementi modificano le curve di solidificazione della lega, ed alcuni di essi possono interagire con gli agenti affinanti e modificanti presenti per i trattamenti della lega liquida. Alla luce di ciò, l'analisi termica risulta un utile strumento per acquisire le curve di raffreddamento e rivelare variazioni di temperatura nel corso della solidificazione. Tali parametri, quando opportunamente interpretati, aiutano a predire l'avvenuta aggiunta di elementi alliganti e la riuscita dei trattamenti della lega, e dunque a definire la microstruttura attesa.

Il miglioramento delle proprietà meccaniche della lega spesso si basa sull'aggiunta di rame e nickel come elementi alliganti. Il primo incrementa significativamente le proprietà a trazione prima e dopo trattamento termico, ed il secondo fornisce delle eccellenti proprietà meccaniche a temperature elevate. Prove di fatica *in situ* nel microscopio elettronico a scansione (SEM) abbinate alla *digital image correlation* (DIC) e prove di resilienza Charpy rispettivamente su leghe AlSi7Mg additivate con rame e nichel aiutano ad approfondire il ruolo giocato da tali elementi nel corso di nucleazione e propagazione della cricca. Il rame rinforza la matrice di alluminio primario per soluzione solida e la propagazione della cricca si mantiene transgranulare e trans-dendritica all'aumentare del tenore di rame in lega. Il nichel invece porta alla formazione di fasi fragili che non hanno influenza sulle proprietà meccaniche allo stato *as-cast* ma le inficiano dopo trattamento termico T6.

ACKNOWLEDGEMENTS

My sincere gratitude goes to:

Professor Gian Luca Garagnani and Dr Mattia Merlin for the warm welcome in Ferrara and for the opportunity of this doctoral course.

All the other professors and colleagues of the *Aldo Daccò* Metallurgy and Corrosion research group for scientific support and nice company: Professor Cecilia Monticelli, Dr Andrea Balbo, Professor Vincenzo Gabrielli, Vincenzo Grassi, Dr Federica Zanotto, Dr Chiara Soffritti, Dr Annalisa Fortini, Maverick Giovagnoli and Mahla Seyedi. Gabriele Bertocchi of the Department of Chemistry for XRD experimental work.

Master students Maverick Giovagnoli and Mario Lucci Manni for scientific growth.

Stefano Pirletti and Stefano Morè Spreafico of Mario Mazzucconi Foundry for good cooperation and experimental support.

Professor Salem Seifeddine and Professor Ehsan Ghassemali of the Jönköping University for the opportunity of the visiting period at the Department of Materials and Manufacturing. Toni Bogdanoff for excellent collaboration and scientific discussion. Dr Fengxiang Lin for support with *in-situ* SEM experimental work.

All other colleagues and friends from the Jönköping School of Engineering for the warm welcome in Sweden and the superb work environment.

Professor Marisa Di Sabatino Lundberg of the Department of Materials Science and Engineering at the Norwegian University of Science and Technology, Dr Daniele Casari of Brembo, Professor Emanuela Cerri and Dr Maria Teresa Di Giovanni of the Department of Engineering and Architecture at the University of Parma for good cooperation.

Professor Andrea Zambon of the Department of Management and Engineering at the University of Padova, for the invaluable teachings that accompany my everyday work.

Family and friends, for constant love, patience and support.

PREFACE

The present doctoral thesis is the result of three years of study and research activities, carried out at the University of Ferrara (Ferrara, Italy) from November 2016 to October 2019. Part of the experimental work was carried out at the Department of Engineering in Ferrara and the Mario Mazzucconi Foundry (Ponte San Pietro, Italy). Part of the experiments and research activity was carried out at the Jönköping University (Jönköping, Sweden) in cooperation with the Department of Materials and Manufacturing, during a visiting period from August 2018 to February 2019.

Dr Mattia Merlin at the Department of Engineering in Ferrara was the main supervisor. Professor Salem Seifeddine and Professor Ehsan Ghassemali hosted the visiting period at the Department of Materials and Manufacturing of the Jönköping University.

The research activity focused on the effect of the addition of alloying elements, Cu and Ni specifically, and the melt treatments, in particular grain refining and Sr modification, on the microstructural features of AlSi7Mg cast aluminium alloys.

Chapter 1 is a literature survey about the main topics of the research work and reports the principal theories and experimental results obtain in the last decades.

Chapter 2 gathers the results of experiments about different levels of grain refining at different holding times, and the interaction of alloying elements with Sr modification. The experimental works concerning melt treatments were performed at the Tekal foundry (San Giovanni Teatino, Italy) of the Mazzucconi Group. The research work led to the publication of the following articles:

- L. Lattanzi, A. Fortini, M. Giovagnoli, M. Merlin, S. Pirletti, S. Morè Spreafico, G.L. Garagnani, *Thermal Analysis for the Prediction of Grain Refinement: An Experimental Investigation on an AlSiMg Foundry Alloy*, Materials Science Forum, Vol. 941, pp. 1029-1034, 2018, *doi:10.4028/www.scientific.net/MSF.941.1029*
- L. Lattanzi, A. Fortini, M. Giovagnoli, M. Merlin, *Influence of Mg and Ti on both eutectic solidification and modifying efficiency in Sr-modified Al-7Si cast alloys*, La Metallurgia Italiana, Vol. 2, pp. 5-15, 2018

- A. Fortini, L. Lattanzi, M. Merlin, G.L. Garagnani. *Comprehensive evaluation of modification level assessment in Sr-modified aluminium alloy*, 2018, International Journal of Metalcasting, 12, 697-711, *https://doi.org/10.1007/s40962-017-0202-3*

The following manuscript was awarded the "Aldo Daccò" 2019 award:

- A. Fortini, L. Lattanzi, S. Pirletti, M. Merlin. *On the interaction between alloying elements and Sr modification in AlSi7 alloys*.

The experimental results on grain refining and Sr interaction with alloying elements were also presented at the following conferences:

- Junior Euromat 2018. Budapest (Hungary), 8-12nd July 2018 - oral presentation
- Thermec'2018. Paris (France), 8-13rd July 2018 - poster

Concerning the effect of alloying elements, the addition of different Cu contents to AlSi7Mg alloys was performed at the JU-Cast experimental foundry (Jönköping, Sweden) of the Jönköping University. Different Cu contents lead to variations in the microstructural features and can influence the crack propagation behaviour. The experimental findings of this activity constitute Chapter 3 of the present work. The activity resulted in the following article:

- T. Bogdanoff, L. Lattanzi, M. Merlin, E. Ghassemali, S. Seifeddine, *The influence of Cu additions on crack initiation and propagation in an Al-Si-Mg Alloy*. Manuscript ready for submission.

Chapter 4 concerns a side project carried out during the doctoral studies, in the frame of a collaboration with the Norwegian University of Science and Technology (Trondheim, Norway). The collaboration started in 2015 and regarded the evaluation of tensile and impact properties of Ni-added AlSi7Mg alloys, both at high and room temperature. The room temperature mechanical properties were tested in Ferrara in 2016, and the activity resulted in the supervision of the following master theses:

- Maverick Giovagnoli (October 2017), *Valutazione dell'effetto del nichel sulla microstruttura e sulle proprietà meccaniche di una lega di alluminio A356*. Supervisor: M. Merlin. Co-supervisors: A. Fortini, L. Lattanzi.
- Mario Lucci Manni (December 2018), *Effect of Ni addition on the impact properties of an A356 alloy: fractographic, thermal and microstructural analyses*. Supervisors: M. Merlin, M. Di Sabatino Lundberg. Co-supervisors: L. Lattanzi, M. Giovagnoli.

The results of these activities were presented at the Italian Metallurgy 37th National Congress, held in Bologna (Italy) on the 12-14th September 2019.
The collaboration with the Norwegian University of Science and Technology and the University of Parma (Parma, Italy) on the same topic led to the publication of the following article:

- L. Lattanzi, M.T. Di Giovanni, M. Giovagnoli, A. Fortini, M. Merlin, D. Casari, M. Di Sabatino, E. Cerri, G.L. Garagnani, *Room temperature mechanical properties of A356 alloy with Ni additions from 0.5 wt to 2 wt %*, Metals, Vol. **8**, pp. 224-238, 2018, *doi:10.3390/met8040224*

Besides the doctoral research activities, a project on the fatigue behaviour of high-pressure die-cast Al alloys was developed in collaboration with the Department of Management and Engineering at the University of Padova (Vicenza, Italy). The preliminary results were presented at the 3rd International Symposium on Fatigue Design and Material Defects, held in Lecco (Italy) on the 19-22nd September 2017.

- L. Lattanzi, A. Fabrizi, A. Fortini, M. Merlin, G. Timelli. *Effects of microstructure and casting defects on the fatigue behavior of the high-pressure die-cast AlSi9Cu3(Fe) alloy*, 2017, Procedia Structural Integrity, 7, 505-512, *doi:10.1016/j.prostr.2017.11.119*

TABLE OF CONTENTS

CHAPTER 1

CHAPTER 2

CHAPTER 3

CHAPTER 4

CONCLUDING REMARKS AND FUTURE DEVELOPMENTS

NOMENCLATURE

ACRONYMS

AD	Anderson-Darling
AGS	average grain size
APT	atom probe tomography
CP	commercial purity
CT	compact – tension
DCP	dendrite coherency point
DIC	digital image correlation
EBSD	electron backscattered diffraction
ED	equivalent diameter = $(4\cdot\text{area}/\pi)^{1/2}$ [μm]
EDS	energy dispersive spectroscopy
FIB	focused ion beam
FOV	field of view
GRF	growth restriction factor
HP	high purity
HV	Vickers hardness
IA	image analysis
IIT	impurity induced twinning
OES	optical emission spectroscopy
OM	optical microscope
PDF	probability density function
RTPRE	restricted twin-plane re-entrant edge
SDAS	secondary dendrite arm spacing
SEM	scanning electron microscope
SF	shape factor = $\text{length}^2/4\pi\cdot\text{area}$
TA	thermal analysis
TPRE	twin-plane re-entrant edge
TEM	transmission electron microscopy
UTS	ultimate tensile strength
WDS	wavelength dispersive spectroscopy
XRD	x-ray diffraction
μ-XRF	micro x-ray fluorescence
YS	yield strength

GREEK LETTERS

α	primary aluminium
	thermal diffusivity [W/m·K]
β	Mg_2Si
	Al_5FeSi
Δ	range
ε	Al_3Ni
ε_{fr}	deformation of fracture
θ	Al_2Cu
ϱ	density [kg/m^3]

LATIN LETTERS

A	surface area [m^2]
	accepted (subscript)
c_p	specific heat [J/kg·K]
C	circularity = $4\pi \cdot area/perimeter^2$
D	discarded (subscript)
e	percentage elongation
E	Young's modulus [GPa]
ED*	image analysis parameter defined in Equation (2.6) [μm]
H	hardness [GPa]
L	liquid
m	mass [kg]
Q	$Al_5Mg_8Cu_2Si_6$
	latent heat of solidification [J]
R	roundness = $4 \cdot area/\pi \cdot length^2$
t	total (subscript)
T	Al_9FeNi
T_E	eutectic temperature [°C]
T_N	nucleation temperature [°C]
T_M	minimum temperature [°C]
T_G	growth temperature [°C]
W	image analysis parameter defined in Equation (2.7) [μm]

LIST OF FIGURES

CHAPTER 1

THEORETICAL BACKGROUND

CHAPTER 2

GRAIN REFINING AND Sr MODIFICATION

CHAPTER 3

Cu ADDITION

CHAPTER 4

***SIDE PROJECT* - Ni ADDITION**

LIST OF TABLES

CHAPTER 1

THEORETICAL BACKGROUND

CHAPTER 2

GRAIN REFINING AND Sr MODIFICATION

CHAPTER 3

Cu ADDITION

CHAPTER 4

SIDE PROJECT - Ni ADDITION

CHAPTER 1

THEORETICAL BACKGROUND

The present research focuses on the AlSi7Mg family of alloys, the most employed for automotive components (e.g. suspension systems) that operate at room temperature. The study considers alloys with various levels of grain refinement and modification and different amounts of alloying elements.

The present chapter concerns the theoretical background useful to discuss and support the experimental results obtained during the research work. First, a general introduction to Al-Si foundry opens the chapter. Principles of grain refining and chemical modification of AlSi alloys will follow, along with the description of the role of Cu as an additional alloying element. An overview of thermal analysis and its application in the aluminium foundry closes the chapter.

1.1 Al-Si CAST ALLOYS

Among Al foundry alloys, Al-Si ones are the most used in automotive and aircraft applications because of their excellent castability, high strength to weight ratio and moderate cost. Commercial Al-Si casting alloys have Si concentration in the range of 5 to 23 wt.%. The addition of Si increases the fluidity and decreases the solidification shrinkage, resulting in an increased castability. It also increases both strength and stiffness but affects the ductility. In the Al-Si system, a eutectic reaction occurs at 577 °C and 11.7 wt.% of Si, as depicted in Figure 1. 1. The eutectic consists of Si lamellae immersed in an aluminium matrix. There are three different families of alloys, depending on the Si content: hypoeutectic alloys, with a microstructure consisting in dendrites of primary α-Al and interdendritic eutectic; eutectic alloys; and hypereutectic alloys, with primary Si crystal in a eutectic matrix. Hypoeutectic and eutectic alloys, with Si concentration that ranges between 5 and 12 wt.%, are widely employed in the automotive industry, going from cylinder heads and engine blocks (AlSi10 and AlSi12 alloys) to wheels and suspension systems (AlSi7 and AlSi9 alloys). Applications that require important wear properties, such as pistons and cylinder liners, need the employment of hypereutectic alloys.

Favourable mechanical properties depend on precise control of the parameters that influence the solidification process. In recent years several studies concerned the improvement of the mechanical characteristics of Al-Si cast alloys by the addition of alloying elements, by conveniently performed liquid alloy treatments and by the optimization of heat treatment parameters.

Besides Si, the addition of specific alloying elements can modify the mechanical properties of Al-Si casting alloys. Cu and Mg are commonly added to increase the strength of the alloy, at expenses of ductility. This effect is due to the precipitation of intermetallic compounds and the matrix strengthening by solid solution. Specific heat treatments that lead to the precipitation of fine Cu and Mg compounds enable to gain the highest contribution to increase strength. The addition of Ni is required for high-temperature applications, as its intermetallic compounds increase the high-temperature mechanical properties. On the other hand, Fe is often regarded as impurity because it forms elongated and brittle intermetallic compounds that affect ductility.

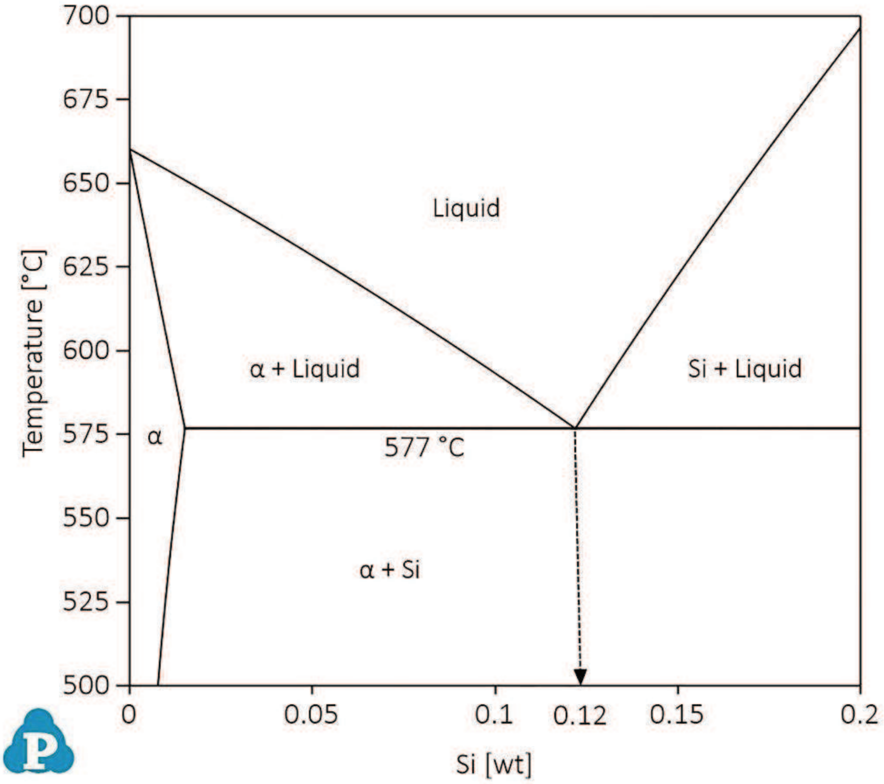

Figure 1. 1 – Al-Si phase diagram

Conventional treatments performed on the liquid alloy are grain refining, eutectic modification and degassing. Grain refining yields several benefits since a refined grain size results in uniform mechanical properties throughout the material. As the grain size of a casting decreases, strength and fatigue life significantly increase. The distribution of secondary phases and porosity is also on a fine scale. Better feeding of the casting is also a result of grain refinement. The eutectic modification aims to promote a change of eutectic Si morphology, from large brittle flakes to a fibrous coral structure. The fracture mode in the eutectic portion of the modified casting is ductile, and the elongation and the tensile strength increase substantially. Degassing is crucial to expel the hydrogen, and other gases embedded in the melt and thus avoid later nucleation of bubbles during solidification. Degassing helps to control the amount and the dimension of defects, while grain refining and modification have a powerful influence on the microstructural features of the alloy. Given the importance of successful grain refining and eutectic modification, because of their consequent effect on mechanical properties, it is crucial to have a high degree of control to assess the melt quality before casting. The study of cooling curves, coupled with density measures and chemical analysis, can be a useful tool.

1.2 LIQUID ALLOY TREATMENTS

1.2.1 Grain refinement of primary α-Al

The inoculation of Al alloys to control the grain size is a common practice in the Al foundry. The addition of grain refiners, mainly master alloys containing potent nucleant particles, promotes the formation of a fine equiaxed microstructure by the suppression of columnar and twin columnar growth mechanisms. Fine equiaxed grains determine a distributed microporosity and intermetallic particles and thus lead to improved mechanical properties. The most used master alloys are from the Al-Ti, Al-B or Al-Ti-B systems, the latter coming from the grain refining practice of wrought Al alloys. The main drawback of refining is the fading phenomenon that affects the agents added to the melt. The refining effect decreases during the time, and a new addition of refiners becomes necessary. Despite the widespread of grain refinement and the extensive literature on the topic, the nucleation mechanism has been a very much-debated topic.

1.2.1.1 Grain refinement of pure Al

Two main approaches characterise the development of the nucleation theories proposed since the 1950s [1] and are related to the two primary compounds present in the Al-Ti-B system. In particular, the earlier literature focused on the genesis of the grain, whether via a peritectic reaction involving Al_3Ti or on favourable sites for heterogeneous nucleation. The particle theory suggests the nucleation of α-Al grains on the borides TiB_2, AlB_2 and $(Ti,Al)B_2$, while the phase diagram theory relies on the peritectic reaction that involves the liquid and Al_3Ti. A brief description of the nucleation theories proposed in the literature will follow.

Particle theory – it was formulated by Cibula in 1949-52 [2], [3] as the carbide-boride theory. Cibula suggested that nucleation occurs on either TiB_2, added to the melt by the master alloy, or TiC, formed by the reaction of the residual carbon in the melt. This theory later evolved in the metastable boride theory, given the instability of the carbide in Al melts. All the borides TiB_2, AlB_2 and the metastable $(Ti,Al)B_2$ should show the same nucleating behaviour since they are isomorphous and hexagonal with very similar lattice parameters. Besides, $(Ti,Al)B_2$ is formed by the replacement of Ti atoms by Al atoms in the TiB_2 lattice. Some authors affirm that the metastable boride converts to TiB_2 on long holding times, while other authors suggest that it promotes the nucleation of Al_3Ti. The fading of the refining effect is due to the settlement of boride particles on prolonged holding times. The weak points of this theory are the metastability of the boride and its refining effect, both not deepened yet.

Phase diagram theory – it was proposed by Crossley and Mondolfo in 1950 [4] and tried to explain how Al_3Ti could be the active nucleant in hypo-peritectic compositions. In the Al-Ti system (Figure 1. 2), the peritectic reaction in Equation (1. 1) occurs at the minimum content of 0.15 wt.% Ti and 665 °C:

$$L + Al_3Ti \rightarrow \alpha \qquad (1.\ 1)$$

For this reason, Al_3Ti is often considered a powerful nucleant for Al. Besides, experimental results reported Al_3Ti at the centre of grains while in the master alloys borides were found pushed to the grain boundaries, and thus considered poor nucleants or less effective than the titanium aluminide Al_3Ti [5]. Marcantonio and Mondolfo suggested at first that the addition of B causes a shift of the peritectic point towards low Ti contents as 0.05 wt.%, and stabilises the presence of Al_3Ti at low Ti contents [1].

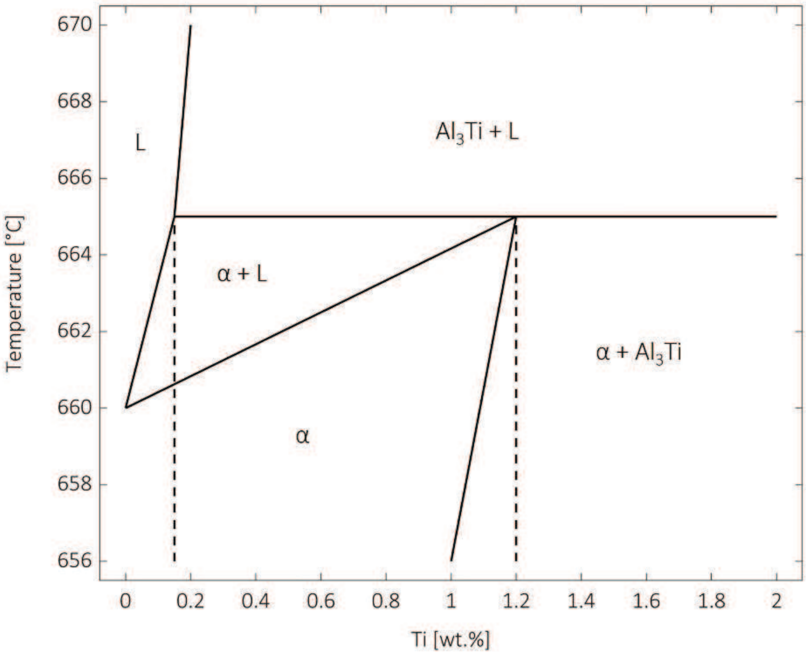

Figure 1. 2 – Al-rich corner of the Al-Ti phase diagram

Nevertheless, Sigworth and Jones later demonstrated that B has virtually no effect on the Al-Ti phase diagram [1]. Fade is due to the dissolution of the titanium aluminide over time, and it is unrecoverable. The dissolution time seems to depend on the holding temperature and the particle size. Several studies agree that Al_3Ti can dissolve in less than 1 minute or last up to 30 minutes in the molten bath, depending on particle size, holding temperature and Ti content. The main problem of the phase diagram theory concerns the stability of titanium aluminide in the bath for long enough time to act as a nucleation site for Al [1].

Hypernucleation theory – formulated by Jones in 1985, hypothesises that minimal amounts of B and Ti have a disproportionate effect on the grain size of Al [1], [5]. By calculating the activities of Ti in the melt and TiB_2, the author showed that Ti atoms segregate to the boride/melt interface creating a stabilised layer of atoms. This liquid layer should have the atomic array of the solid solution of Ti and Al (stable pseudocrystal) and on cooling it would permit the growth of primary α-Al without undercooling. Although it seems promising, this theory lacks experimental evidence and assumes the occurrence of an activity gradient, due to the addition of TiB_2 particles, that is not possible at equilibrium.

Peritectic hulk theory – presented by Bäckerud *et al.* in 1991 [6], it accepts that Al_3Ti has better nucleant behaviour than TiB_2 and involves a rather complicated mechanism. This theory assumes that titanium diboride covers the aluminide and protects it from early dissolution. Diffusion proceeds through the boride shell and the aluminide slowly dissolves, leaving a liquid of peritectic composition inside the shell. The peritectic reaction occurs, and Al can then grow. The aspect that does not fit with experimental evidence is about the formation of the TiB_2 shell on Al_3Ti. In fact, according to this theory, the borides should dissolve in the melt faster than the dissolving aluminides and reprecipitate on them. Nevertheless, later studies demonstrated that borides are very stable compared to Al_3Ti in Al melts with low Ti contents [7]. Hence, the peritectic hulk mechanism does not operate in grain refining.

Duplex nucleation theory – it was proposed by Mohanty and Gruzleski in 1995 [5] and experimentally supported, to a degree, by Schumacher and Greer [8]. Mohanty and Gruzleski [5] reported that no grain refinement was observed after addition of TiB_2 and without excess Ti. With the addition of excess Ti, grain refinement occurred, and TiB_2 particles were at the grain centres. An Al_3Ti layer formed on the surface on titanium diborides and eased the formation of primary α-Al. The authors suggested that the formation of the aluminide is due to a concentration gradient of Ti toward the TiB_2 particle. Similarly to the hypernucleation theory, Sigworth [9] claims that the activity gradient would be against the laws of thermodynamics. Nevertheless, Schumacher and Greer characterised the orientation relationships between the phases involved in the subsequent precipitation, reported in Table 1. 1, and suggested that the Al_3Ti layer could form due to adsorption effects at the boride/aluminide interface [1].

Table 1. 1 – The orientation relationships between the phases involved in the duplex nucleation theory [1]

TiB_2	Al_3Ti	α-Al
$<11\bar{2}0>\{0001\}$	<110>{112}	<110>{111}
$<11\bar{2}0>\{0001\}$	<210>{112}	<110>{111}

What emerges from the presented literature is that none of the developed theories can entirely elucidate all the experimental observations and results. The identification of the nuclei is critical, but to experimentally identify them is an open challenge.

1.2.1.2 Grain refinement of Al-Si alloys

Foundry alloys have been more difficult to grain refine than wrought alloys. The Al-5Ti-B master alloy is reported to be a poor grain refiner in comparison with Al-4B and Al-3Ti-3B master alloys.

Since the primary α-Al in hypoeutectic Al-Si systems has the same crystal structure as pure Al, Mohanty and Gruzleski [10] tried to apply their refining theory to Al-7Si foundry alloys. The authors conclude that alloys with excess B show a good refining effect because of the formation of a B-rich layer at the TiB2/melt interface. This interfacial layer nucleates primary α-Al via the eutectic reaction $L \rightarrow \alpha + AlB_2$ that occurs in the Al-B system. The Ti-based master alloys do not show significant refining behaviour, and the reason has been thought to be the presence of high levels of Si. The presence of Si has multiple effects, on the one hand, it determines the precipitation of the ternary aluminide $(Al_{1-x},Si_x)_3Ti$, or it leads to the precipitation of titanium silicide $TiSi_2$ on Al_3Ti poisoning its nucleation potential. On the other hand, Si moves the peritectic reaction (1. 1) to low temperatures, and thus hinders the nucleation of primary α-Al. Nevertheless, Mohanty and Gruzleski could not explain why the addition of TiB_2 is more effective than the addition of TiB_2 with excess Ti.

In foundry alloys, nucleant particles are the most efficient grain refiners, but the presence of segregating elements affects the amount of grain refinement. The effect of solute elements on grain refinement is the main focus of the solute paradigm. It has been developed later than the nucleant paradigm, in the 1990s, and concerns the role of segregating elements in restricting the growth of solidifying grains that leads to significant grain refinement.

The solute paradigm was postulated by Johnsson in 1993 [11] since the nucleation paradigm did not lead to comprehensive and consistent theories. The idea is that the presence of both nucleant particles and segregating elements have an essential role in grain refinement. The theories about nucleants never take into account the effect of growth restricting elements. The principal parameter in the solute paradigm is the Growth Restriction Factor (GRF) that enables to quantify the segregating behaviour of elements during solidification. It quantifies the restricting effect that solute elements have on the growth of the solid-liquid interface in new grains. Equation (1. 2) defines it as follows:

$$GRF = m(k-1)c_0 \tag{1. 2}$$

where m $[K/wt.\%]$ is the liquidus slope, k is the equilibrium partition coefficient and c_0 $[wt.\%]$ is the concentration of the solute in the alloy. The GRF value corresponds to the initial rate of development of the undercooled zone. The higher the value of the GRF, the smaller the resulting grain size. Table 1. 2 presents typical values of the parameters related to the GRF for some common alloying elements and some transition elements of interest for grain refining [1], [12].

Table 1. 2 – The segregating power of some elements in binary Al systems [1], [12]

Element	k	m [K/wt.%]	c_{max} [wt.%]	GRF [K]
B	0.067	1.015	0.022	$3.2 \cdot c_0$
Cu	0.17	-3.4	33.2	$2.8 \cdot c_0$
Hf	2.4	8.0	0.5	$11.2 \cdot c_0$
Mg	0.51	-6.2	3.4	$3.0 \cdot c_0$
Nb	1.5	13.3	0.15	$6.6 \cdot c_0$
Ni	0.007	-3.3	6	$3.3 \cdot c_0$
Sc	0.82	9.09	0.55	$1.6 \cdot c_0$
Si	0.11	-6.6	12.6	$5.9 \cdot c_0$
Ti	7.8	33.3	0.15	$220.0 \cdot c_0$
Zr	2.5	4.5	0.11	$6.8 \cdot c_0$

When more solutes are present in the melt, no interaction is assumed, and the total GRF comes from Equation (1. 3):

$$GRF_{tot} = \sum_i m_i(k_i-1)c_{0,i} \tag{1. 3}$$

Segregating elements restrict the growth rate and provide more time for nucleation events, but most importantly, they play a critical role in the undercooling-driven mechanism proposed by Tøndel [1]. These elements create a constitutionally undercooled zone in front of the solid/liquid interface, as represented in Figure 1. 3.

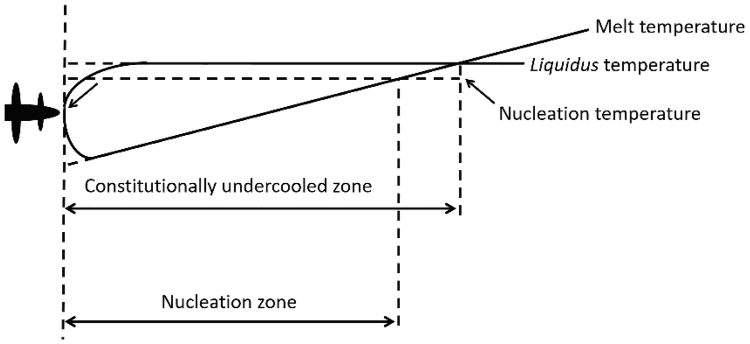

Figure 1. 3 – The constitutionally undercooled region in front of a growing dendrite [1]

This undercooled zone is fundamental to activate the nucleation sites present herein and interrupt the growth of previous nucleated grains. The size of this zone depends on the potency of the nucleant particles and the GRF of the elements present in the melt because the GRF value determines how far the interface can travel before a new grain is nucleated. Hence, the presence of both segregating elements and nucleating particles is the basis of effective grain refining. This mechanism explains why TiB_2 does not lead to grain refinement in pure Al, where segregating elements are not present. As can be deduced from Table 1. 2, the presence of alloying elements already has a small effect on grain size. Ti is the element with the highest GRF, but its role in grain refining is yet to be clarified.

A model developed by Hellawell and Maxwell [13] predicts the influence of various factors on the final grain size, and it results that among nucleant potency, cooling rate, nucleant particle size and growth restriction factor, the latter has the most significant effect. Experimental results reported in the literature support the goodness of this model; nevertheless, it presents some weak points. It assumes that Al_3Ti particles are the nucleants present in the melt, and they behave following classical theories without further explanations. Late works suggest that Ti as a solute element can be responsible for grain refinement, leading to a constitutionally undercooled zone in front of the growing interface. Nucleation occurs on the nucleating particles present in this undercooled liquid region [14].

Table 1. 3 summarises the principal grain refinement theories of both paradigms, nucleation and solute, and their main characteristics in terms of nucleating substrate and Ti solute effect. The theories of the nucleant paradigm were first developed for pure Al, but they are suitable also for Al-Si hypoeutectic alloys because the α-Al primary phase follows the same solidification mechanisms of pure Al. In foundry alloys, they combine with the solute paradigm because of the presence of alloying elements.

Table 1. 3 – Summary of the grain refinement theories

Paradigm	Theory	Nucleating substrate	Effect of Ti
Nucleant	Boride/carbide	borides or carbides	None
	Phase diagram	*via* peritectic reaction	Ti forms Al_3Ti, involved in the peritectic reaction
	Peritectic hulk	Ti-rich boride shell, *via* peritectic reaction	Ti is in the boride shell after Al_3Ti dissolution

	Hypernucleation	borides	Ti segregates on the boride providing a suitable interface for Al nucleation
	Duplex nucleation	Al_3Ti, formed on the surface of TiB_2	Ti segregates on TiB_2 and forms Al_3Ti
Solute	Solute	borides or other particles	Determines a constitutionally undercooled zone in front of the dendrite, and facilitates nucleation on the new grain

Recent studies investigated the refining behaviour of various transition elements in pure Al and Al-Si alloys, intending to provide helpful insight into some unclear factors that govern grain refinement. In pure Al, studies are available on rare-earths (RE) by Zhao *et al.* [15], Zr by Wang *et al.* [16] and Hf by Li *et al.* [17]. Patakham *et al.* [18] investigated the refining effect of Sc in al AlSi7Mg alloy, while Bolzoni *et al.* [19] focused on the addition of Nb to an AlSi10 alloy. Zhao *et al.* [15] studied the refining effect of an Al-Ti-C-RE master alloy, rich in Ce, and reported the presence of the $Ti_2Al_{20}Ce$ compound. The addition of various amounts of master alloy to pure Al led to evident grain refinement. The authors hypothesise that TiC acts as nucleant, Ti atoms protect it from dissolution and promote the precipitation of Al_3Ti that decomposes through the peritectic reaction of Equation (1. 1). The role of Ce-bearing compound is to decompose at 630 °C and release the Ti atoms that protect Al_3Ti from dissolution. The proposed mechanisms were not further investigated and have to be confirmed, mainly because they appear in contradiction with the literature about the role of TiC. The refining effect of Zr is mainly due to the precipitation of Al_3Zr, according to Wang *et al.* [16]. The main reason lies in the low crystal mismatch between Al_3Zr and primary α-Al, whereas the peritectic reaction $L + Al_3Zr \rightarrow \alpha$ may not be a crucial condition for grain refining. The authors suggest that the solute effect might not be crucial as well, but the perfect combination of matching crystallographic parameters and size distribution of particles is what governs grain refining. On the other hand, Li *et al.* [17] ascribe the refining effect of Hf to two main contributions: the solute effect and the precipitation of Al_3Hf. Similarly to what holds for Al_3Zr and Al_3Ti, Al_3Hf presents a low crystal mismatch with primary α-Al and can be involved in the peritectic reaction $L + Al_3Hf \rightarrow \alpha$. The authors observed that increasing amounts of Hf there is a slight change in the mechanisms involved for grain refining. At Hf contents lower than 0.2 wt.%, the constitutional undercooling is responsibe for grain refining. At medium Hf contents, between 0.2 and 0.5 wt.%, the presence of Al_3Hf determines heterogeneous nucleation and grain boundary pinning, in addition to the solute effect. Hf higher than 0.5 wt.% is less effective as grain refiner because of the coarsening of Al_3Hf particles, that do not act as nucleants. Patakham *et al.* [18] obtained similar results with the addition of Sc to an Al-Si-Mg alloy. Al_3Sc present a low crystal mismatch and thus act as heterogeneous nucleant for primary α-Al, assisted by a liquid consistutional undercooling. Nevertheless, the Sc refining efficacy is limited by the presence of alloying elements as it combines with Al, Si, Fe and Mg in a variety of intermetallic phases. Bolzoni *et al.* [19] assess the refining effect of an Al-2Nb-2B master alloy in an AlSi10 alloy. The authors affirm that both NbB_2 and Al_3Nb, present in the master alloy, act as nucleation sites for primary α-Al. This conclusion comes from the decrease of recalescence observed with increasing additions of master alloys. Nevertheless, the study does not provide data about crystal mismatch, phase diagrams or investigations within grains.

A common feature of the presented literature, is that the transition elements considered belong to the third, fourth and fifth group of the periodic table. All of them can form aluminides Al_3M with various lattice structure and limited mismatch with the Al lattice. These are the common characteristics that make the transition elements potential grain refiners for Al and its alloys. The lattice parameters and corresponding mismatch in Table 1. 4 are values for the pure binary Al_3M aluminides measured at room temperature [12].

Table 1. 4 – Lattice parameters and related invariant reactions and mismatch with Al lattice for Al_3M intermetallic compounds [12]

Group	Phase	Structure	Lattice parameters [Å]	Absolute mismatch δ with Al	Reaction type	Reaction T [°C]
3	Al_3Sc	Cubic $L1_2$	a = 4.103	1.32 %	Eutectic	660
4	Al_3Ti	Tetragonal $D0_{22}$	a = 3.848 c = 8.596	5.36 %	Peritectic	665.4
	Al_3Zr	Tetragonal $D0_{23}$	a = 4.014 c = 17.321	2.89 %	Peritectic	660.8
	Al_3Hf	Tetragonal $D0_{22}$	a = 3.893 c = 8.925	5.98 %	Peritectic	662.2
5	Al_3Nb	Tetragonal $D0_{22}$	a = 3.844 c = 8.605	5.47 %	Peritectic	661.4

The absolute lattice mismatch is $\delta = 100 \cdot |1 - a/a_0|$ where $a_0 = 4.0496\,\text{Å}$ is the lattice parameter of Al. Another feature that these Al_3M compounds have in common is their involvement in either a peritectic or eutectic reaction that leads to the solidification of primary α-Al.

In general, the presence of both potent nucleant particles and sufficient solutes is a necessary condition to obtain grain refinement. The occurrence of an invariant reaction could seem an additional significant event to refine the grain size. Nevertheless, some important factors are still missing in the current understanding of grain refinement mechanisms.

Despite the extensive research on new master alloys to efficiently refine Al-Si alloys, nowadays in foundry practise the classical Al-Ti-B alloys remain the most widespread, both for economic reasons and for the customs of the field.

1.2.2 Chemical modification of eutectic Si

Chemical modification is responsible for the formation of fibrous eutectic Si structures (Figure 1. 4a) in place of coarse flake particles (Figure 1. 4b), and it improves the mechanical properties of the casting.

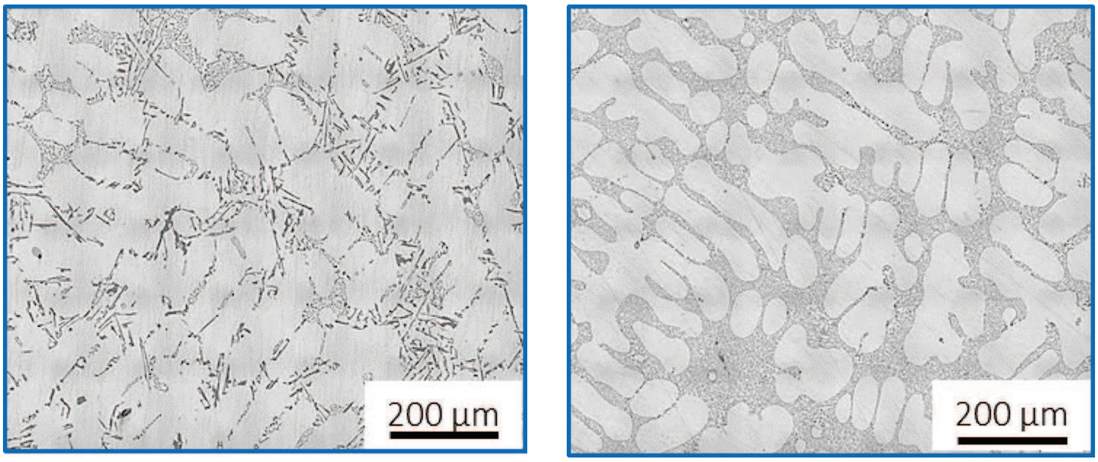

a) b)

Figure 1. 4 – Eutectic microstructure of AlSi7 alloys: a) unmodified; b) Sr modified (100 ppm)

It relies on the addition of trace impurity elements [20] via master alloys, although eutectic modification can also result from increased solidification velocity. The latter case is called quench modification [21]. It does not determine an actual flake-fibre transition, but it relies on the general phenomenon that fast cooling rates determine refined microstructures and non-faceted morphology. Na and Sr have been the primary modifiers in the foundry practice of the last decades. The latter is more easy-to-handle and presents more stability in the melt than Na. For this reason, nowadays Al-Sr master alloys are the most common chemical modifiers of Al-Si alloys. Current research highlights other modifying elements and aims to describe the mechanisms behind the eutectic modification.

1.2.2.1 Effect on the growth of eutectic Si

A brief description of the Al-Si eutectic solidification is necessary to correctly understand the mechanisms that govern the flake-fibre transition of eutectic Si due to the presence of modifier agents. The Al-Si eutectic is a coupled irregular eutectic system. It consists of a non-faceted phase, Al, and a faceted phase, Si. The faceted phase does not easily change growth direction due to its atomic structure, and the resulting eutectic structure presents a non-uniform lamellar spacing. Si presents a diamond cubic structure, and the anisotropic crystal growth is in the [211] direction to form planes (111), as illustrated in Figure 1. 5 [20]. The high tendency to grow in the [211] direction and the low tendency to grow in the [111] direction lead to a plate-shaped outline, hence the faceted definition. On a macro scale, Si grows as flat plates or coarse flakes (Figure 1. 4a).

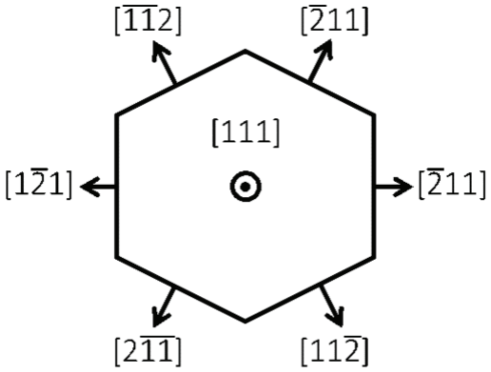

Figure 1. 5 – Growth of Si crystal in [211] direction

In 1960, Hamilton *et al.* proposed the growth model for Si known as the twin-plane re-entrant edge (TPRE) mechanism [22]. Figure 1. 6 illustrates the orientation relationship of a twinned Si flake and the growth direction according to the TPRE theory. It affirms that atoms can join re-entrant corners (141°) easier than ridges (219°), and thus their presence leads to rapid growth along the [211] direction. Hamilton *et al.* concluded that at least two twins are necessary for the growth of Si because the corner between them acts as a nucleation site for the subsequent atomic plane. If only one twin is present, a triangular tip forms, bounded by ridges, and the crystal has no other possibilities to grow. The presence of two twins guarantees the formation of a re-entrant corner, and thus crystal growth can continue.

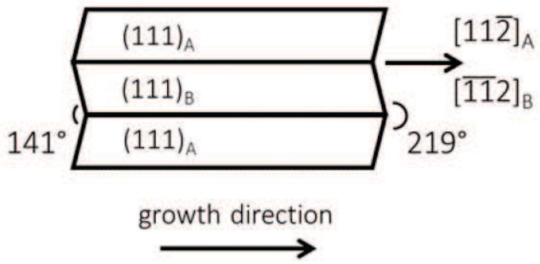

Figure 1. 6 – TPRE (twin-plane re-entrant edge) growth mechanism of a twinned Si flake

There is not a specific orientation relationship between eutectic Al and Si because the latter can change growth direction by twinning, but Al is not able to change growth direction fast enough to follow Si.

A more recent study updates the TPRE theory with the possibility of growth from triangular tips, previously discarded by Hamilton *et al.*, after in situ observation of the growth behaviour of Si crystals [23]. The rigid requirement of [211] growth hinders branching, a crucial mechanism in eutectic growth to maintain constant inter-flake distance and thus maximum inter-diffusion efficiency. Small-angle branching ($\theta < 10°$) is due to displacement twinning. It is a mechanism that involves the development of a new layer of twins with the same stacking sequence and the same [112] growth direction of the original layer (Figure 1. 7a). The frequency of several displacement twinning events determines the θ angle of branching. Small-angle branching occurs more frequently than the large-angle branching, that stems from the flank of the original flake and can present angles of 70.5° (Figure 1. 7b) or 109.5° (Figure 1. 7c). In these cases, the branch layer presents a different stacking sequence from the base layer, and the [112] growth directions of the new sequences are not parallel anymore to the original one. Large-angle branching is rare in the unmodified eutectic, that maintains its overall <112> growth habit, but becomes significant when modifying elements are present. This phenomenon is responsible for the transition from flake to fibrous eutectic, identified as the eutectic modification [20].

Two principal models for impurity modification, the impurity induced twinning (IIT) theory and the restricted growth theory, are the basis of research works performed in the past decades. The restricted growth theory states that modifier atoms are adsorbed at re-entrant edges and thus deactivate the TPRE growth mechanism. The anisotropic growth in [112] direction results hindered, and an isotropic fibrous growth occurs. Several successive branching events, based on the large-angle mechanisms depicted in Figure 1. 7b and Figure 1. 7c, permit a resultant growth axis in directions that lie between <100> and <110>. This restricted growth theory is also reported as the restricted TPRE (RTPRE) or the poisoned TPRE model.

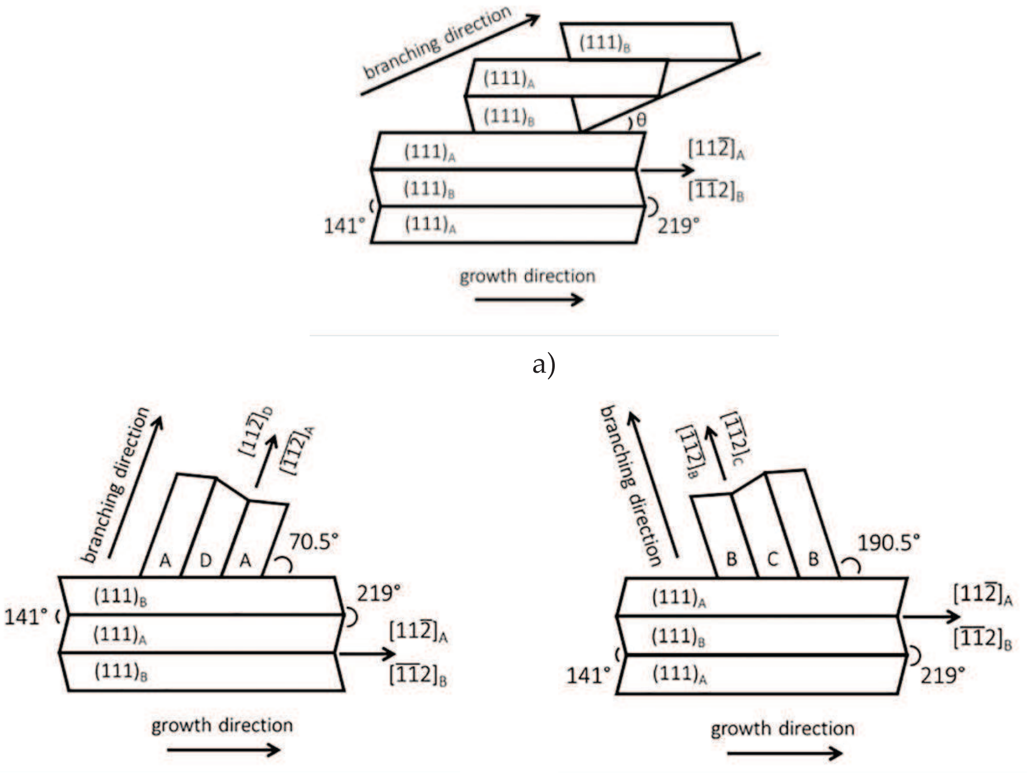

a)

b)

c)

Figure 1. 7 – Crystallographic mechanism of branching: a) small-angle by displacement twinning; b) 70.5° large-angle; c) 109.5° large-angle

Lu and Hellawell [24] introduced the impurity induced twinning (IIT) theory, based on the adsorption of chemical modifiers onto surface steps, thus poisoning the growth of Si atomic layers. The adsorbed impurity atoms change the stacking sequence facilitating the formation of new twins, and thus promote growth in several [112] directions. The authors suggested the ratio of atomic radii r_i/r_{Si} between the *i*-element and Si as a criterium for IIT. In fact, an impurity atom of appropriate size is necessary to generate the twin, and the optimum atomic radii ratio is 1.65, according to Lu and Hellawell [24]. Theoretically, the best modification should occur by the addition of elements greater than or equal to the proposed ratio, and its value is reasonably close to the atomic radii ratio of the most commonly employed modifying agents, such as Na, Sr and Ca. Figure 1. 8 illustrates the distribution of atomic radii ratios around the optimum value, represented by the dashed line. The microstructure of hypoeutectic Al-Si alloys containing Sr, Na, Ca, Ba and Eu present modified eutectic Si with a fibrous morphology [25]–[27]. For this reason, researchers consider valid the IIT theory, even though Yb and other lanthanides do not lead to modification according to some experimental results [27].

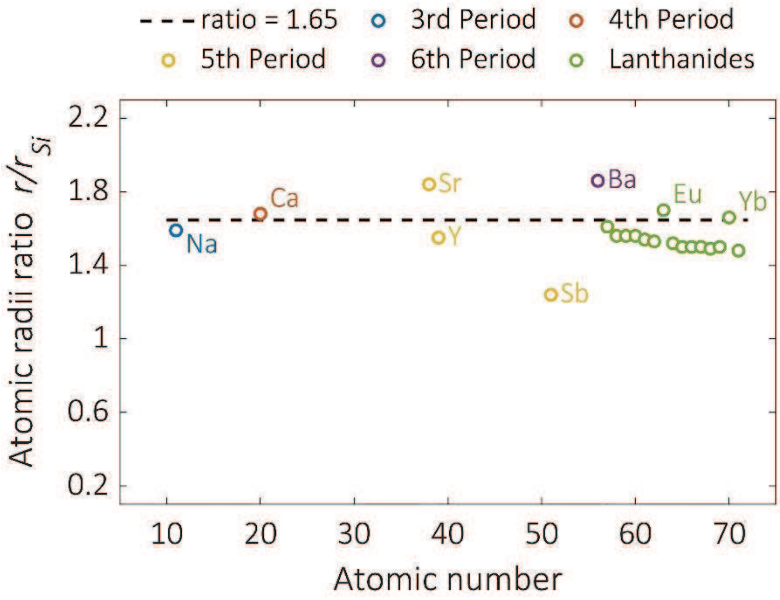

Figure 1. 8 – Atomic radii ratio v. atomic number

Both IIT and RTPRE theories are widely accepted, and their common element is that the impurity elements added to promote eutectic modification lead to a vast increase in the frequency of twinning in eutectic Si. Further investigations with innovative techniques help the development of these significant theories in order to elucidate some controversial experimental results.

Several works in the literature confirm the presented theories investigating the behaviour of common modifying elements, Na and Sr. Nogita *et al.* [28] investigated the Sr distribution within the eutectic Si phase in a Sr-modified AlSi10Cu alloy through micro x-ray fluorescence microscopy (μ-XRF). The resulting elemental maps highlighted that Sr has a negligible content inside eutectic Al. Instead, it segregates just in eutectic Si with a quite homogeneous distribution inside the Si particle [28]. This result seems in line with the proposed theory. On the other hand, Timpel *et al.* [29] pointed out that Sr atoms do not homogeneously distribute inside the Si particles. Enrichment of both Sr and Al atoms are visible inside Si particles via atom probe tomography (ATP) and transmission electron microscopy (TEM) analyses, meaning that a co-segregation phenomenon occurs. The authors indicate such ternary co-segregations with a rod-like morphology in three dimensions as type I co-segregations. Type II co-segregation is another ternary co-segregation identified by TEM at the eutectic interface between Al and Si. They are rod-like and extend from the Al/Si interface into the Si particle. The stoichiometries of type I and type II segregations differ slightly but, as illustrated in Figure 1. 9, they present a significant difference in their role in the modification of eutectic Si. The type I co-segregations promote the formation of twins as described by the IIT model. The type II co-segregations are adsorbed at the re-entrant edges of the solid-liquid interface of Si and thus prevent the growth of a new atomic layer, in line with the RTPRE theory.

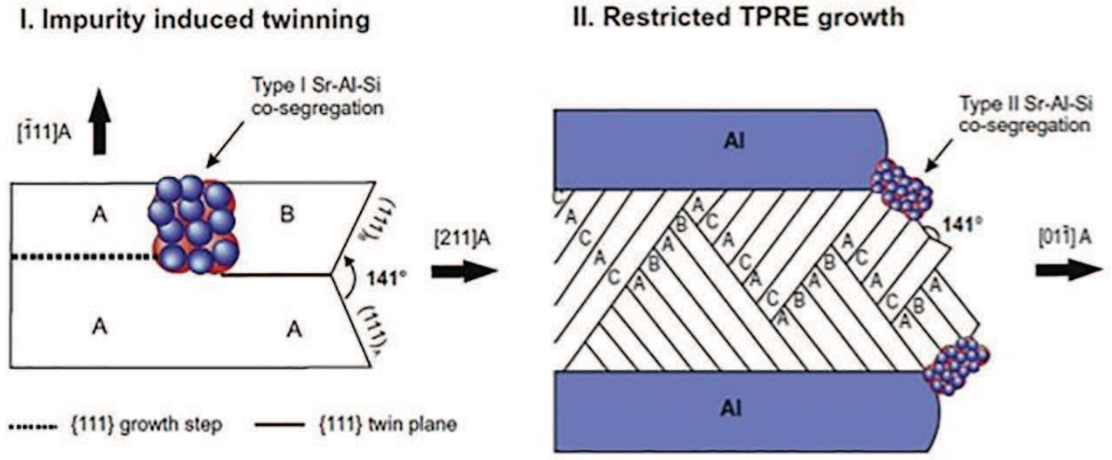

a) b)

Figure 1. 9 – Role of Al-Si-Sr co-segregation in eutectic Si modification: a) type I promotes twinning according to the IIT model; b) type II restricts growth according to the RTPRE model [29]

In general, the authors conclude that ternary X-Al-Si co-segregations, X being the modifier impurity element, in seem to play a critical role in eutectic Si modification. Type I co-segregations mainly contribute to the formation of twins in eutectic Si during growth while type II co-segregations contribute to the branching of Si fibres [29].

Li *et al.* [30] elucidated the mechanism of Si modification with Sr, Na and Yb additions to an AlSi5 alloy at different cooling rates. With very high cooling rates (produced via melt-spinning), Si particles in unmodified alloys show a limited number of parallel twins but show a refined morphology. After the addition of Sr or Na, a significantly increased number of multiple twins occurs, and they possibly cause the entrapment of some solute particles during their growth. EDS analyses at the intersections of multiple twins revealed the presence of Sr- or Na-rich clusters, confirming that they are active elements during twin formation via IIT and RTPRE mechanisms. On the contrary, the presence of Yb does not influence Si twinning despite the favourable atomic radii ratio for the IIT mechanism. The same modified alloy produced with moderate cooling rates (via conventional casting) presented Sr segregation at the intersections of Si twins, that promote the formation of multiple twins. The segregation of Yb atoms, on the contrary, is distinctly different from the adsorption of Sr and Na. Yb does not play an active role in IIT or RTPRE growth mechanisms since it is not present within eutectic Si. The authors suggest that the Yb-rich segregation lines are artefacts caused by the solute entrapment during eutectic Si natural TPRE growth, and do not contribute to multiple twinning. Li and Schumacher [31] also investigated the addition of Y in the same system. In the case of moderate cooling rates, the presence of Y does not lead to eutectic modification, and Si flakes do not present a significant number of twins. Y atoms do not segregate in Si particles but precipitate as either AlY or Al_2SiY phases. In the Y-added alloy produced via melt-spun multiple twins are present in refined Si particles. Y-based compounds did not precipitate, and the authors suggest that Y solubility increases with high cooling rates. Thus Y atoms may remain in Al and Si particles and result in Si twinning. The authors conclude that Y behaves as a refiner and not as a modifier for eutectic Si particles.

From the results concerning Na and Sr, several works aimed to deepen the modifying effect of elements other than Sr and Na. Nogita *et al.* [27] investigated the effect of rare-earths on Si modification and reported that all elements cause a depression of the eutectic temperature. The rate at which the temperature falls with increasing element content depends on the specific element considered. None of the lanthanides promotes Si modification, but just a refining of Si particles which nevertheless still exhibit a flake-like morphology. The only exception is Eu, which leads to a complete fibrous Si morphology. Since all the lanthanides present an atomic radii ratio reasonably close to the ideal one of 1.65 (Figure 1. 8), the fact that only Eu acts as a modifier indicates that the ratio value does not predict the flake-fibre transition in the eutectic Si. The study of the eutectic solidification through quench test revealed a high nucleation frequency in the unmodified alloy. The addition of rare-earths reduces the number of nucleation events leading to coarser eutectic grains. This phenomenon occurs both for modifying and for refining elements, and it means that nucleation of eutectic grains and eutectic Si modification follow independent mechanisms. The topic of eutectic nucleation is discussed later in the present paragraph (§1.2.2.2).

Later studies with the μ-XRF technique highlighted the reason behind the different behaviour of Eu from the other rare-earths [32]. Yb is considered for comparison because it has the theoretical optimum atomic radii ratio (1.65) according to the IIT theory. Both Yb and Eu determine a depression of the eutectic temperatures. The results of μ-XRF show that Eu presents a negligible concentration in eutectic Al while strongly segregates in eutectic Si. This behaviour is somewhat similar to the one previously observed for Sr [28], [29]. Yb does not segregate either inside eutectic Al or inside eutectic Si but precipitates in intermetallic compounds within the eutectic phase. The results of these studies suggest that Eu has a modifying behaviour and presents two contributes to modification. The first one is the segregation inside Si particles with mechanisms in line with either IIT or RTPRE theories. The second contribution to modification is the depression of the eutectic temperatures, that determines a refinement of Si particles and a reduction of the growth velocity for the flake-to-fibre transition. Yb and other rare earth elements only contribute to Si refining through a depression of eutectic temperatures. Once again, experimental findings suggest that the atomic radii ratio is not a sufficient condition to individuate modifying elements.

Li *et al.* [33] further characterised by TEM Eu and Yb modified alloys produced by melt-spinning to deepen their different modification behaviour. Results show that the addition of Eu promotes the formation of several multiple twins inside Si particles, similar to what previously observed for Na and Sr [30]. EDS analysis highlighted the presence of Eu at the intersection of multiple twins, confirming its active role as a modifying agent according to the IIT theory. On the other hand, Yb adsorption at the intersections of twins did not occur, but some Yb-rich segregations appeared along the <112> Si direction, similar to what observed in Sr-modified alloy [29]. Such segregations should poison the TPRE mechanism and lead to the formation of parallel twins, but the total amount of Yb-rich segregation lines is not enough to promote several parallel twins. These results further confirm that Yb does not act as a modifying element, but its refining effect on Si particles is solely due to the increased undercooling. Therefore, the bonding behaviour with Si, in addition to the atom size, is a crucial feature to obtain the eutectic modification.

Recently, Barrirero *et al.* [34] compared once again the modification behaviour of Eu and Yb through APT analysis. Results are in line with previous work, as Eu leads to a fibrous Si morphology while Yb just refined Si particles compared to the unmodified alloy. Besides, both alloys exhibit small intermetallic compounds with composition Al_2Si_2X (X = Eu, Yb) located in the eutectic region. The presence of such compounds with composition and crystal structure similar to Al_2Si_2Sr, found in Sr-added alloys, justifies the depression of the eutectic temperatures, later explained in the paragraph. Si particles in Eu-added alloy exhibit a large density of twin defects, similarly to Sr and Na-added alloys, while Si particles in Yb-added alloy exhibit just a small number of straight twins, similarly to the unmodified condition. The APT analysis revealed the inhomogeneous distribution of Al and Eu inside Si particles and the presence of co-segregation areas of Al, Si and Eu in Eu-added alloys. Yb atoms inside Si particles were not detected in the Yb-added alloy, but just inhomogeneous segregations of sole Al are present. The conclusion is that both Eu and Yb-added alloys have a ternary eutectic point with the formation of Al_2Si_2Eu or Al_2Si_2Yb compounds before the eutectic solidification, which contributes to the refining of Si through increasing required undercooling. The main difference is that early-stage Al_2Si_2Eu clusters precipitate on the facet of Si crystals, and they increase growth direction diversity according to the RTPRE model. Although Al_2Si_2Yb ternary compounds precipitate, the same early-stage ternary clusters cannot form on the facet of Si crystal because of the high misfit with the Si surface. In the light of these results, the actual condition that ascribes an element as a modifier is its possibility to form ternary clusters on the facet of Si crystals. Moreover, the misfit between these ternary clusters and Si surface is a critical factor, as reported in Table 1. 5.

Table 1. 5 – Misfits of ternary compounds Al-Si-X related to Si [34]

Element X	Misfit with Si [%]	Si structure
Na,Sr,Eu	$-3 < \delta < -6$	Coral
Ca,Ba	$-6 < \delta < -10.5$	Mixed
Yb,Y	$\delta > -10.5$	Refined flakes

Elements like Na, Sr and Eu, form clusters with the smaller misfit among all the modifying elements, explaining their excellent efficiency as modifiers. Ternary compounds with Ca and Ba have a slightly higher misfit, and therefore their addition leads to mixed fibrous/coral-like microstructure. Lastly, elements like Yb and Y determine ternary clusters with the highest misfit that prevents their formation on Si surface. For this reason, they present the lowest potency as modifiers and their presence leads just to a refinement of Si particles.

Moniri *et al.* [35] recently reported that the presence of modifiers influences both nucleation and growth kinetics. The first corresponds to a higher undercooling compared to the unmodified alloy, while the latter mirrors in the marked difference in the morphological properties. The impurity species alter the stacking sequence of the faceted phase (i.e. Si), and consequently, the non-faceted phase (i.e. Al) replaces the faceted one during growth and completely encases it.

In conclusion, years of investigations by different techniques lead to the understanding that the trace modifier restricts the growth of eutectic Si, by itself or via the precipitation of ternary clusters. The hindered propagation of the faceted phase increases isotropic growth and determines the flake-fibre transition. Nevertheless, a unified theory of eutectic modification remains still elusive.

1.2.2.2 Side effects on the nucleation of Al-Si eutectic

Recent research on eutectic modification in Al-Si alloys identified changes in the eutectic nucleation due to the presence of modifiers. In unmodified alloys, a large number of eutectic grain nucleate, while the presence of Sr and Na dramatically reduces the number of eutectic grains [36]. McDonald *et al.* [37] define the eutectic grain as «a connected region of Al-Si eutectic that has grown from a common source», without implications about crystallography. Either phase may be poly- or mono-crystalline depending on the growth mechanisms that operate. Eutectic grains present three primary nucleation mechanisms: from the mould wall and opposite to the thermal gradient (Figure 1. 10a), on the primary α-Al dendrites (Figure 1. 10b), and interdendritic heterogeneous nucleation (Figure 1. 10c).

When eutectic nucleation occurs from the primary α-Al dendrites, eutectic Al presents the same crystallographic orientation of primary α-Al [36]. This mechanism of eutectic nucleation is typical of unmodified alloys. McDonald *et al.* [38] proved via quench tests that the eutectic nucleation starts from polygonal Si particles on dendrite tips. In turn, polygonal Si particles nucleate on AlP particles, ejected at the solid/liquid interface during the growth of primary α-Al dendrites. AlP particles come from the presence in the melt of P, a widespread impurity element. These particles are potent nuclei for eutectic Si, and thus the required undercooling is very limited.

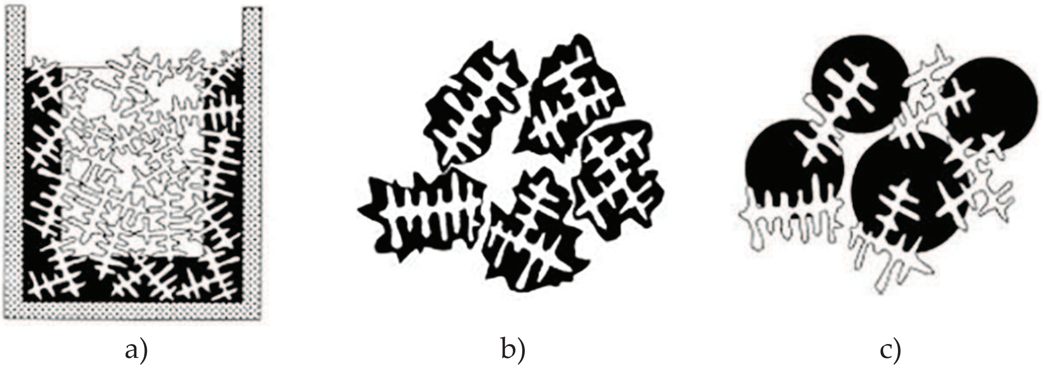

Figure 1. 10 – Nucleation mechanisms of eutectic grains: a) from the wall; b) on the primary α-Al dendrites; c) interdendritic nucleation [37]

The addition of modifying elements promotes heterogeneous nucleation either interdendritic or at the mould wall. The reason is the precipitation of ternary Al-Si-X compounds (X being the modifying element) before the eutectic solidification. These compounds nucleate on AlP particles and thus consume active nuclei for the eutectic nucleation, that has to occur on less potent nuclei in the interdendritic liquid [39]. In this case, eutectic Al presents different crystallographic orientations compared to the primary α-Al, as it grows independent from the dendrites [36].

Table 1. 6 lists some potent nuclei of eutectic Si and the related undercooling required for activation. Less potent nuclei require a high undercooling for eutectic nucleation to occur, leading to a reduced nucleation frequency and large eutectic grains [40].

Table 1. 6 – Nucleating particles for eutectic Si and related undercooling required [40]

Nucleants	Alloy condition	Undercooling of eutectic nucleation [°C]
Al dendrite	Na-free and P-free	5 ÷ 6
	Na-modified	10 ÷ 12
AlP	P-containing	2 ÷ 3
AlNaSi	Na overmodified	3 ÷ 4
Unidentified particles	Without precedent nucleants	> 15

A limited number of nucleation events force the solid/liquid interface to move faster in order to maintain a given rate of heat extraction [38]. The increment of growth velocity determines the gradual refinement of Si flakes. The minimum growth velocity to obtain a flake-to-fibre transition is 500 μm/s, and it is complete at 807 μm/s [21]. Figure 1. 11 shows the gradual change of eutectic Si morphology with different solidification rates.

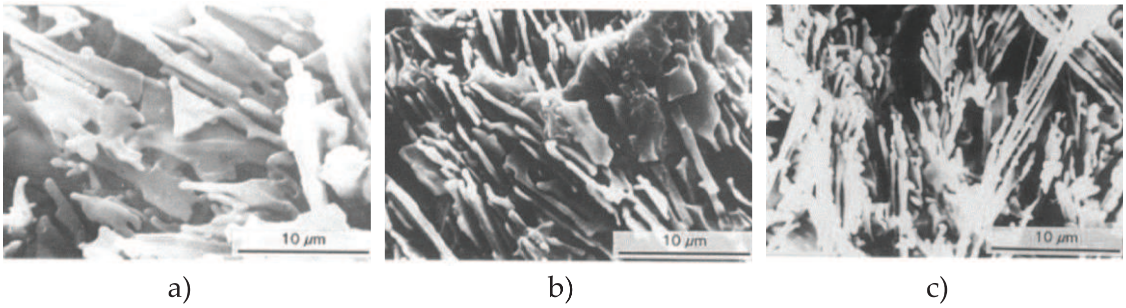

Figure 1. 11 – The change of Si morphology with growth velocity: a) completely flake, 308 μm/s; b) mixed flake and fibrous, 505 μm/s; c) completely fibrous, 807 μm/s [21]

These high growth velocities generally are due to significant temperature gradients and not to undercooling. The addition of modifying elements decreases the minimum growth velocity significantly down to 10 μm/s. In modified alloys, the growth velocity easily overcomes the new minimum threshold and this phenomenon results in an entirely fibrous Si morphology [41].

McDonald *et al.* [37] also consider the purity of AlSi10 alloys. The differences between commercial-purity (CP) and high-purity (HP) alloys rely on the production procedure and result in the Fe and Ti contents. In the unmodified CP alloy, a large number of eutectic grains nucleate and grow with an asymmetrical shape. Eutectic Si particles present a coarse flake morphology, as expected. On the other hand, a limited number of grains nucleate in the unmodified HP alloy and grow with a spherical shape. Si particles result with a refined flake-like morphology. The addition of Sr significantly reduces the number of eutectic grains in the CP alloy, while it does not alter the already limited eutectic nucleation in the HP alloy. This research highlights that when nucleation of eutectic grains is not favourable, a high eutectic growth rate results. The increased interface velocity is not sufficient to determine the flake-fibre transition, that needs the presence of Sr to occur.

In conclusion, the depression of eutectic temperatures during solidification indicates a change in nucleation and growth of the eutectic. It cannot be directly considered as a fundamental parameter of eutectic modification because it does not occur in high-purity Al-Si alloys [37]. Eutectic growth undercooling indicates refinement of Si particles, without high-angle branching events, in commercial purity Al-Si alloys.

1.2.2.3 Interaction between modifying and alloying elements

Ca is a common trace element that often occurs to be in the melt. Ca enters the melt with the addition of Si, because it is present in the form of intermetallic compounds like silicides, phosphides and nitrides. Even if it is possible to remove Ca from the melt, it is not possible to entirely avoid its presence in Al-Si alloys. The literature reports that Ca and Sr interact together and reduce the modifying effect of each other [42]–[46]. Samuel *et al.* [42] investigated the effect of Ca on Sr modification in AlSi7Cu3. The Sr content was of 150-200 ppm, and the additions of Ca varied from 50 ppm to 500 ppm. The authors concluded that for contents higher than 100 ppm, Ca has a de-modifying effect on the microstructure despite the presence of Sr. The reason is the formation of $Al_x(Ca,Sr)Si_x$ compounds, and Sr is no longer available as a modifier of eutectic Si. Rakhmonov *et al.* [43] studied different AlSi5Cu1 alloys with 30 ppm of Ca and different levels of Sr, from 65 ppm to 210 ppm. The authors observed an increased quantity of pre-eutectic $Al_2(Ca,Sr)Si_2$ particles with the increase of Sr content. These compounds deactivate the role of AlP as nucleation site for eutectic Si but retain Sr and Ca, no longer available for modification. El-Hadad and colleagues [44] affirm that 20 ppm of Ca in a Sr-modified AlSi7Cu3 alloy determine the precipitation of the $Al_7(Ca,Sr)Si_7$ compound. Its stoichiometry changes to $Al_2(Ca,Sr)Si_2$ when Mg is present in the alloy, and concurrently the morphology varies from lath to polygonal. Sreeja Kumari *et al.* [45], [46] report that Ca has a behaviour similar to the one of Sr because it promotes the nucleation of eutectic cells from the interdendritic liquid and not from primary α-Al dendrites. These studies agree on the fact that the compounds that contain Ca and Sr precipitate before the eutectic solidification and tend to nucleate on oxides and AlP particles. Thus they deactivate nucleation sites for the Al-Si eutectic.

Early studies evaluated the effects of Mg additions on the mechanical behaviour of both unmodified and Sr-modified alloys [47], [48]. Joenoes and Gruzleski [49] report that Mg additions up to 1 wt.%, besides their benefits on mechanical properties, slightly increase the modification level of Si particles. Furthermore, Feikus *et al.* [50], [51] affirm that in unmodified alloys Mg enables a change in eutectic Si morphology from coarse lamellar to acicular. Since the distinction between refining and modification is relatively recent, probably the author referred to a refinement phenomenon with the misleading noun "modification". Nevertheless, recent research does not investigate Mg as a modifying agent because it does not satisfy the atomic radii ratio required by the IIT mechanism ($r_{Mg}/r_{Si} = 1.36$).

Some authors later investigated the influence of Mg and Cu on the nucleation and the morphology of Al-Si eutectic and AlSi7 [52]–[54] and AlSi10 alloys [55], [56]. Heiberg and colleagues [53] report that the eutectic solidification front in the binary AlSi7 alloy is planar and regular, independently of the Sr level. In the commercial AlSi7Mg0.3 alloy, on the other hand, solidification occurs through a eutectic mushy zone because the eutectic reaction is no longer isothermal (Figure 1. 12).

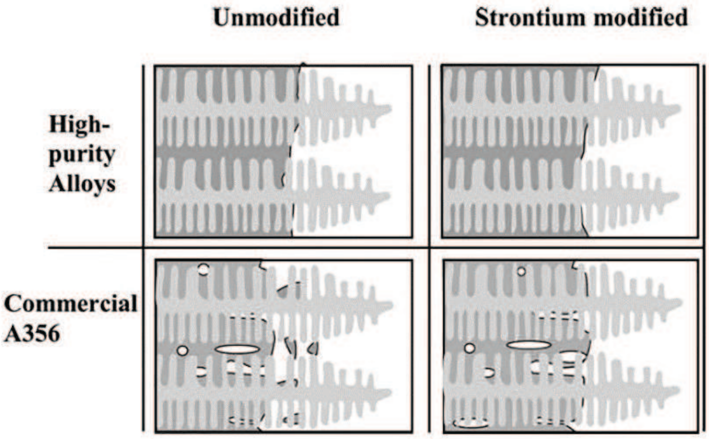

Figure 1. 12 – Schematic representation of the eutectic growth front (dark gray) in modified and Sr modified AlSi7Mg alloys. Primary dendrites are light grey and liquidi s white. The eutectic growth front is planar in the high-purity alloys while the commercial purity alloys present a eutectic mushy zone [53]

The eutectic Si appears well modified in the binary alloy with 150 ppm of Sr while it presents coarse particles in the AlSi7Mg alloy with 100 ppm of Sr. More recently Heiberg *et al.* [52], [54] face the addition of Cu (0.7 ÷ 3 wt.%) and Mg (1 wt.%) to Sr-modified AlSi7 alloys. Microstructural investigations highlight a coarsening of the eutectic microstructure as the Cu content increases, regardless of the Sr content, and the eutectic inter-flake spacing increases from 2 μm to 7 μm. Darlapudi and colleagues [55], [56] investigate the influence of Cu (1 ÷ 6 wt.%) and Mg (0.5 ÷ 2.5 wt.%) additions on the eutectic morphology of AlSi10 alloys. The studies focused on both eutectic nucleation and growth dynamics. For what concerns nucleation, the segregation of Cu in unmodified alloys has a limited effect on the already high nucleation density of eutectic cells. On the other hand, the presence of Cu leads to a constitutional supercooling ahead of the solidification front because Sr poisons the density and the potency of available nuclei. The nucleation-free zone around the growing grains results limited and eutectic nucleation is promoted. As a consequence, the number of eutectic grains increases as the Cu content increases [55]. The presence of Mg determines a similar effect, as it increases the nucleation density of eutectic grains [56].

In conclusion, the presented literature highlights that Mg and Cu both influence the density of eutectic grains through constitutional undercooling. It plays a fundamental role during the eutectic solidification and determines the resulting morphology of Si particles. On the other hand, Sr does not affect the morphology of the solid/liquid interface but influences only its velocity.

1.3 ALLOYING ELEMENTS

Alloying elements are fundamental to control the properties of an alloy. Mg and Cu are the most common elements added to Al-Si alloys since small additions can significantly improve their mechanical properties. After proper heat treatment, Mg and Cu are present in fine precipitates that increase the strength of the alloy at expenses of the ductility. Specific applications require the addition of particular alloying elements, such as Ni, to improves high-temperature mechanical properties.

1.3.1 Addition of Cu

It is of interest for the automotive industry to combine the ductility of AlSi7Mg alloys and the tensile properties of AlSi7Cu alloys. A reasonable compromise could be the addition of small amounts of Cu to the AlSi7Mg alloy. It is essential to reach the composition that optimises the mechanical properties and minimises the occurrence of hot tearing and shrinkage porosity related to the presence of Cu [57]–[59].

Cu additions to Al-Si-Mg casting alloys have been increasingly investigated over the last two decades, as it leads to increased tensile mechanical properties because of solid solution and precipitation strengthening. Cu changes the precipitation sequence and thus the strengthening phases in the Al-Si-Mg system. Besides to β-Mg_2Si, also Q-$Al_5Mg_8Cu_2Si_6$ and θ-Al_2Cu start to precipitate when Cu is present in such alloys. Some studies on as-cast Cu-added AlSi7Mg alloys concerned the influence of melt quality, porosity and Cu phases on tensile properties [60]–[63], and Table 1. 7 summarises the results.

Table 1. 7 – Summary of mechanical properties available in the literature

Authors	SDAS [µm]	Cu [wt.%]	UTS [MPa]	Δ_{UTS} [%]	e [%]	Δ_e [%]
Taghiabadi *et al.* [60]	-	0.0	189		9.2	
		0.5	200	+ 6	8.2	- 11
		1.5	248	+ 31	6.4	- 30
		3.0	211	+ 12	5.5	- 40
Shabestari and Moemeni [61]	-	0.2	170		6.5	
		0.7	175	+ 3	5.5	- 15
		1.5	180	+ 6	5.0	- 23
		2.5	175	+ 3	4.5	- 31
Seifeddine *et al.* [62]	10	0.0	220		14.0	
		0.6	270	+ 23	15.0	+ 7
		1.7	310	+ 41	16.0	+ 14
		2.5	315	+ 43	14.0	
	25	0.0	210		10.0	
		0.6	250	+ 19	15.0	+ 50
		1.7	285	+ 36	8.5	- 15
		2.5	280	+ 33	7.0	- 30
	50	0.0	160		7.0	
		0.6	180	+ 13	8.2	+ 17
		1.7	230	+ 44	5.0	- 29
		2.5	240	+ 50	4.0	- 43
Di Giovanni *et al.* [63]	30	0.0	200		10.5	
		0.5	225	+ 13	8.5	- 19
		1.0	260	+ 30	6.0	- 43
	35	0.0	200		12.0	
		0.5	190	- 5	6.0	- 50
		1.0	250	+ 25	8.5	- 29
	40	0.0	185		10.0	
		0.5	185		7.0	- 30
		1.0	240	+ 30	7.5	- 25

Nevertheless, results show some discrepancies because the increases in YS and UTS are not of similar magnitude for the same Cu contents. It is worth to note that these literature results are not directly comparable since microstructural features, such as SDAS and AGS, are not clearly stated in all works and alloy conditions, such as grain refining and Sr modification, are not similar. Taghiabadi *et al.* [60] report a maximum increase of 30 % for UTS with 1.5 wt.% of Cu. At the same time, elongation shows a continuous decrease with increasing Cu. Shabestari and Moemeni [61] observe a maximum increase of 23 % for YS and 6 % for UTS with a Cu content of 1.5 wt.%. Elongation continuously decreases with increasing Cu. Also, the author report that the effect of Cu on porosity formation decreases with increasing cooling rate. Both studies conclude that Cu content higher than 1.5 wt.% leads to a significant shrinkage porosity, that overcomes the beneficial effects of Cu-based compounds on the tensile properties. For this reason, the maximum increase in tensile properties is observed with 1.5 wt.% of Cu. Seifeddine *et al.* [62] study a wide range of Cu additions, from 0.6 to 5.4 wt.%, and three different SDAS values thanks to controlled cooling rates. Table 1. 7 lists results for Cu contents up to 2.5 wt.% for comparison with the other works. The authors obtain a continuous increase in UTS for all the Cu additions investigated. Besides, elongation shows a decreasing trend with increasing Cu. These observations are valid for the three SDAS value investigated. Since the specimen are directionally solidified and well-fed, mechanical properties result beneficially influenced by levels of Cu higher than 1.5 wt.%, in contrast with previously reported literature [60], [61]. Di Giovanni *et al.* [63] observe an increase in the range of 25 ÷ 30 % for UTS with 1 wt.% of Cu, for SDAS going from 30 to 40 μm. As observed in the works mentioned above, elongation decreases as Cu content in the alloy increases.

1.4 THERMAL ANALYSIS

The thermal analysis technique appears as a reliable prediction tool for the quality of Al alloys in the metal casting industry to record the solidification temperatures of an alloy and sometimes to predict some features of the microstructure. It is an old technique born in the 1950s, initially developed in the cast iron foundry. After a significant development for Fe alloys [64]–[67], later improvements moved its application to the Al foundry [68]–[70].

It requires to record the cooling curve of a solidifying alloy and to analyse the inflexion points of the curve. Every alloy has a specific behaviour during solidification, and its thermal fingerprint is the first information that stems out from the cooling curve. As an example, Figure 1. 13 represents the cooling curves of pure Al and a binary AlSi7 alloy compared to the Al-Si phase diagram. The phase diagram refers to equilibrium conditions, *i.e.* infinitely slow cooling rates. Nevertheless, at sufficiently low cooling rates the main phase transformations are detectable at the same temperatures in the real-conditions solidification recorded by thermal analysis. Hence these cooling rates determine a good approximation of equilibrium conditions. Furthermore, the presence of alloying and trace elements can significantly change the solidification sequence, and in these cases, the cooling curve becomes a valuable instrument.

The cooling rate of the casting determines itself the coarseness of the microstructure since high cooling rates give rise to very fine microstructures. Most reactions that occur during solidification are exothermic and result in the reduction of the cooling rate or, in some cases, can lead to an increase in temperature called recalescence. In order to reveal the exact temperature at which minor and significant phase changes occur, it is often necessary to plot the first derivative of temperature over time ($T' = dT/dt\ [K/s]$) as a function of time. Small changes in the slope of the cooling curve result in evident peaks on the first derivative curve. The second derivative ($T'' = d^2T/dt^2\ [K/s^2]$) is useful to detect the beginning of nucleation events. The baseline is a theoretical first derivative of the cooling curve, without phase transformations, that nevertheless takes into account the changes in thermal properties due to phase transformations. The difference between the baseline and the first derivative enables to calculate latent heat and solid fraction as solidification proceeds.

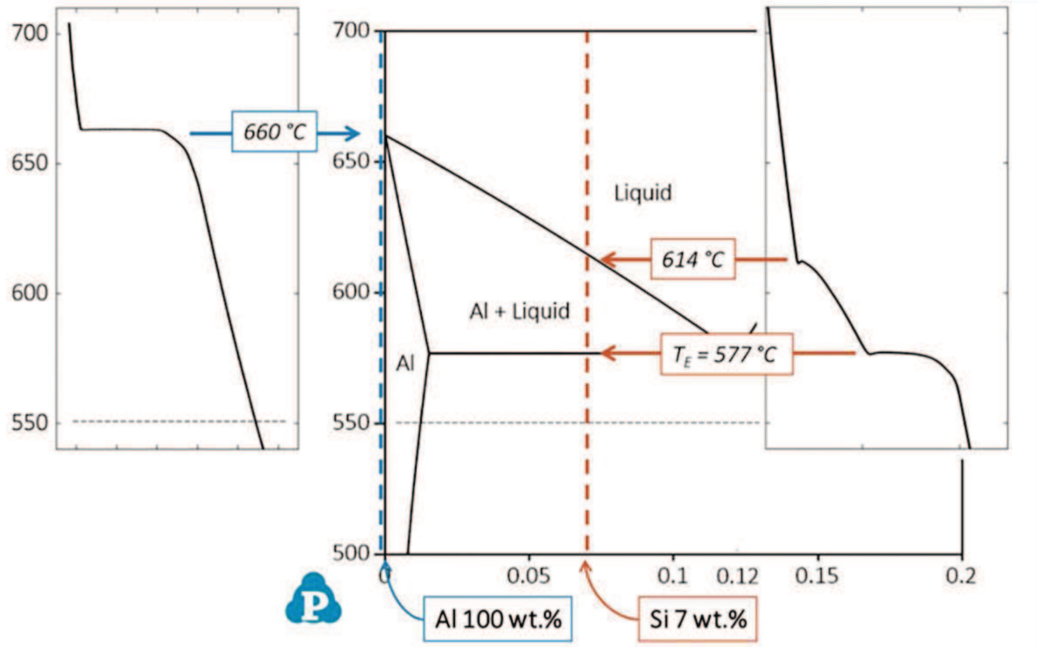

Figure 1. 13 – Al-Si phase diagram and cooling curves

The analysis of cooling curves can be of two kinds, and the experimental setup changes accordingly. The Newtonian method requires only one thermocouple, while the Fourier method necessitates two thermocouples in the melt [64]. The name of the two methods refers to the heat equation considered for the analysis, and consequently, the baseline equation differs in the two methods.

In the Newtonian analysis, the thermal gradient across the sample is considered to be zero, and the heat transfer between the casting and the mould occurs by convection. The heat equation for the system that consists of the solidifying metal and the mould follows Equation (1. 4):

$$\frac{dT}{dt} = -\frac{U \cdot A \cdot (T - T_0)}{m \cdot c_p} + \frac{1}{m \cdot c_p} \cdot \frac{dQ}{dt} \tag{1. 4}$$

where m $[kg]$ is the mass of the sample, c_p $[J/kg \cdot K]$ is the specific heat of the metal, T $[K]$ is the metal temperature, T_0 $[K]$ is the room temperature, t $[s]$ is time, U $[W/m^2 \cdot K]$ is the overall heat transfer coefficient, A $[m^2]$ is the sample surface area, and Q $[J]$ is the latent heat of solidification. The assumption of $dQ/dt = 0$ leads to Equation (1. 5) of the Newtonian baseline:

$$\frac{dT}{dt}_N = -\frac{U \cdot A \cdot (T - T_0)}{m \cdot c_p} \tag{1. 5}$$

Assuming that the heat transfer coefficient and other thermophysical parameters are constants, Equation (1. 5) can be integrated to obtain the cooling curve without transformation. The baseline can be expressed as an exponential function [67], [68], or simplified by fitting a logarithmic or polynomial curve to selected data of the first derivative [69]. The cumulative area between the first derivative and the baseline as a fraction of total area between them represents the solid fraction at time t during solidification [71].

The Fourier analysis, proposed by Fras *et al.* [64], assumes that heat transfer takes place by conduction only and considers the effect of thermal gradient during solidification. Equation (1. 6) is the Fourier heat equation with a heat source:

$$\frac{\partial T}{\partial t} = \alpha \cdot \nabla^2 T + \frac{1}{\rho \cdot c_p} \cdot \frac{\partial Q}{\partial t} \tag{1. 6}$$

where α $[m^2/s]$ is the thermal diffusivity and ρ $[kg/m^3]$ is the density of the metal. Similarly to the Newtonian method, by assuming $\partial Q/\partial t = 0$ in Equation (1. 6), the baseline equation results in Equation (1. 7):

$$\frac{\partial T}{\partial t}_F = \alpha \cdot \nabla^2 T \tag{1. 7}$$

In the case of the Fourier analysis, the temperature field in the sample is necessary information to calculate the baseline, and thus at least two thermocouples are employed. An iterative procedure is necessary for the determination of thermal diffusivity and specific heat capacity during solidification, and thus to calculate solid fraction and latent heat.

The Newtonian method is convenient to determine the solid fraction dependence on temperature or time. The Fourier method stems from the drawbacks of the Newtonian approach, the main one being the fact that the single thermocouple does not record the temperature gradients in the casting. Secondly, the baseline is arbitrarily fitted with a suitable equation, while the Fourier analysis overcomes this issue because the temperature field in the metal is known. Several studies [64], [69], [71], [72] reported that the predicted baselines, latent heat and solid fraction differ significantly since Fourier analysis is an excellent improvement of the Newtonian method. The significant difference in the calculation of solid fraction mirrors the one in the shape of the baseline, evident in Figure 1. 14a-b.

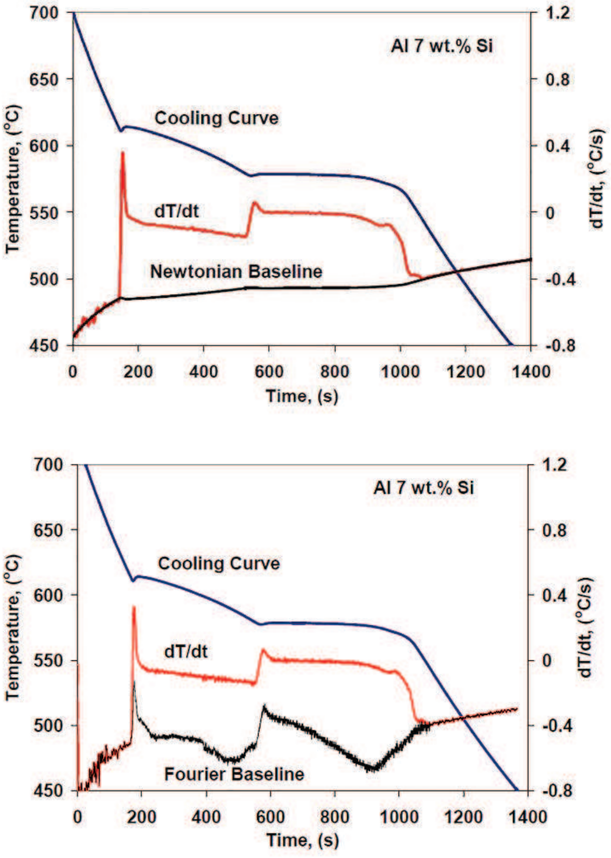

Figure 1. 14 – Comparison of a) Newtonian and b) Fourier baselines for an AlSi7Mg alloy [71]

Similarly, the Fourier technique is more reliable in latent heat prediction than the Newtonian one because it relies on the actual temperature field of the metal. Nevertheless, in foundry practice, where fast answers are needed, the single thermocouple technique is valuable and provides reasonably accurate results also with further computer-aided analysis.

The present paragraph deepens the Newtonian analysis and how to interpret the thermal parameters. Figure 1. 15 reports as an example the cooling curve of an AlSi7Mg alloy, with the related first and second derivatives.

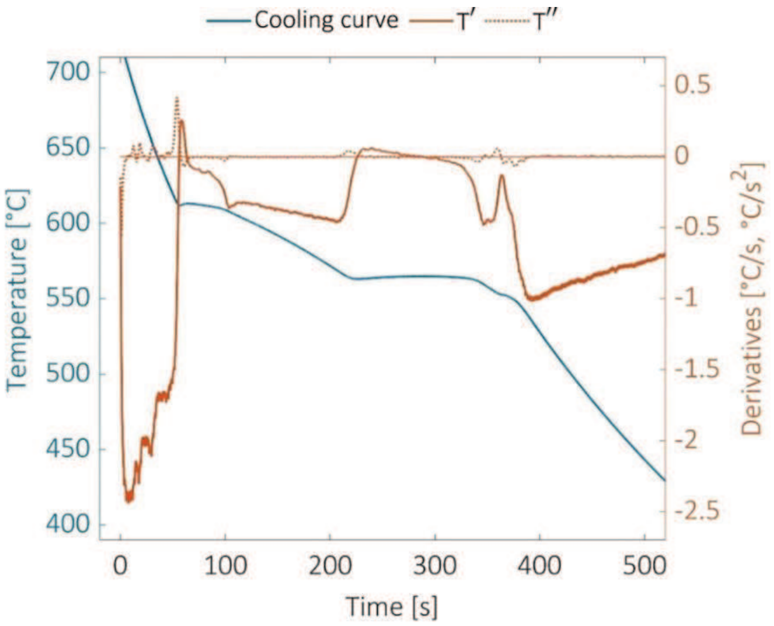

Figure 1. 15 – Cooling curve and related derivatives

The peaks of the first derivative highlight three main solidification reactions that lead to the three main microstructural constituents of the alloy: primary α-Al dendrites, Al-Si eutectic and Mg_2Si phase. The arrests of the first derivative correspond to the thermal arrests that occur during the solidification of a new phase. The peaks of the second derivatives point out the change in the slope of the first derivatives, and the literature reports that this change corresponds to the beginning of nucleation events [73].

Cooling rate has a critical role on the appearance of the cooling curve of an alloy. Its effect in evident in Figure 1. 16 for an AlSi8Cu2 alloy investigated by Zamani and Seifeddine [74].

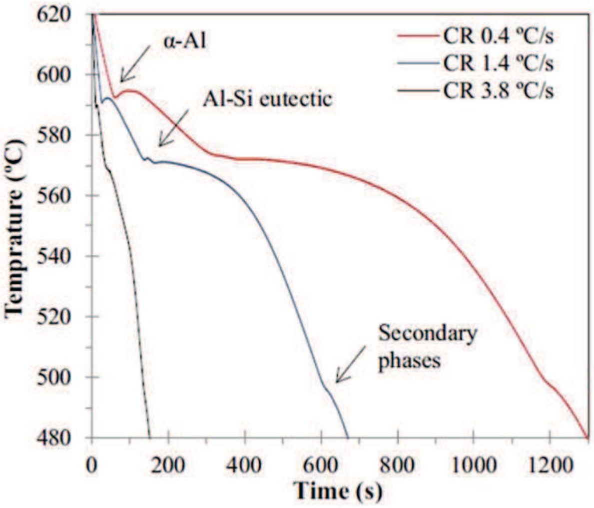

Figure 1. 16 – Cooling curves of an AlSi8Cu2 alloy solidified with different cooling rates [74]

The higher the cooling rate, the steeper the solidification curve. It also becomes harder to distinguish the formation peaks of the different phases.

Several authors report that an extimation of the baseline is possible by appropriate fitting [69], [71], [75]–[77]. The experimental data before *liquidus* temperature and after *solidus* temperature are interested only by convection cooling, can be fitted either by exponential, polynomial or logarithmic equations [69], [76]. The integration of the cumulative area between the first derivative and the baseline (Figure 1. 17a) gives the evolution of solid fraction during solidification (Figure 1. 17b), as anticipated in the description of the methods for thermal analysis. Figure 1. 17b also highlights the differences in the solid fraction trends calculated via Fourier and Newtonian methods.

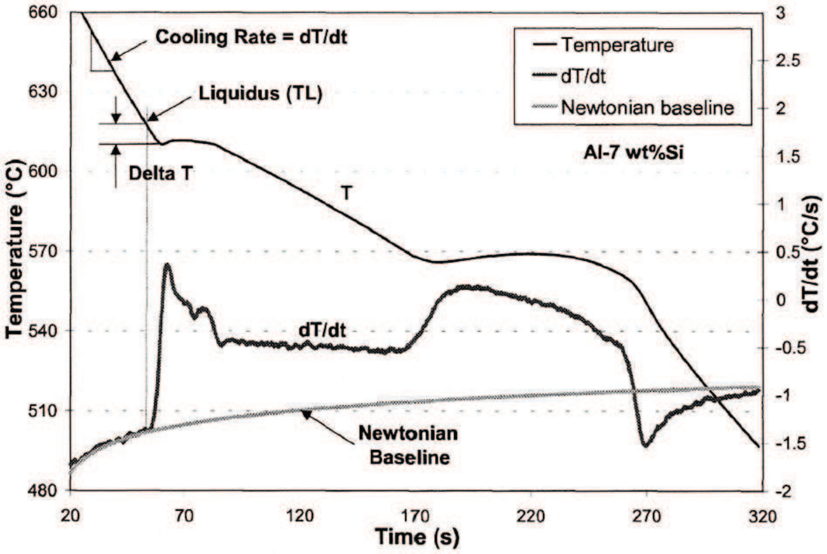

a)

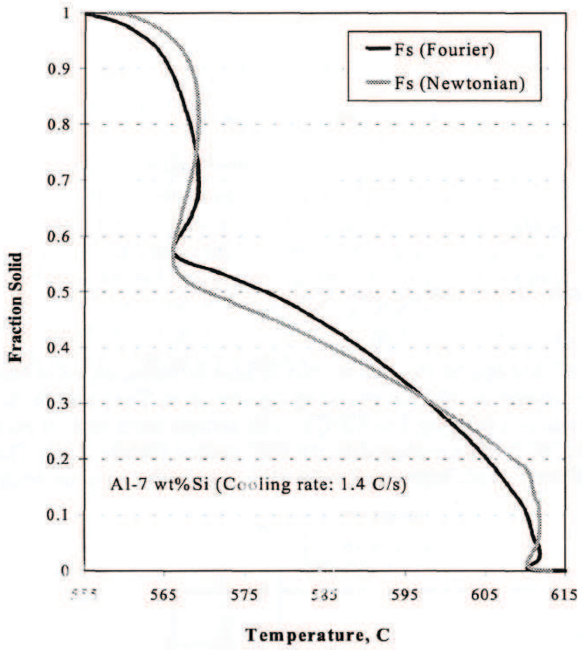

b)

Figure 1. 17 – a) Cooling curve, first derivative and Newtonian baseline of an AlSi7 alloy; b) related evolution of solid fraction with temperature [72]

Nucleation, minimum and growth temperatures (in Figure 1. 18a are indicated as T_N, T_M and T_G respectively) are the thermal parameters that characterise the primary α-Al solidification. The nucleation temperature is the one that corresponds to the positive local peak of the second derivative. The minimum temperature is the value that matches the first local zero of the first derivative. The literature usually defines the growth temperature as the maximum value that follows the minimum temperature. The values of these temperatures reveal to the expert user if refiners are present in the melt and at what extent they operated. The variation of the recalescence value, defined as $\Delta T_R = T_G - T_M$, is a used method to quantify grain refinement [78].

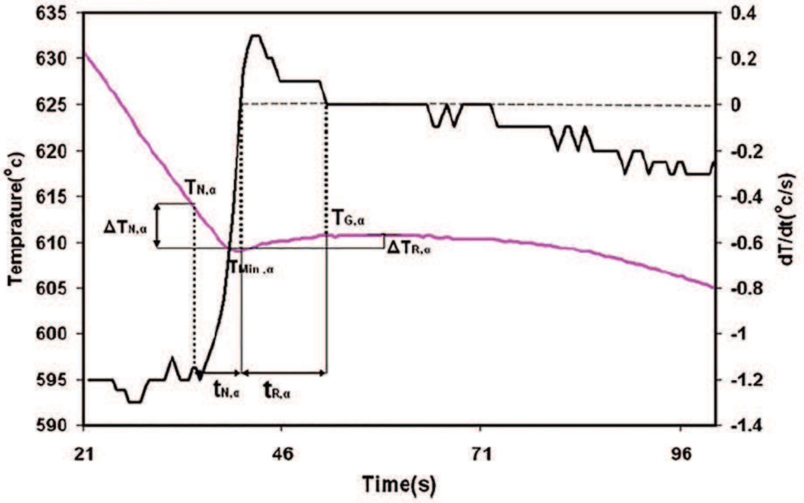

a)

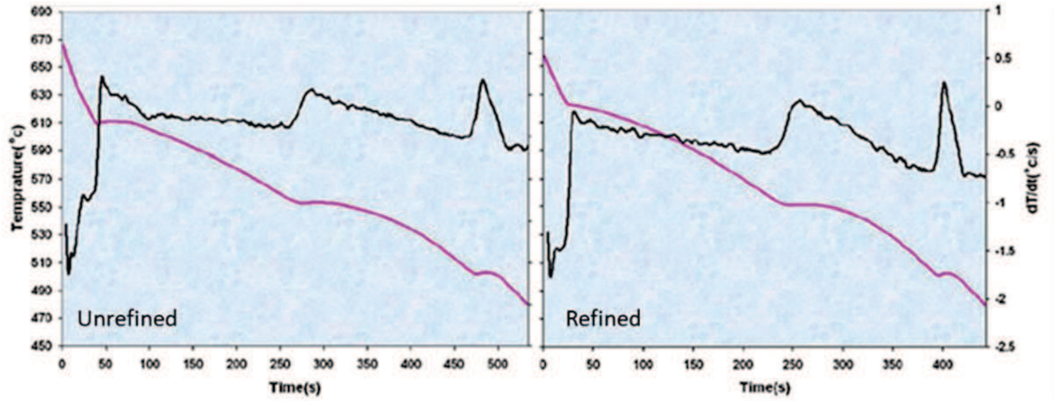

b)

Figure 1. 18 – Primary α-Al solidification in an AlSi6Cu3 alloy: a) cooling curve and first derivative; b) effect of grain refining on the cooling curve [78]

As depicted in Figure 1. 18b, a well-performed grain refining determines an increase of T_N and T_M. At the same time, ΔT_R significantly decreases or eventually disappears in well-refined alloys. The reason is that an ideal heterogeneous nucleation site would reduce the undercooling to the lowest possible value and promote the formation of nuclei earlier, meaning higher T_N. The difference between the growth and the nucleation temperatures is sometimes used to assess grain refining efficiency [79]. If the nucleation of the primary α-Al starts above the steady-state growth temperature, new crystals can form in the liquid ahead of the growing crystal; therefore, grain refining occurs.

The dendrite coherency point (DCP) is also a useful parameter to predict the soundness of the alloy. It is detectable with the cooling curve analysis [64], [69], [80]. The DCP marks the transition from mass feeding to interdendritic feeding during solidification, and after macrosegregation, shrinkage and hot tearing defects begin to appear. DCP can be measured through mechanical methods that measure the torque necessary to rotate a paddle, but its determination via thermal analysis is faster and less time-consuming. Figure 1. 19a illustrates the single thermocouple method to detect DCP, as proposed by Djurdjevic *et al.* [80]. The first step is to plot the cooling curve and its first derivative versus temperature, as depicted in Figure 1. 19a. The authors report that the first derivative presents a loop in the region of dendritic solidification, and the point where it deviates from the horizontal tangent is the DCP temperature (point B in Figure 1. 19b). The authors also verified that the DCP temperature determined with the single thermocouple method is identical to the value obtained with the two-thermocouple methodology (point A in Figure 1. 19b).

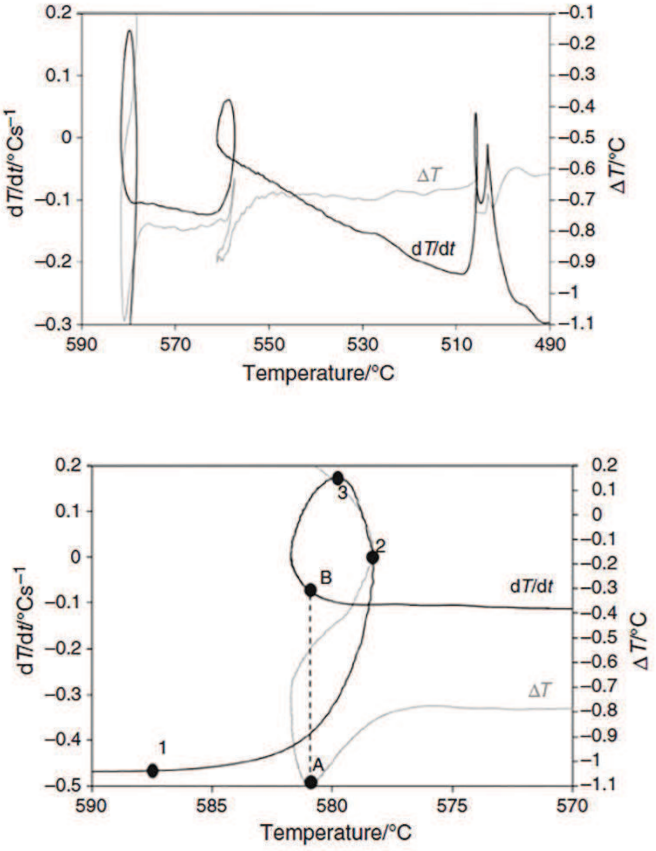

b)

Figure 1. 19 – Primary α-Al solidification in an AlSi9Cu4 alloy: determination of the dendrite coherency point. a) superimposed ΔT and dT/dt; b) magnification of the DCP event [80]

For what concerns the eutectic solidification, calculations similar to the ones employed for primary α-Al are useful to determine nucleation, minimum and growth temperature as well as recalescence, depicted in Figure 1. 20a. The literature reports that modifying agents determine a decrease of T_G in comparison with the growth temperature of unmodified alloy T_{G0}. The magnitude of the parameter $\Delta T_R = T_{G0} - T_G$ quantifies the success of modification [81]–[84].

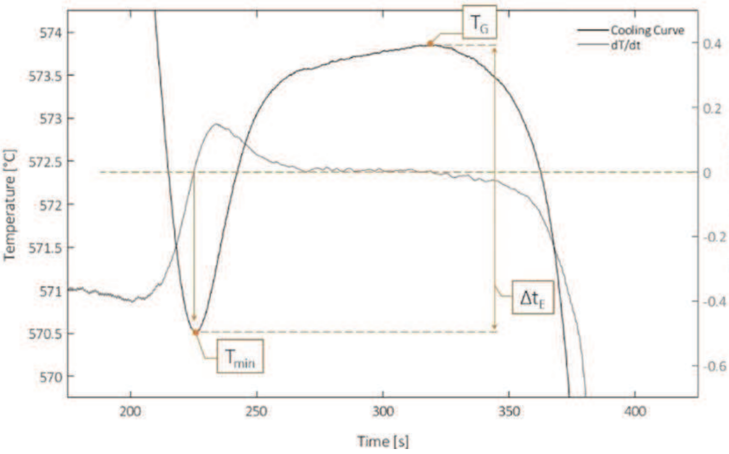

a)

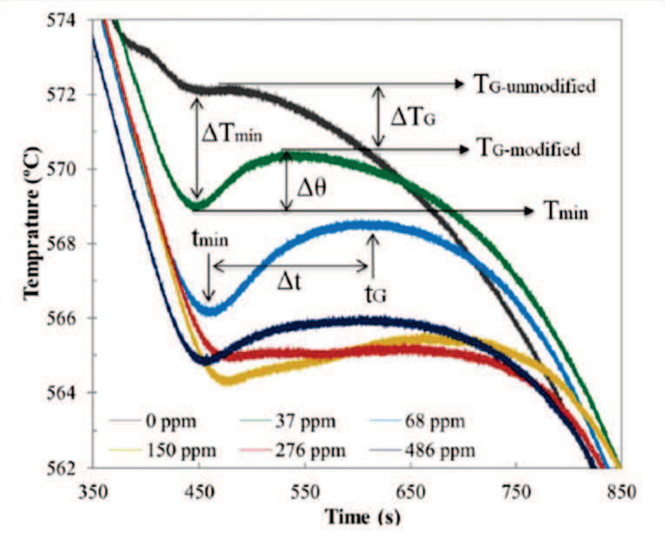

b)

Figure 1. 20 – Eutectic solidification: a) cooling curve and first derivative [85]; b) effect of Sr additions on the cooling curve [74]

As anticipated in § 1.2.2, the decrease of eutectic temperatures corresponds to the refinement of Si particles. Only when a modifying element is present in the alloy, the ΔT_R can also be related to the flake-fibre transition of eutectic Si. The quantity of modifier, nevertheless, is not directly correlated with the magnitude of ΔT_R.

Knuutinen *et al.* [86] investigated the effect of various modifiers via thermal analysis and reported different behaviours. Figure 1. 21 depicts that the addition of Ba, Ca, Y and Yb determine a decrease of the eutectic growth temperature. The initial addition of Ca and Y leads to an immediate drop of T_G and a further increase in concentration do not have a significant influence. The decrease of eutectic growth temperature is gradual, with consecutive additions of Ba and Yb. Although all elements reduce the growth temperature and produce Si refinement, the eutectic morphology is significantly different [26]. These details indicate that there is not a direct relationship between eutectic T_G and eutectic morphology. Thus, it is crucial to have in mind the elements present in the alloy and their influence of the solidification curve.

The addition of Ba, Ca, Y, and Yb also causes the development of a significant recalescence $\Delta T_R = T_G - T_M$ before eutectic growth [86] and the decrease of eutectic T_N [26]. These phenomena indicate that modifying elements have an influence also on the eutectic nucleation, not only on eutectic Si growth.

Alloying elements have specific effects on the cooling curve of an alloy, and they also interfere with each other in multi-component alloys. For this reason, it is critical to interpret the effect of each element correctly and to deepen the thermal analysis of the specific multi-component alloys of interest.

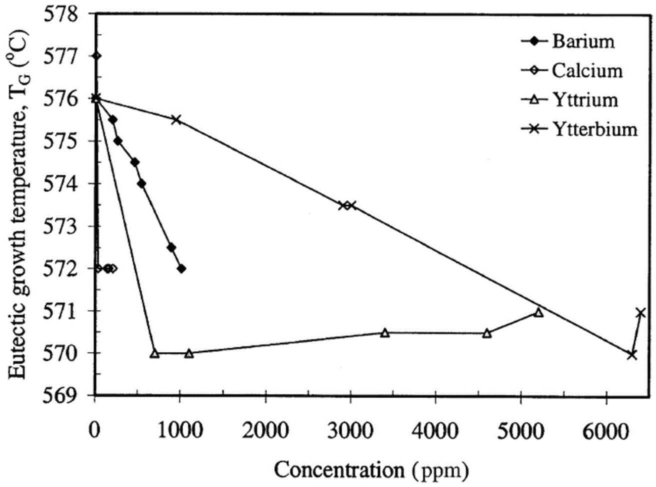

Figure 1. 21 – Eutectic growth temperature v. concentration of the elements investigated by Knuutinen *et al.* [86]

Talking about AlSi7 alloys, Mg and Cu are often added to increase the strength of the alloy because they determine the precipitation of reinforcing phases. Specific heat treatments that consist of solution treatment and ageing enhance the strengthening effect of these intermetallic compounds, by their dispersion into fine precipitates in the matrix. The addition of Mg to an AlSi7 alloy leads to the precipitation of β-Mg_2Si, which occurs after the eutectic solidification. On the cooling curve, a small peak is detectable (Figure 1. 22) after the eutectic region, and it corresponds to the solidification of β-Mg_2Si.

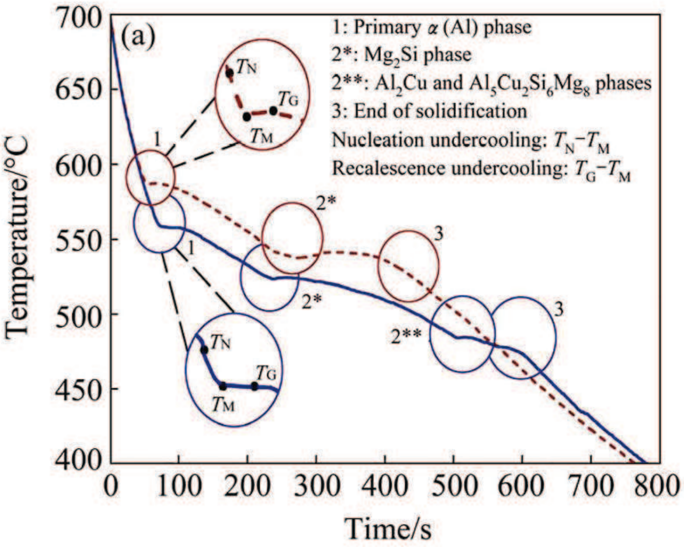

Figure 1. 22 – Effect of alloying elements on the cooling curve of an AlSi7Mg alloy: Mg leads to the solidification of Mg_2Si (dashed line); Cu lowers the cooling curve and forms Cu-based compounds (solid line) [60]

For a binary AlSi7 alloy, the primary solidification occurs at 614 °C according to the phase diagram, and the eutectic reaction follows at 577 °C (Figure 1. 13). Figure 1. 23 depicts the influence of Mg on the phase diagram of the AlSi alloys, as it lowers the transformation temperatures and leads to the formation of a eutectic solidification interval. The presence of Mg lowers the eutectic T_G to 570 °C, and for this reason, it has been considered a modifying agent [50].

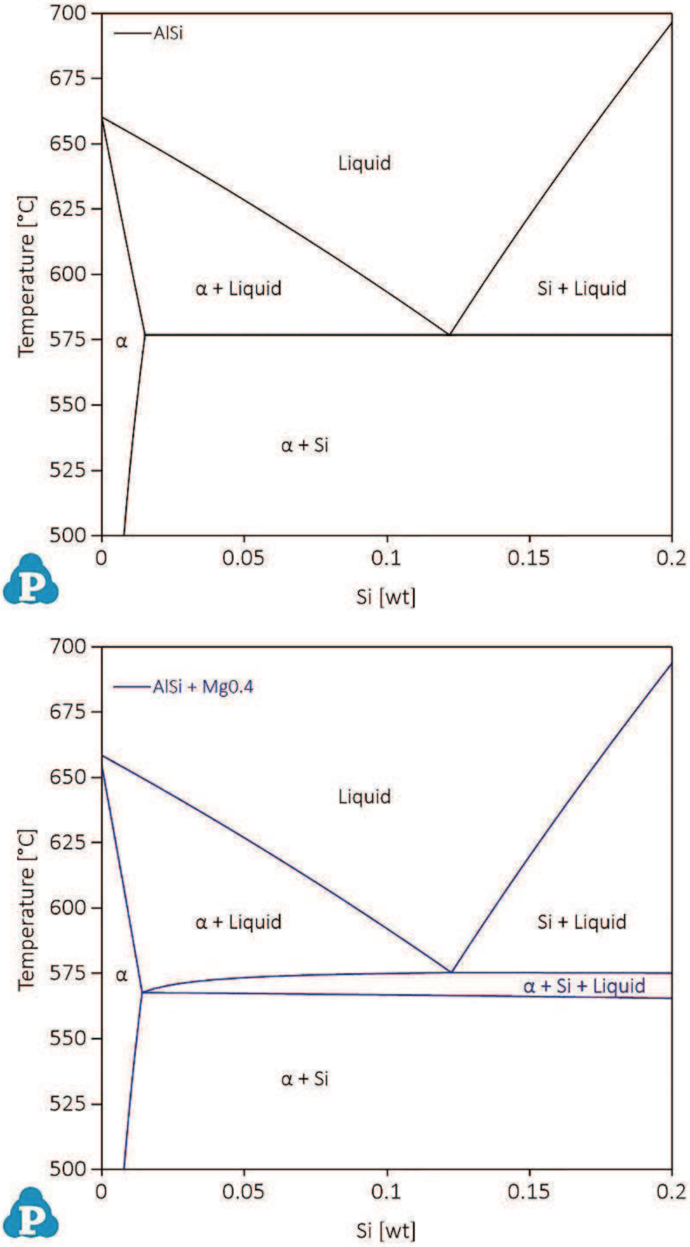

Figure 1. 23 – Comparison of AlSi and AlSi + Mg0.4 phase diagram sections: the presence of Mg transforms the eutectic temperature in the eutectic temperature interval

For what concerns Cu, it determines the formation of θ-Al_2Cu and Q-$Al_5Mg_8Si_6Cu_2$ when co-present with Mg. The peaks on the cooling curves indicate the solidification of these new phases. Cu also moves the entire solidification to lower temperatures [52], [55], [60], [87], [88], as depicted in Figure 1. 22, and thus it can be mistaken as a modifying agent [50]. As presented for primary α-Al and eutectic, it is also possible to determine the nucleation temperature for intermetallic compounds looking for the corresponding peak of the second derivative.

When a modifier agent is added to multi-components alloys, it might also interact with the solidification of intermetallic compounds [89]. For example, in AlSi7MgCu alloys it intensifies specific post-eutectic reactions that involve Cu but covers some Mg-related post-eutectic reactions by shifting the eutectic solidification to lower temperatures. Some authors report that Sr affects the morphology of the Cu-based compounds. It promotes the presence of polygonal θ-Al_2Cu particles over the eutectic ones and increases the amount of fine Q-$Al_5Mg_8Si_6Cu_2$ particles [90]–[93]. The correct interpretation of cooling curves strongly depends on the knowledge about the alloying elements present in the investigated system.

The integration of the cumulative area between the first derivative and the baseline, Figure 1. 17, gives the evolution of solid fraction during solidification, depicted in. With the help of nucleation temperatures obtained for each phase, also the amount of each phase that precipitates as temperature decreases can be calculated (Figure 1. 24). According to previous research, the results obtained via thermal analysis are a reasonable estimation of the metallographic measures [94].

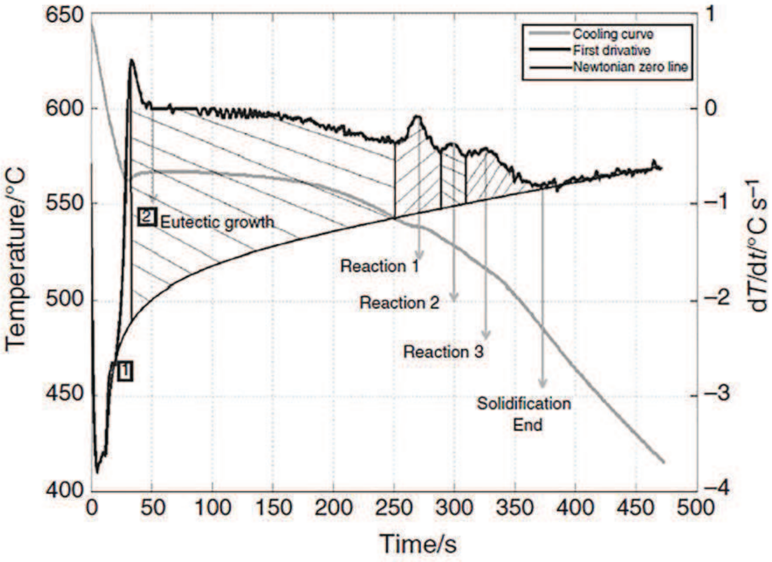

Figure 1. 24 – Solidification reactions of an AlSi12 alloy [76]

In conclusion, thermal analysis provides information about the temperature parameters related to the solidification of both primary α-Al and Al-Si eutectic phases. Therefore it can be helpful to examine the melt quality and to evaluate the goodness of grain refinement and modification treatments before casting. Nevertheless, various experimental parameters influence the result of thermal analysis, and it is crucial to take them into account when discussing the results. Cooling rate, melt and crucible temperature, alloying and trace elements have a significant influence on the solidification of an alloy. Thus, for practical applications, strong background knowledge is necessary to analyse the cooling curves correctly and to make comparisons.

Commercial thermal analysis systems simplify the process using a reference temperature as an input, calculated with empirical equations from the literature that consider the influence of alloying elements on solidification temperatures. In this way, thermal analysis can be available also in foundry practice for untrained users, but the results are general and can mislead to wrong considerations about the alloy.

REFERENCES

[1] M. Easton and D. Stjohn, *Grain refinement of aluminum alloys: Part I. The nucleant and solute paradigms - a review of the literature*, Metall. Mater. Trans. A Phys. Metall. Mater. Sci., vol. **30**, no. 6, pp. 1613–1623, 1999

[2] Cibula A., *The mechanism of grain refinement of sand castings in aluminium alloys*, J. Inst. Met., vol. **76**, pp. 321–360, 1950

[3] Cibula A., *The grain refinement of aluminium alloy castings by additions of titanium and boron*, J. Inst. Met., vol. **80**, pp. 1–19, 1951

[4] F. A. Crossley and L. F. Mondolfo, *Mechanism of Grain Refinement in Aluminum Alloys*, Jom, vol. **3**, no. 12, pp. 1143–1148, 1951

[5] P. S. Mohanty and J. E. Gruzleski, *Mechanism of grain refinement in Aluminium*, Acta Met. Mater., vol. **43**, no. 5, pp. 2001–2012, 1995

[6] L. Bäckerud, P. Gustafson, and M. Johnsson, *Grain refining mechanisms in aluminium as a result of additions of titanium and boron, Part II*, Aluminium, vol. **67**, pp. 910–915, 1991

[7] L. Arnberg, L. Bäckerud, and H. Klang, *Intermetallic particles in Al–Ti–B–type master alloys for grain refinement of aluminium*, Met. Technol., vol. **9**, no. 1, pp. 7–13, 1982

[8] P. Schumacher and A. L. Greer, *Studies of the action of grain-refining particles in aluminium alloys*, Light Met., vol. **17**, pp. 869–877, 1995

[9] G. K. Sigworth, *Communication on mechanism of grain refinement in aluminum*, Scr. Mater., vol. **34**, no. 6, pp. 919–922, 1996

[10] P. S. Mohanty and J. E. Gruzleski, *Grain refinement mechanisms of hypoeutectic Al-Si alloys*, Acta Mater., vol. **44**, no. 9, pp. 3749–3760, 1996

[11] M. Johnsson and L. Bäckerud, *Nucleants in grain refined aluminium after addition of Ti- and B-containing master alloys*, Z. Met., vol. **83**, no. 11, pp. 774–780, 1992

[12] K. E. Knipling, D. C. Dunand, and D. N. Seidman, *Criteria for developing castable, creep-resistant aluminum-based alloys - A review*, Int. J. Mater. Res., vol. **97**, no. 3, pp. 246–265, 2006

[13] I. Maxwell and A. Hellawell, *A simple model for grain refinement during solidification*, Acta Metall., vol. **23**, pp. 229–237, 1975

[14] M. Easton and D. StJohn, *Grain refinement of aluminum alloys: Part II. Confirmation*

of, and a mechanism for, the solute paradigm, Metall. Mater. Trans. A Phys. Metall. Mater. Sci., vol. **30**, no. 6, pp. 1625–1633, 1999

[15] H. Zhao, Y. Song, M. Li, and S. Guan, *Grain refining efficiency and microstructure of Al-Ti-C-RE master alloy*, J. Alloys Compd., vol. **508**, no. 1, pp. 206–211, 2010

[16] F. Wang, D. Qiu, Z. L. Liu, J. A. Taylor, M. A. Easton, and M. X. Zhang, *The grain refinement mechanism of cast aluminium by zirconium*, Acta Mater., vol. **61**, no. 15, pp. 5636–5645, 2013

[17] H. Li, D. Li, Z. Zhu, and B. Chen, *Grain refinement mechanism of as-cast aluminum by hafnium*, Trans. Nonferrous Met. Soc. China, vol. **26**, no. 12, pp. 3059–3069, 2016

[18] U. Patakham, J. Kajornchaiyakul, and C. Limmaneevichitr, *Grain refinement mechanism in an Al-Si-Mg alloy with scandium*, J. Alloys Compd., vol. **542**, pp. 177–186, 2012

[19] L. Bolzoni, M. Nowak, and N. Hari Babu, *Assessment of the influence of Al-2Nb-2B master alloy on the grain refinement and properties of LM6 (A413) alloy*, Mater. Sci. Eng. A, vol. **628**, pp. 230–237, 2015

[20] L. M. Hogan and M. Shamsuzzoha, *Crystallography of the flake-fibre transition in the Al-Si eutectic*, Mater. Forum, vol. **10**, no. 4, pp. 270–277, 1987

[21] S. Khan and R. Elliott, *Quench modification of aluminium-silicon eutectic alloys*, J. Mater. Sci., vol. **31**, no. 14, pp. 3731–3737, 1996

[22] A. Mazahery and M. O. Shabani, *Modification mechanism and microstructural characteristics of eutectic si in casting Al-Si Alloys: A review on experimental and numerical studies*, Jom, vol. **66**, no. 5, pp. 726–738, 2014

[23] K. Fujiwara, K. Maeda, N. Usami, and K. Nakajima, *Growth mechanism of Si-faceted dendrites*, Phys. Rev. Lett., vol. **101**, no. 5, pp. 1–4, 2008

[24] a. Hellawell and S.-Z. Lu, *The mechanism of silicon modification in aluminum-silicon alloys: Impurity induced twinning*, Metall. Trans. A, vol. **18**, no. 10, pp. 1721–1733, 1987

[25] A. Knuutinen, K. Nogita, S. D. McDonald, and A. K. Dahle, *Modification of Al-Si alloys with Ba, Ca, Y and Yb*, J. Light Met., vol. **1**, no. 4, pp. 229–240, 2001

[26] K. Nogita, A. Knuutinen, S. D. McDonald, and A. K. Dahle, *Mechanisms of eutectic solidification in Al-Si alloys modified with Ba, Ca, Y and Yb*, J. Light Met., vol. **1**, no. 4, pp. 219–228, 2001

[27] K. Nogita, S. D. McDonald, and A. K. Dahle, *Eutectic Modification of Al-Si Alloys with Rare Earth Metals*, Mater. Trans., vol. **45**, no. 2, pp. 323–326, 2004

[28] K. Nogita *et al.*, *Determination of strontium segregation in modified hypoeutectic Al – Si alloy by micro X-ray fluorescence analysis*, Scr. Mater., vol. **55**, pp. 787–790, 2006

[29] M. Timpel *et al.*, *The role of strontium in modifying aluminium-silicon alloys*, Acta Mater., vol. **60**, no. 9, pp. 3920–3928, 2012

[30] J. H. Li, M. Albu, F. Hofer, and P. Schumacher, *Solute adsorption and entrapment during eutectic Si growth in A-Si-based alloys*, Acta Mater., vol. **83**, pp. 187–202, 2015

[31] J. H. Li and P. Schumacher, *Effect of Y addition and cooling rate on refinement of eutectic Si in Al-5 wt-%Si alloys*, Int. J. Cast Met. Res., vol. **25**, no. 6, pp. 347–357, 2012

[32] K. Nogita *et al.*, *The role of trace element segregation in the eutectic modification of hypoeutectic Al-Si alloys*, J. Alloys Compd., vol. **489**, pp. 415–420, 2010

[33] J. H. Li *et al.*, *Modification of eutectic Si in Al-Si alloys with Eu addition*, Acta Mater., vol. **84**, pp. 153–163, 2015

[34] J. Barrirero *et al.*, *Eutectic modification by ternary compound cluster formation in Al-Si alloys*, Sci. Rep., vol. **9**, no. 1, pp. 1–10, 2019

[35] S. Moniri, X. Xiao, and A. J. Shahani, *The mechanism of eutectic modification by trace impurities*, Sci. Rep., vol. **9**, no. 1, pp. 1–13, 2019

[36] A. K. Dahle, K. Nogita, J. W. Zindel, S. D. McDonald, and L. M. Hogan, *Eutectic nucleation and growth in hypoeutectic Al-Si alloys at different strontium levels*, Metall. Mater. Trans. A Phys. Metall. Mater. Sci., vol. **32**, no. 4, pp. 949–960, 2001

[37] S. D. McDonald, K. Nogita, and A. K. Dahle, *Eutectic nucleation in Al-Si alloys*, Acta Mater., vol. **52**, no. 14, pp. 4273–4280, 2004

[38] S. D. McDonald, K. Nogita, and A. K. Dahle, *Eutectic grain size and strontium concentration in hypoeutectic aluminium-silicon alloys*, J. Alloys Compd., vol. **422**, no. 1–2, pp. 184–191, 2006

[39] Y. H. Cho, H.-C. Lee, K. H. Oh, and A. K. Dahle, *Effect of strontium and phosphorus on eutectic Al-Si nucleation and formation of β-Al5FeSi in hypoeutectic Al-Si foundry alloys*, Metall. Mater. Trans. A, vol. **39A**, no. 10, pp. 2435–2448, 2008

[40] L. Lu, K. Nogita, S. D. McDonald, and A. K. Dahle, *Eutectic solidification and its role in casting porosity formation*, Jom, vol. **56**, no. 11, pp. 52–58, 2004

[41] S. D. McDonald, A. K. Dahle, J. A. Taylor, and D. H. StJohn, *Eutectic grains in unmodified and strontium-modified hypoeutectic aluminum-silicon alloys*, Metall. Mater. Trans. A Phys. Metall. Mater. Sci., vol. **35 A**, no. 6, pp. 1829–1837, 2004

[42] A. M. Samuel, H. W. Doty, S. V. Gallardo, and F. H. Samuel, *The effect of Bi-Sr and Ca-Sr interactions on the microstructure and tensile properties of Al-Si-based alloys*, Materials (Basel)., vol. **9**, no. 3, 2016

[43] J. Rakhmonov, G. Timelli, and G. Basso, *Interaction of Ca, P trace elements and Sr modification in AlSi5Cu1Mg alloys*, J. Therm. Anal. Calorim., vol. **133**, pp. 123–133, 2018

[44] S. El-Hadad, A. M. Samuel, F. H. Samuel, H. W. Doty, and S. Valtierra, *Effects of Bi and Ca addition on the characteristics of eutectic Si particles in Sr-modified 319 alloys*, Int. J. Cast Met. Res., vol. **15**, no. 5, pp. 551–564, 2003

[45] S. S. Sreeja Kumari, R. M. Pillai, T. P. D. Rajan, and B. C. Pai, *Effects of individual and combined additions of Be, Mn, Ca and Sr on the solidification behaviour, structure and mechanical properties of Al-7Si-0.3Mg-0.8Fe alloy*, Mater. Sci. Eng. A, vol. **460–461**, pp. 561–573, 2007

[46] S. S. Sreeja Kumari, R. M. Pillai, K. Nogita, A. K. Dahle, and B. C. Pai, *Influence of calcium on the microstructure and properties of an Al-7Si-0.3Mg-xFe alloy*, Metall. Mater. Trans. A, vol. **37**, no. 8, pp. 2581–2587, 2006

[47] C. H. Caceres, C. J. Davidson, Q. G. Wang, and J. R. Griffiths, *The effect of Mg on the microstructure and mechanical behavior of Al-Si-Mg casting alloys*, Metall. Mater. Trans. A, vol. **30**, no. 10, pp. 2611–2618, 1999

[48] A. Darlapudi, S. D. McDonald, and D. H. StJohn, *The influence of Cu, Mg and Ni on the solidification and microstructure of Al-Si alloys*, IOP Conf. Ser. Mater. Sci. Eng., vol. **117**, no. 1, pp. 1–7, 2016

[49] I. Aguilera-Luna, M. J. Castro-Román, J. C. Escobedo-Bocardo, F. A. García-Pastor, and M. Herrera-Trejo, *Effect of cooling rate and Mg content on the Al-Si eutectic for Al-Si-Cu-Mg alloys*, Mater. Charact., vol. **95**, pp. 211–218, 2014

[50] L. Heusler and W. Schneider, *Influence of alloying elements on the thermal analysis results of Al-Si cast alloys*, J. Light Met., vol. **2**, no. 1, pp. 17–26, 2002

[51] A. T. Joenoes and J. E. Gruzleski, *Magnesium effects on the microstructure of unmodified and modified AlSi alloys*, Cast Met., vol. **4**, no. 2, pp. 62–71, 1991

[52] G. Heiberg, K. Nogita, A. L. Dons, A. K. Dahle, and L. Arnberg, *Effect of magnesium, iron and copper on eutectic solidification of hypoeutectic aluminum-silicon alloys*, AFS Trans., pp. 347–358, 2002

[53] G. Heiberg, K. Nogita, A. K. Dahle, and L. Arnberg, *Columnar to equiaxed transition of eutectic in hypoeutectic aluminium-silicon alloys*, Acta Mater., vol. **50**, no. 10, pp. 2537–2546, 2002

[54] G. Heiberg, C. Gandin, H. Goerner, and L. Arnberg, *Experimental and Modeling Studies of the Thermal Conditions and Magnesium , Iron , and Copper Content on the Morphology of the Aluminum Silicon Eutectic in Hypoeutectic Aluminum Silicon Alloys*, Metall. Mater. Trans. A, vol. **35A**, pp. 2981–2991, 2004

[55] A. Darlapudi, S. D. Mcdonald, and D. H. Stjohn, *The influence of ternary Cu additions on the nucleation of eutectic grains in a hypoeutectic Al-10 wt .% Si alloy*, J. Alloys Compd., vol. **646**, pp. 699–705, 2015

[56] A. Darlapudi, S. D. McDonald, S. Terzi, A. Prasad, M. Felberbaum, and D. H. StJohn, *The influence of ternary alloying elements on the Al-Si eutectic microstructure and the Si morphology*, J. Cryst. Growth, vol. **433**, pp. 63–73, 2016

[57] F. J. Feikus, *Optimization of Al-Si cast alloys for cylinder head applications*, AFS Trans., vol. **98**, no. 61, pp. 225–231, 1998

[58] L. Heusler, F. J. Feikus, and M. O. Otte, *Alloy and Casting Process Optimization for Engine Block Application*, AFS Trans., vol. **50**, pp. 1–9, 2001

[59] A. R. Farkoosh and M. Pekguleryuz, *Enhanced mechanical properties of an Al–Si–Cu–Mg alloy at 300 °C: Effects of Mg and the Q-precipitate phase*, Mater. Sci. Eng. A, vol. **621**, pp. 277–286, 2015

[60] R. Taghiabadi, A. Fayegh, A. Pakbin, M. Nazari, and M. H. Ghoncheh, *Quality index and hot tearing susceptibility of Al−7Si−0.35Mg−xCu alloys*, Trans. Nonferrous Met. Soc. China, vol. **28**, pp. 1275–1286, 2018

[61] S. G. Shabestari and H. Moemeni, *Effect of copper and solidification conditions on the microstructure and mechanical properties of Al–Si–Mg alloys*, J. Mater. Process. Technol., vol. **153–154**, pp. 193–198, 2004

[62] S. Seifeddine, E. Sjölander, and T. Bogdanoff, *On the Role of Copper and Cooling Rates on the Microstructure, Defect Formations and Mechanical Properties of Al-Si-Mg Alloys*, Mater. Sci. Appl., vol. **4**, pp. 171–178, 2013

[63] M. T. Di Giovanni *et al.*, *How Slight Solidification Rate Variations within Cast Plate Affect Mechanical Response : A Study on As-Cast A356 Alloy with Cu Additions*, Adv. Mater. Sci. Eng., vol. **2018**, pp. 1–11, 2018

[64] E. Fras, W. Kapturkiewicz, A. Burbielko, and H. F. Lopez, *A new concept in thermal analysis of castings*, AFS Trans., vol. **93**, no. 131, pp. 505–511, 1993

[65] E. Fras, W. Kapturckiewicz, A. Burbielko, and H. F. Lo, *Numerical Simulation and Fourier Thermal Analysis of Solidification Kinetics in High-Carbon Fe-C Alloys*, Metall. Mater. Trans. B, vol. **28B**, pp. 115–123, 1997

[66] E. Fras, W. Kapturkiewicz, and H. F. Lopez, *The solidification kinetics of cast iron using an improved thermal analysis technique*, Cast Met., vol. **6**, no. 3, pp. 137–142, 1993

[67] I. G. Chen and D. M. Stefanescu, *Computer-aided differential thermal analysis of spheroidal and compacted graphite cast irons*, AFS Trans., vol. **92**, pp. 947–964, 1984

[68] K. G. Upadhya, D. M. Stefanescu, K. Lieu, and D. P. Yeager, *Computer-Aided Cooling Curve Analysis: Principles and Applications in Metal Casting*, AFS Trans., vol. **97**, pp. 61–66, 1989

[69] J. O. Barlow and D. M. Stefanescu, *Computer-Aided Cooling Curve Analysis Revisited*, AFS Trans., vol. **4**, p. 349+354, 1997

[70] A. A. Canales, J. Talamantes-silva, D. Gloria, S. Valtierra, and R. Colás, *Thermal analysis during solidification of cast Al-Si alloys*, Thermochim. Acta, vol. **510**, pp. 82–87, 2010

[71] D. Emadi, L. V Whiting, M. Djurdjevic, W. T. Kierkus, and J. Sokolowski, *Comparison of Newtonian and Fourier thermal analysis techniques for calculation of latent heat and solid fraction of aluminum alloys*, Metalurgija, vol. **3**, pp. 91–106, 2005

[72] D. Emadi and L. V Whiting, *Determination of solidification characteristics of Al-Si alloys by thermal analysis*, AFS Trans., vol. **110**, pp. 285–296, 2002

[73] D. Sparkman, *Microstructure by Thermal Analysis*, AFS Trans., vol. **119**, pp. 1–8, 2011

[74] M. Zamani and S. Seifeddine, *Determination of optimum Sr level for eutectic Si modification in Al-Si cast alloys using thermal analysis and tensile properties*, Int. J. Met., vol. **10**, no. 4, pp. 457–465, 2016

[75] P. Marchwica, J. H. Sokolowski, and W. T. Kierkus, *Fraction solid evolution*

characteristics of AlSiCu alloys - dynamic baseline approach, vol. **47**, no. 2, pp. 115–136, 2011

[76] V. A. Hosseini and S. G. Shabestari, *Study on the eutectic and post-eutectic reactions in LM13 aluminum alloy using cooling curve thermal analysis technique*, J. Therm. Anal. Calorim., vol. **124**, no. 2, pp. 611–617, 2016

[77] J. W. Gibbs and P. F. Mendez, *Solid fraction measurement using equation-based cooling curve analysis*, vol. **58**, pp. 699–702, 2008

[78] S. G. Shabestari and M. Malekan, *Assessment of the effect of grain refinement on the solidification characteristics of 319 aluminum alloy using thermal analysis*, J. Alloys Compd., vol. **492**, no. 1–2, pp. 134–142, 2010

[79] L. Lu and A. K. Dahle, *Effects of combined additions of Sr and AlTiB grain refiners in hypoeutectic Al-Si foundry alloys*, Mater. Sci. Eng. A, vol. **435–436**, pp. 288–296, 2006

[80] M. B. Djurdjevic, J. H. Sokolowski, and Z. Odanovic, *Determination of dendrite coherency point characteristics using first derivative curve versus temperature*, J. Therm. Anal. Calorim., vol. **109**, no. 2, pp. 875–882, 2012

[81] S. Argyropoulos, B. Closset, J. E. Gruzleski, and H. Oger, *The quantitative control of modification in Al-Si foundry alloys using a thermal analysis technique*, AFS Trans., vol. **91**, pp. 351–358, 1983

[82] M. Malekan, D. Dayani, and A. Mir, *Thermal analysis study on the simultaneous grain refinement and modification of 380.3 aluminum alloy*, J. Therm. Anal. Calorim., vol. **115**, no. 1, pp. 393–399, 2014

[83] M. Zamani and S. Seifeddine, *Determination of optimum Sr level for eutectic Si modification in Al-Si cast alloys using thermal analysis and tensile properties*, Int. J. Met., vol. **10**, no. 4, pp. 457–465, 2016

[84] M. S. Abdelrahman, M. T. Abdu, and W. Khalifa, *Assessment of eutectic modification level in Al-Si alloys via thermal analysis*, in *Light Metals 2017*, 2017, pp. 885–895

[85] L. Lattanzi, A. Fortini, M. Giovagnoli, and M. Merlin, *Influence of Mg and Ti on both eutectic solidification and modifying efficiency in Sr-modified Al-7Si cast alloys*, Metall. Ital., vol. **110**, no. 2, pp. 5–15, 2018

[86] A. Knuutinen, K. Nogita, S. D. McDonald, and A. K. Dahle, *Modification of Al-Si alloys with Ba, Ca, Y and Yb*, J. Light Met., vol. **1**, no. 4, pp. 229–240, 2001

[87] C. H. Caceres, M. B. Djurdjevic, T. J. Stockwell, and J. H. Sokolowski, *The effect of*

Cu content on the level of microporosity in Al-Si-Cu-Mg casting alloys, Scr. Mater., vol. **40**, no. 5, pp. 631–637, 1999

[88] M. Zeren, E. Karakulak, and S. Gümüs, *Influence of Cu addition on microstructure and hardness of near-eutectic Al-Si-xCu-alloys*, Trans. Nonferrous Met. Soc. China, vol. **21**, pp. 1698–1702, 2011

[89] M. H. Mulazimoglu, N. Tenekedjiev, B. M. Closset, and J. E. Gruzleski, *Studies on the minor reactions and phasesin strontium-treated aluminium-silicon casting alloys*, Cast Met., vol. **6**, no. 1, pp. 16–28, 1993

[90] F. H. Samuel, A. M. Samuel, and H. W. Doty, *Factors controlling the type and morphology of Cu-containing phases in 319 Al alloy*, AFS Trans., vol. **96**, no. 30, pp. 893–901, 1996

[91] M. Djurdjevic, T. Stockwell, and J. Sokolowski, *The effect of strontium on the microstructure of the aluminium-silicon and aluminium-copper eutectics in the 319 aluminium alloy*, Int. J. Cast Met. Res., vol. **12**, pp. 67–73, 1999

[92] M. H. Mulazimoglu, N. Tenekedjiev, B. M. Closset, and J. E. Gruzleski, *Studies on the minor reactions andphases in Strontium-treated Aluminium-Silicon casting alloys*, Cast Met., vol. **6**, no. 1, pp. 16–28, 1993

[93] P. Ouellet, F. H. Samuel, D. Gloriat, and S. Valtierrat, *Effect of Mg content on the dimensional stability and tensile properties of heat treated Al-Si-Cu (319) type alloys*, Int. J. Cast Met. Res., vol. **10**, pp. 67–78, 1997

[94] M. B. Djurdjevic, I. Vicario, and G. Huber, *Review of thermal analysis applications in aluminium casting plants*, *Revista de Metalurgia*, vol. **50**, no. 1. pp. 1–13, 2014

CHAPTER 2

GRAIN REFINING AND Sr MODIFICATION

The present chapter deals with the experimental work about grin refining and Sr modification. Different levels of grain refinement at different holding times are compared to study the fading phenomenon. For what concerns modification, the focus is the interaction of Sr with either alloying or trace elements commonly present in AlSi7Mg alloys. The aim is to establish if thermal analysis can be a valuable tool in the foundry to predict the quality of grain refining and Sr modification before the final cast.

2.1 AIM AND PURPOSE OF THE WORK

2.1.1 Grain refinement and fading

The literature extensively tackled the use of thermal analysis to verify the efficacy of refiners and the related changes in the solidification parameters observed in the cooling curves [1]–[3]. Conversely, limited published research concerned the grain refiner fading. The purpose of the study is to evaluate how the fading of grain refiners occurs if the melt remains at the same temperature for a prolonged time after their addition. In foundry practice, the fading phenomenon is well-known but yet not thoroughly comprehended. Hence, cooling curves of solidifying specimens after different holding times were employed to relate the thermal parameters of the alloy to the refining efficacy.

2.1.2 Interaction of Sr with alloying and trace elements

Chemical modification of Al-Si alloys is the treatment that alters the morphology of eutectic Si particles from lamellar to fibrous. This treatment aims to reduce the stress concentration factor of the lamellar particles and thus improve the mechanical properties of the alloy. Some studies focused on the assessment of Sr modification via thermal analysis [4]–[7], but the literature pays very little attention to the interaction between modifiers, alloying elements and trace elements [8], [9]. The present study examines the changes in the eutectic solidification of Sr-modified alloys due to the presence of Cu, Mg and Ti, that are the most common alloying elements in AlSi7 systems. Also, the interaction of Sr with Ca is of interest because Ca often occurs in the AlSi melts as an undesirable trace element.

2.2 MATERIALS AND EXPERIMENTAL PROCEDURE

2.2.1 Melt preparation

2.2.1.1 Grain refining and fading

An AlSi7Mg alloy modified with 100 ppm of Sr, but not refined, was considered as reference alloy. Pure Mg and AlTi10 master alloy rods were added to an AlSi7 alloy to reach the targeted Mg and Ti contents of ~ 0.4 wt. % and ~ 0.12 wt. %, respectively. AlSr10 master alloy rods were also added to obtain the targeted Sr content of 100 ppm. The melts (500 kg) were then transferred to a heated ladle and kept at a temperature of 735 ± 15 °C. After the melt transfer, two different quantities of AlTi5B1 rods, *i.e.* 1 rod/100 kg and 3 rods/100 kg of molten metal, and a commercial refining tab were added as refiners. Figure 2. 1a shows an SEM micrograph of the AlTi5B1 master alloy with the related EDS spectra that highlight the presence of polygonal Al_3Ti compounds (Figure 2. 1b, spectrum 16) and dispersed TiB_2 particles (Figure 2. 1b, spectrum 18).

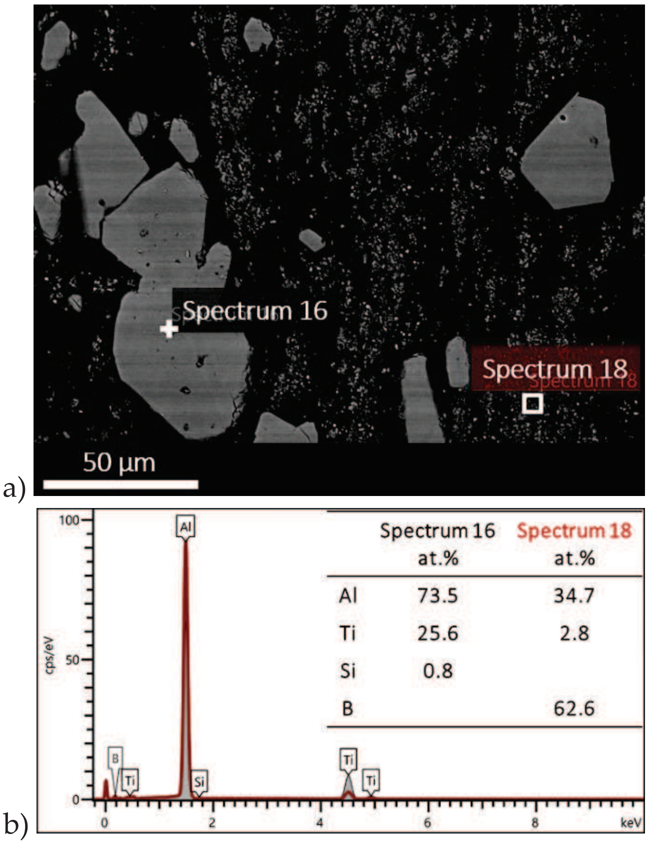

	Spectrum 16 at.%	Spectrum 18 at.%
Al	73.5	34.7
Ti	25.6	2.8
Si	0.8	
B		62.6

Figure 2. 1 – a) SEM micrograph of the AlTi5B1 master alloy and b) related EDS spectra of Al_3Ti and TiB_2

The presence of these microstructural features is further confirmed by literature [10]. Once the refining rod dissolves in the molten metal, the Ti-based intermetallic compounds become available nucleating sites and their refining action begins.

Optical Emission Spectrometer (OES) analyses measured the chemical composition of the alloys, reported in Table 2. 1.

Table 2. 1 – Chemical composition of the alloys investigated for grain refinement [wt.%]

Alloy name	Si	Fe	Mg	Ti	Sr [ppm]	B [ppm]	Al
AlSi7Mg	6.84	0.12	0.45	0.12	107	4	bal.
1-rod	6.91	0.12	0.46	0.13	108	12	bal.
3-rods	7.03	0.13	0.45	0.14	100	52	bal.
Tab	7.21	0.13	0.40	0.12	101	17	bal.

2.2.1.2 Interaction of Sr with alloying elements

In order to investigate the interaction between Sr, Mg, Ti and Cu, five different reference alloys were prepared, listed in Table 2. 2. For the AlSi7 alloy, Al ingots and pure Si rocks were melted in an electric resistance furnace. For the other alloys, pure Cu, pure Mg and the AlTi10 master alloy rods were added to reach the targeted contents of ~ 0.5 wt. % Cu, ~ 0.4 wt. % Mg and ~ 0.12 wt. % Ti. Table 2. 2 reports the chemical composition of the reference alloys, evaluated with OES analyses.

Table 2. 2 – Chemical composition of the alloys for interaction between Sr and the principal alloying elements of AlSi7 family alloys [wt.%]

Alloy name	Si	Fe	Mg	Ti	Cu	Al
AlSi7	6.86	0.10	-	-	-	bal.
AlSi7+Ti	7.55	0.10	-	0.12	-	bal.
AlSi7+Mg	7.16	0.12	0.37	-	-	bal.
AlSi7+MgTi	7.17	0.12	0.37	0.13	-	bal.
AlSI7+CuMgTi	7.29	0.11	0.39	0.13	0.51	bal.

The melts were then transferred to a heated ladle and kept at a temperature of 735 ± 15 °C. After the melt transfer, the addition of AlSr10 master alloy rods led to the targeted Sr contents of 40, 70, 100 and 140 ppm. Figure 2. 2a shows an SEM micrograph of the AlSr10 master alloy with the related EDS spectra that reveal the presence of Sr-rich intermetallic compounds of different size (Figure 2. 2b). The semi-quantitative results suggest the Al_4Sr stoichiometry for the coarse polygonal particles, and this result agrees with previous study [11]. According to the Al-Sr phase diagram [12], the Al_4Sr particles dissolve at ~ 654 °C in the molten bath, and Sr atoms become available for modification.

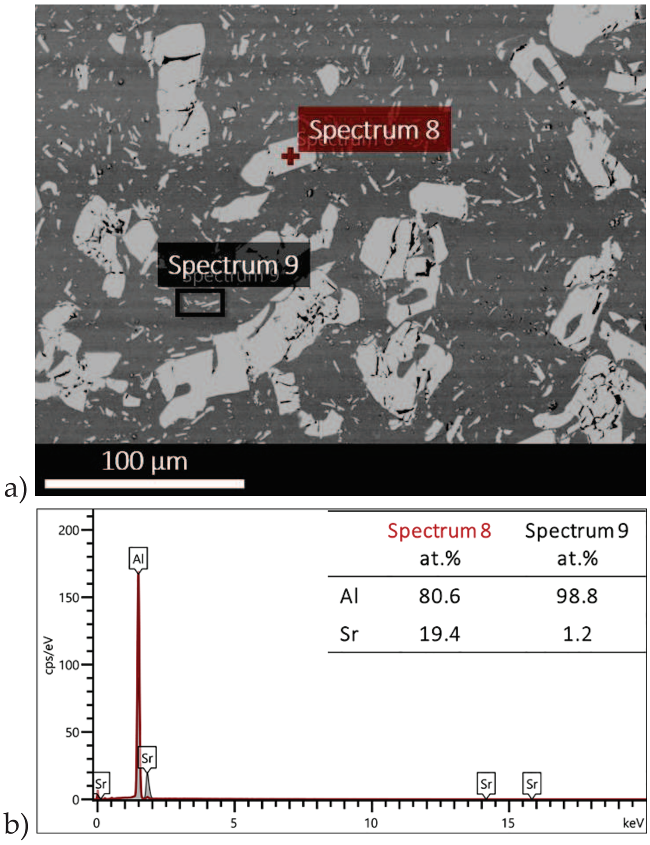

Figure 2. 2 – a) SEM micrograph of the AlSr10 master alloy and b) related EDS spectra of Sr-rich compounds

2.2.1.3 Interaction of Sr with trace elements

For what concerns the interaction of Sr with Ca, four alloys were prepared, and their chemical compositions, evaluated with OES, are reported in Table 2. 3. Primary Al ingots were melted, and pure Si was then added to the bath. AlTi10 master alloy rods and commercially pure Mg were also added to reach the targeted Ti and Mg nominal content of ~ 0.12 wt.% and ~ 0.38 wt.%. Ca targeted contents were reached via the addition of AlCa10 master alloy. The melts were then transferred to a heated ladle and kept at a temperature of 735 ± 15 °C. After the melt transfer, AlSr10 master alloy rods were added to obtain the targeted Sr content of 180 ppm.

Table 2. 3 – Chemical composition of the alloys for interaction between Sr and Ca [wt.%]

Alloy name	Si	Fe	Mg	Ti	Ca [ppm]	Sr [ppm]	Al
AlSi7Mg	7.17	0.12	0.37	0.13	-	-	bal.
Sr 180	7.11	0.12	0.38	0.12	-	180	bal.
Ca 40	7.04	0.12	0.37	0.12	40	176	bal.
Ca 80	7.25	0.12	0.38	0.12	80	182	bal.

All the melts were degassed for 480 s through a rotary degasser supplied with inert nitrogen gas before the addition of refiners, modifiers and other master alloys.

2.2.2 Thermal analysis

The evaluation of the thermal parameters of the investigated alloys is possible by pouring the melts into a pre-heated steel cup (Figure 2. 3). A mineral insulated K-type thermocouple located in the centre of the cup, 15 mm far from the bottom, enables to record the cooling curves.

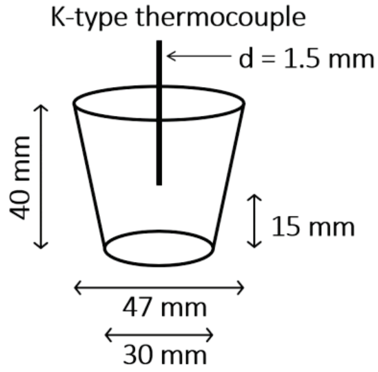

Figure 2. 3 – Schematic of the steel cup for thermal analysis

The thermocouple was placed inside a stainless-steel sheath and then removed from the solidified samples. Temperature and time data were recorded at a frequency of 4 Hz by the data acquisition system Pico Technology TC-08 Thermocouple Data Logger, linked to a personal computer (Figure 2. 4). The acquisition stopped when the temperature reached 400 °C during cooling. The errors in temperature measurements are estimated to be less than 0.5 °C, thanks to calibration in pure Al and binary AlSi7 alloy.

Figure 2. 4 – Experimental setup for thermal analysis

Cooling curves and their derivatives were processed using a tailored Matlab® code. Experimental data processing comprised smoothing, curve fitting and plotting of the first and second derivatives for the determination of the characteristic solidification temperatures. The cooling rate was evaluated in the liquid region before the nucleation of the α-Al primary phase, in the temperature range 630 - 645 °C, and its average value results of 1.5 ÷ 1.6 °C/s. The main solidification parameters of the phases are the minimum temperature T_M, and the growth temperature T_G. Figure 2. 5 displays that T_M is the minimum temperature before recalescence and T_G is the maximum temperature after T_M.

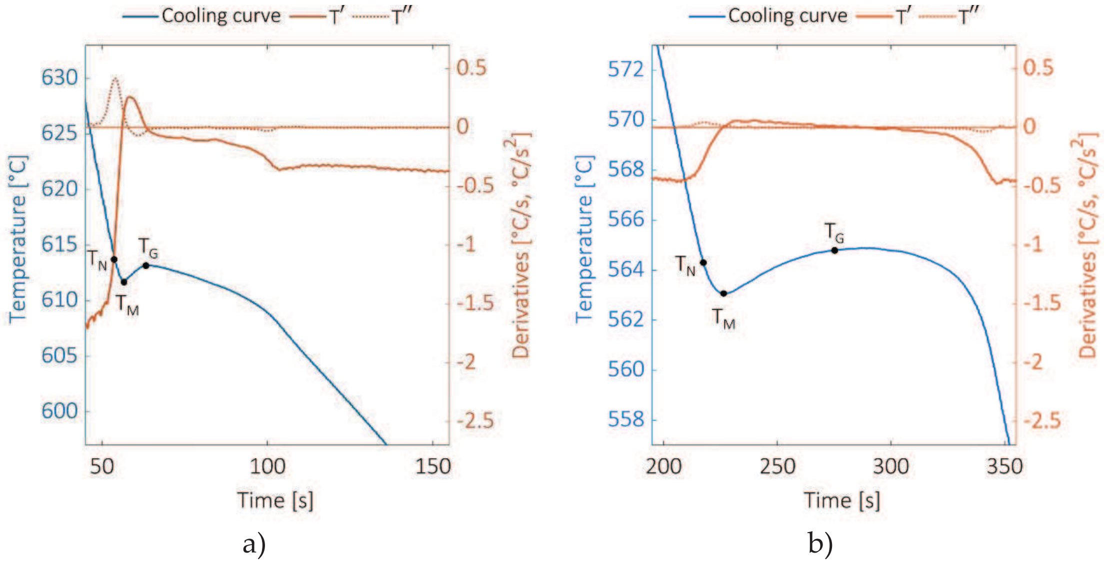

Figure 2. 5 – Thermal analysis parameters: a) primary aluminium solidification; b) eutectic solidification

The recalescence $\Delta T_R = T_G - T_M$ is the difference between growth and minimum temperatures. The eutectic $\Delta T_G = T_{G0} - T_G$ is the difference between the eutectic growth temperature of the unmodified alloy (T_{G0}) and the eutectic growth temperature of the Sr modified one.

2.2.3 Microstructure evaluation

Samples from TA were sectioned transversely to the axis of the thermocouple, and both sections were prepared using standard metallographic procedures. Quantitative IA was performed using a Leica DMi8 A optical microscope (OM), equipped with Leica Application Suite 4.9 image analysis software.

A macro-etch with a 10 wt.% $CuCl_2$ solution was performed to reveal the grain structure. Also, each specimen was anodised with Barker's solution (HBF_4 1.8 wt.%, 30 V for 120 s) and observed under polarised light. Eight composite images assure the investigation of an area that is representative of the entire sample. Each composite image consists of nine micrographs, taken at a magnification of 500x. The evaluation of the average grain size on a minimum of 300 grains for each alloy follows the Heyn lineal intercept procedure of the ASTM E112 standard.

For what concerns Si particles, the region of intrest was a square of 4 mm^2 chosen close to the centre of the sample surface, close to the tip of the thermocouple. Indeed, by the BS ISO 13322-1:2014, a preliminary study was conducted to determine the minimum number of particles to investigate to be representative of the entire sample. The analysis of 400 micrographs enabled to trustworthy identify the distribution of geometrical parameters for the entire population. The minimum number of particles needed results from Equation (2. 1):

$$n^* = \alpha^2 u^2 s^2 (2 \cdot (\beta + 0.5 \cdot \alpha)^2 s^2 + 1) \cdot \delta^{-2} \qquad (2.\ 1)$$

where α and β are constants defined from the geometrical parameter to be measured, s is the standard deviation of the population geometrical parameter, δ is the % relative error, and its value is 5 %, u is an intermediate parameter of 1.96 for a given probability of 95 %. The resulting n^* of 3000 particles ensures a negligible variability of geometrical features of Si particles. To ensure the suitability of the employed optical magnification and the sufficient number of pixels for the smallest particle to be measured, the minimum threshold is 10 pixels. The image analysis covers four composite images of 9 micrographs at a magnification of 500x for each specimen. The investigation area comprised within each composite image is ~ 300000 μm^2. The described method ensured the analysis of a suitable number of particles, comprised within the range of 5000 - 8000 particles. The ImageJ software returns, among various geometrical properties and dimensionless parameters, circularity ($C = 4\pi \cdot \text{area}/\text{perimeter}^2$) and equivalent diameter ($ED = (4 \cdot \text{area}/\pi)^{1/2}$) of eutectic Si particles.

The different secondary phases were observed with a Zeiss EVO MA 15 SEM and identified through EDS.

2.3 RESULTS AND DISCUSSION

2.3.1 Gran refining and fading

The XRD analysis of the refiners in Figure 2. 6 depicts the phases that are present in the AlTi5B1 master alloy and the commercial tab. The intermetallic phases present in the master alloy are titanium diboride TiB_2 and titanium aluminide Al_3Ti (Figure 2. 6a), in line with the EDS spectra of Figure 2. 1b. These intermetallic particles will be involved in the refining of the α-Al primary phase after the addition of the master alloy to the melt. The peaks related to pure Al are also identified. In the refining tab, the principal identified phases are potassium salts (Figure 2. 6b). The most abundant phase seems to be potassium titanium fluoride K_2TiF_6 followed by potassium tetrafluoroborate BF_4K and potassium chloride KCl.

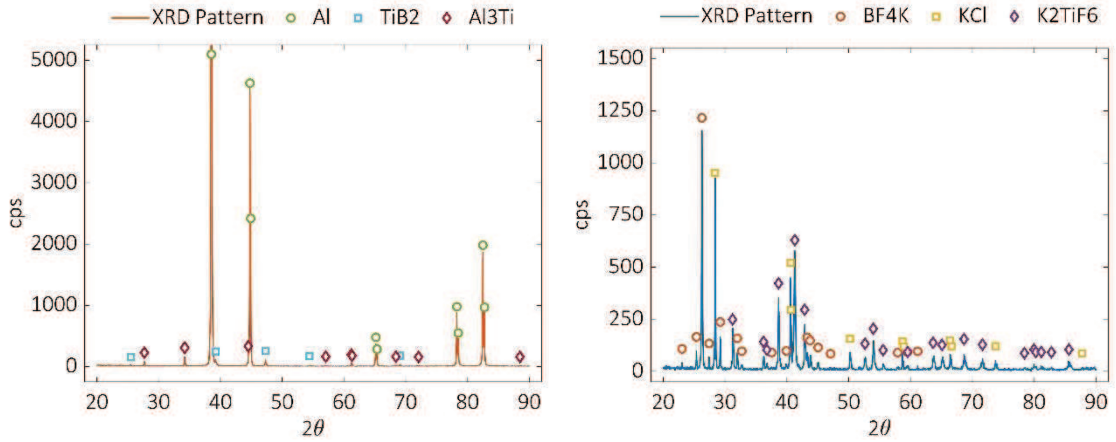

a) b)

Figure 2. 6 – XRD pattern of refiners: a) AlTi5B1 rod; b) commercial tab

Moldovan *et al.* [13] studied the thermodynamic interactions in the Al-K_2TiF_6-KBF_4 system and demonstrated that TiB_2 particles result from the aluminothermic reduction in Equation (2. 2):

$$3K_2TiF_6 + 6KBF_4 + 10Al \rightleftharpoons 3TiB_2 + 12KF + 10AlF_3 \tag{2. 2}$$

The reaction (2. 2) has a very high probability of development in the temperature interval of 750 ÷ 950 °C. The obtained TiB_2 particles are thermodynamically stable and very fine. Furthermore, the two potassium fluoride salts can singularly react with Al via reactions (2. 3) and (2. 4) that follow:

$$3K_2TiF_6 + 13Al \rightleftharpoons 3Al_3Ti + 6KF + 4AlF_3 \tag{2. 3}$$

$$6KBF_4 + 9Al \rightleftharpoons 3AlB_2 + 6KF + 6AlF_3 \tag{2. 4}$$

At a temperature higher than 700 °C, Al_3Ti and AlB_2 developed from reactions (2. 3) and (2. 4) can form TiB_2 particles via reaction:

$$3AlB_2 + 3Al_3Ti \rightleftharpoons 3TiB_2 + 12Al \tag{2. 5}$$

The authors also concluded that the presence of Si in the melt hinders the formation of Al_3Ti and AlB_2 via reactions (2. 3) and (2. 4), while it does not influence the first reaction (2. 2) that leads to TiB_2. According to Moldovan *et al.* [13], TiB_2 is the principal nucleating agent that forms *in situ* in the alloy with the addition of the refining tab.

Turning now to the thermal analysis of the alloys, Figure 2. 7 depicts the cooling curves related to different holding times after the refiner addition and Table 2. 4 reports the numerical values of the main thermal parameters.

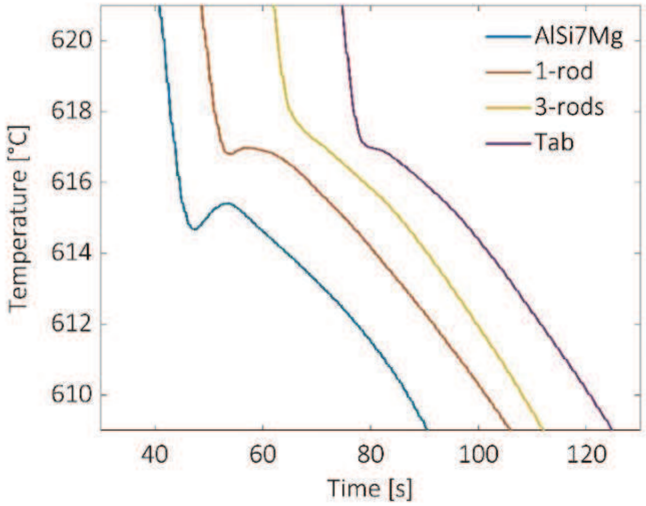

a)

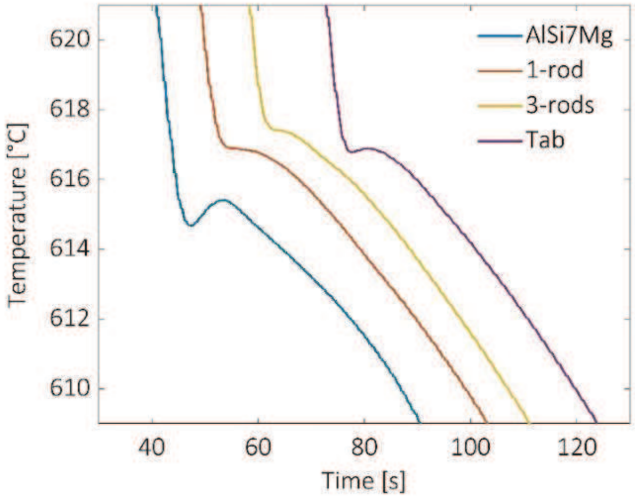

b)

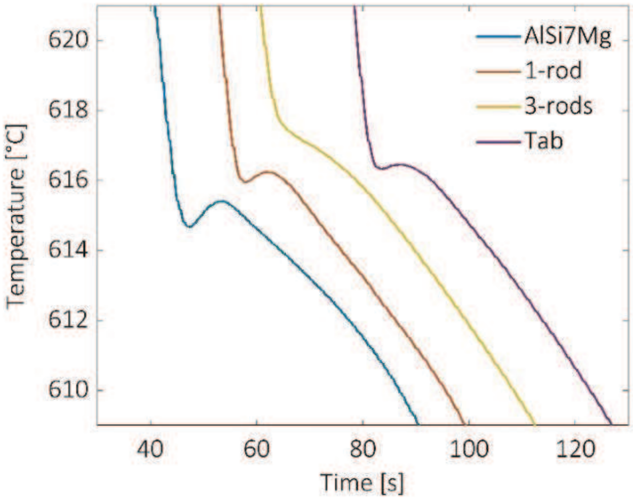

c)

Figure 2. 7 – Cooling curves of the investigated alloys at different holding times: a) 10 minutes; b) 60 minutes; c) 120 minutes

All the refiners determine an increase in T_M and T_G in comparison with the reference alloy after 10 minutes. In all cases reported in Table 2. 4, ΔT_R significantly decreases, and it reaches 0.0 °C for the 3-rods and tab alloys.

Table 2. 4 – Thermal parameters of the alloys at different holding times

Alloy	Holding time	T_M [°C]	T_G [°C]	ΔT_R [°C]
AlSi7Mg	-	614.7	615.4	0.7
1-rod	10 minutes	616.9	617.0	0.1
	60 minutes	616.9	616.9	0.0
	120 minutes	616.0	616.2	0.2
3-rods	10 minutes	617.2	617.2	0.0
	60 minutes	617.4	617.4	0.0
	120 minutes	617.1	617.1	0.0
Tab	10 minutes	617.0	617.0	0.0
	60 minutes	616.8	616.9	0.1
	120 minutes	616.4	616.5	0.1

On the other hand, one AlTi5B1 rod seems to be the less effective refiner in comparison with the other refiners, three AlTi5B1 rods and the tab, since the cooling curve still shows a slight recalescence. These findings are in line with the micrographs of Figure 2. 8, related to the unrefined alloy and the refined alloys after 10 minutes from the addition. The use of polarised light enables to distinguish the α-Al primary grains after electrolytic etching with Barker's reagent. The 3-rods (Figure 2. 8c) and the tab (Figure 2. 8d) alloys present a finer microstructure than the ones of AlSi7Mg and the 1-rod (Figure 2. 8b) alloy within 10 minutes from the addition of the refiner. After 60 minutes (Figure 2. 7b), both T_M and T_G maintain the same values for all the considered alloys and thus suggest that a fading phenomenon of the refining efficiency does not occur within the first hour after addition. Table 2. 4 highlights that there is only a slight increase in the ΔT_R value to 0.1 °C for the tab alloy, while the ΔT_R value of the 1-rod alloy decreases to 0.0 °C.

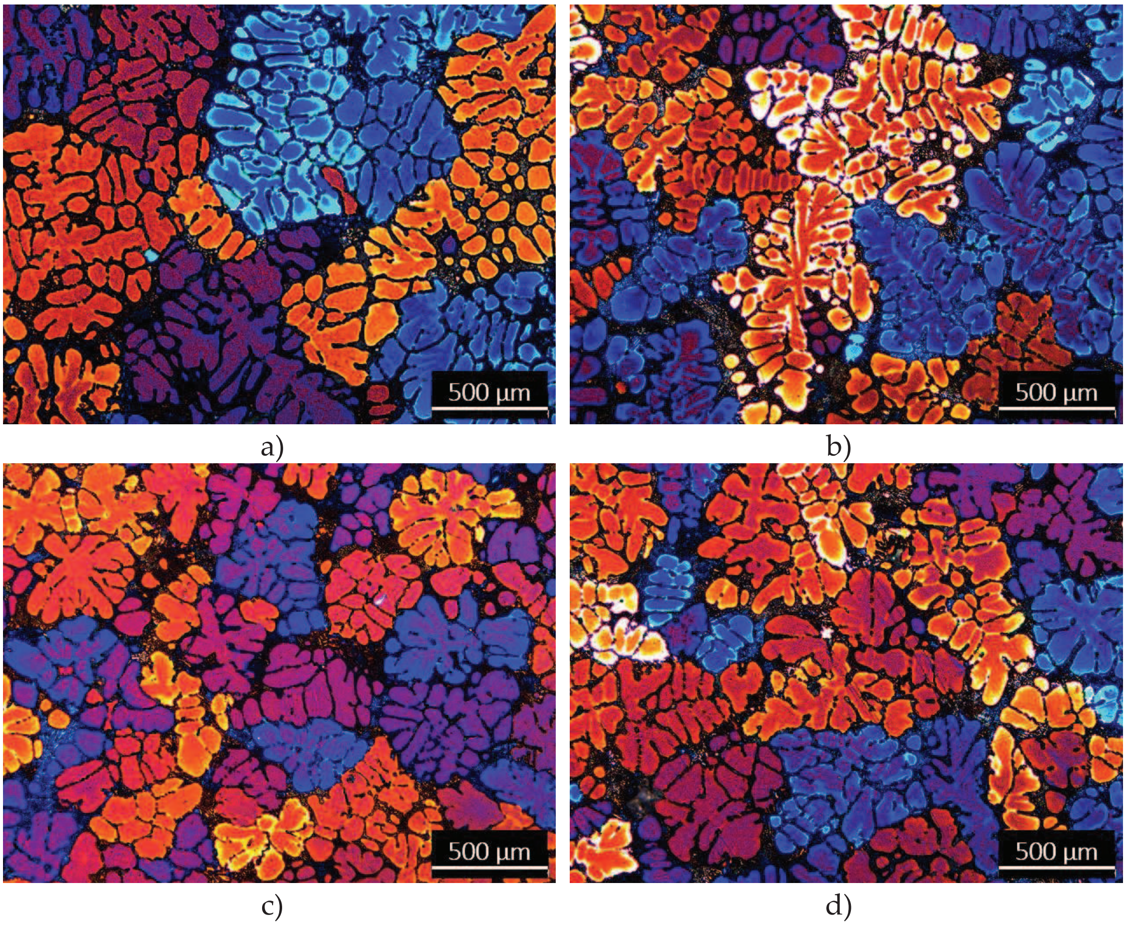

a) b)

c) d)

Figure 2. 8 – Micrographs after 10 minutes of the refiner addition: a) AlSi7Mg; b) 1-rod alloy; c) 3-rods alloy; d) tab alloy. OM with polarised light after electrolytic etching with Barker's reagent

Figure 2. 9 highlights that the 1-rod alloy has a grain structure with an AGS of 654 μm, refined in comparison with the reference alloy, with an AGS of 979 μm. The 3-rods and tab alloys show a significantly refined microstructure with 484 μm and 453 μm, respectively. The average grain size of the 1-rod alloy slightly decreases to 575 μm with the prolonged holding time of 60 minutes. A similar phenomenon can be observed for the 3-rods alloy since its AGS decreases from 484 μm to 464 μm, but the same does not occur for the tab alloy, that presents an AGS increase from 453 μm to 532 μm. This latter result mirrors the increase of the ΔT_R value to 0.1 °C. After 120 minutes (Table 2. 4) the

1-rod and tab alloys show a little recalescence of 0.2 °C and 0.1 °C, respectively, and these observations lead to the hypothesis that the refining effect begins to fade after such a prolonged holding time. T_M and T_G mirror the recalescence trend as they slightly decrease with increasing holding time. About the AGS, Figure 2. 9 reports that 1-rod alloy has a slight increase in the grain dimension, and the same occurs for the tab alloy. On the contrary, the 3-rods alloy shows an AGS practically constant even after the prolonged holding time of 120 minutes.

Figure 2. 9 also highlights that the addition of one AlTi5B1 rod shows its maximum efficiency after 60 minutes and remains almost constant until 120 minutes. This behaviour could suggest that 10 minutes are not sufficient to activate the refining process. The refining efficiency of three AlTi5B1 rods remains practically constant over the investigated time, and it is more significant than the one of the single refiner rod.

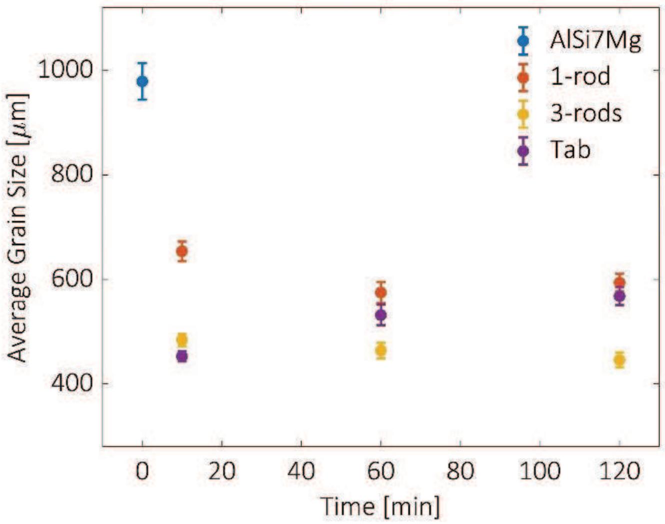

Figure 2. 9 – Average grain size vs. time

Conversely, the refiner tab presents a satisfactory refinement after 10 minutes from the addition, but then its beneficial effects fade with time and AGS increases after holding times of 60 minutes and 120 minutes. The presented results suggest that the thermal parameters reported in Table 2. 4 are a trustworthy indicator of the refining process since the ΔT_R value of 0.0 °C corresponds to the minimum AGS value reached with each refiner.

It is fundamental to keep in mind that the refining condition is not the only parameter that governs the final AGS. Cooling speed is the other variable that determines the dimension of SDAS and primary α-Al grains. The higher the cooling rate, the lower the SDAS value according to the relationship in Equation (2. 6):

$$CR = 2 \cdot 10^{4} \cdot SDAS^{-2.67} \tag{2. 6}$$

where $CR\ [°C/s]$ is the cooling rate. Several works in the literature indicate the relationship of Equation (2. 6) to be valid for cast Al alloys [14]–[18]. Figure 2. 10 depicts the micrographs of alloys in the same refining conditions (*i.e.* no refinement, 1-rod and 3-rods) but solidified with different cooling speeds that led to 20 µm and 65 µm of SDAS. The cooling rate has a significant influence on the resulting grain size: the alloys with a SDAS value of 20 µm present an AGS that goes from ~ 260 to ~ 380 µm; the AGS falls within the 435 ÷ 720 µm range for the alloys with a SDAS values of 65 µm.

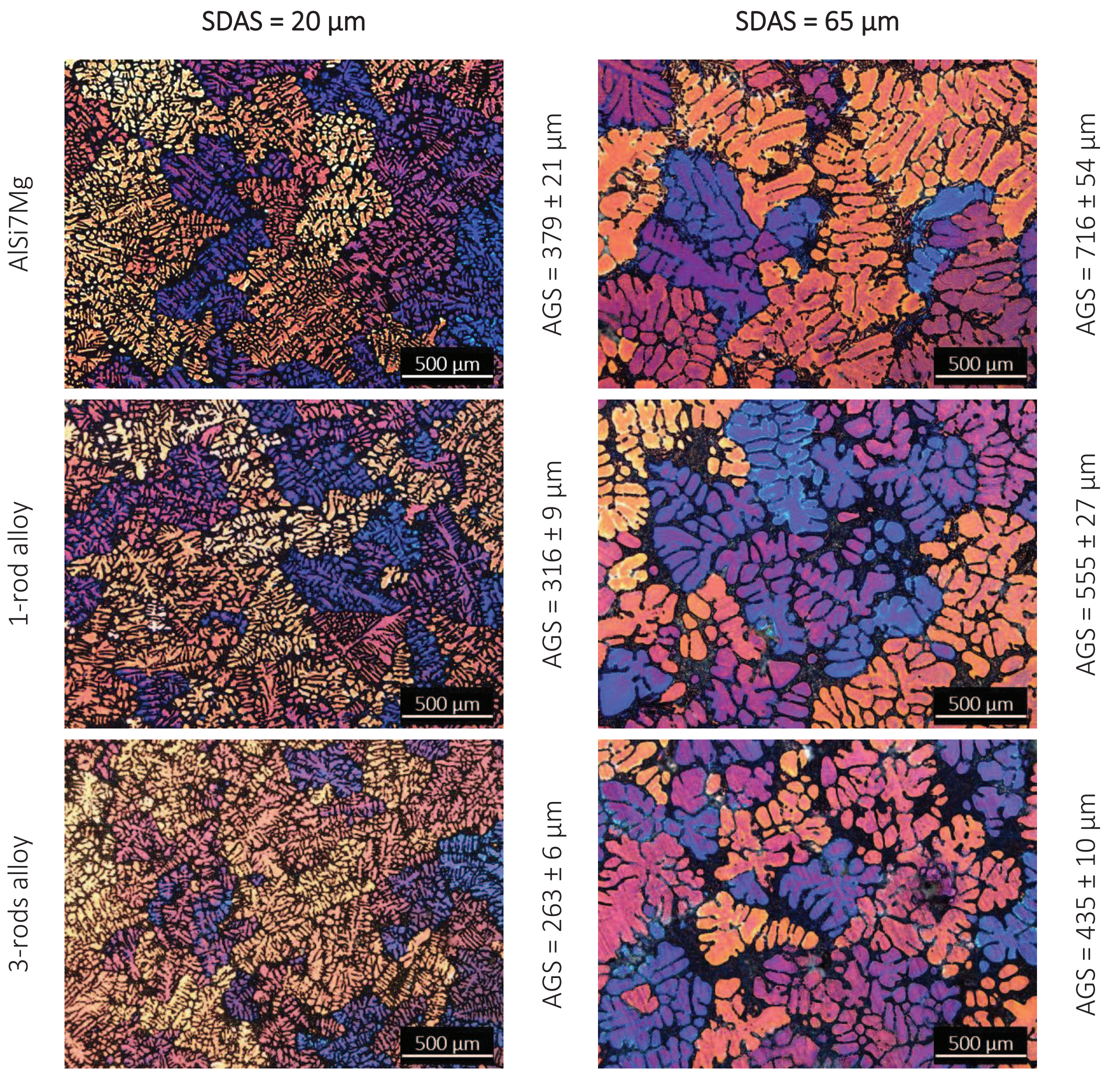

Figure 2. 10 – Comparison of the AVG that results from the same grain refining conditions and different cooling rates

The cooling rate that leads to 20 µm of SDAS covers the effect of the grain refiners and limits the width of the AGS range. On the other hand, a cooling rate related to a SDAS value of 65 µm sheds light on the effect of different quantities of grain refiners.

The AGS range in the latter case widens, and a difference of ~ 285 μm separate the grain dimension of the unrefined alloy from the on of the 3-rods alloy. The presented results highlight that a refining condition is not related to a specific value of AGS, as the cooling rate also determines the latter. Thus, thermal analysis parameters can either confirm or not the success of grain refinement but do not give a specific value of grain size.

The present study sets out to investigate how holding time could influence the refining efficiency of different grain refiners. The following concluding remarks arise from the combination of the cooling curves with microstructural investigations:

- The AlTi5B1 rods enable to reach a quality level of grain refinement, with the average grain size ranging from ~ 460 μm (3 rods/100 kg) to ~ 575 μm (1 rod/100 kg) after 60 minutes of holding time. Their effect requires a minimum activation time, but it seems to remain constant for prolonged times up to 120 minutes of holding. This phenomenon occurs for both the investigated quantities.
- The refiner tab determines after 10 minutes a level of grain refinement (AGS ~ 450 μm) comparable with the best one obtained by the addition of AlTi5B1 rods (AGS ~ 460 μm). Nevertheless, after 60 and 120 minutes, the average grain size increases with the ΔT_R value, indicating that the beneficial effects of the refiner tab suffer a fading phenomenon.

2.3.2 Interaction of alloying and trace elements with Sr

2.3.2.1 Interaction with alloying elements

Figure 2. 11 depicts the eutectic cooling curves of the AlSi7 alloys with different alloying elements in order to investigate their influence on the presence of Sr, and Table 2. 5 reports the thermal parameters of the unmodified alloys. Figure 2. 11a concerns the binary AlSi7 alloys and appears clear the role of Sr in lowering the minimum and growth eutectic temperatures. The minimum temperature decreases from ~ 577 °C to 571 °C with the addition of 40 ppm of Sr, and it remains stable as the Sr content increases up to 140 ppm. The growth temperature does not follow the same trend, as it presents a limited decrease with 40 ppm of Sr and further decreases with 70 ppm of Sr. As a consequence, the ΔT_R increases up to 4.4 °C for 70 ppm of Sr, and it stabilises at ~ 3.3 °C for Sr contents of 100 and 140 ppm. Similar observations come from Figure 2. 11b, related to the AlSi7+Ti alloy. The minimum temperature decreases significantly from 577 °C to 571 °C with the

addition of 40 ppm of Sr, and it remains stable as the Sr content increases up to 140 ppm. On the other hand, T_G has a gradual and continuous decrease with the increasing content of Sr up to 100 ppm and stabilises at ~ 574 °C for 140 ppm of Sr.

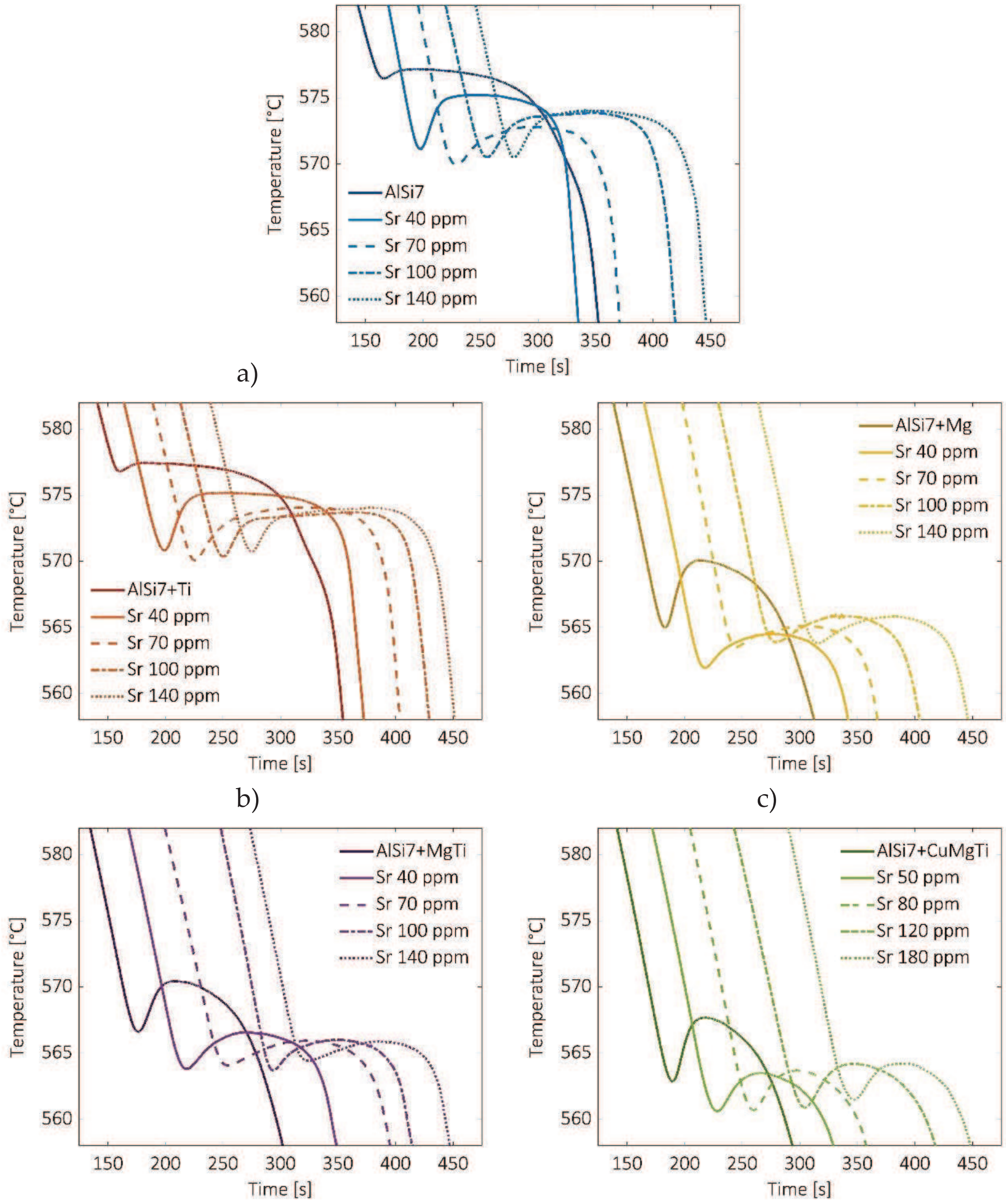

a)

b)

c)

d)

e)

Figure 2. 11 – Thermal analysis of the Sr-alloying elements interaction alloys: a) AlSi7; b) AlSi7 + Ti; c) AlSi7 + Mg; d) AlSi7 + MgTi; e) AlSi7 + CuMgTi

The cooling curves of the alloys that contain Mg present a different eutectic solidification region, shortened in duration and shifted to lower temperatures than the AlSi7 and AlSi7+Ti alloys. The presence of Mg in the alloy determines the minimum temperature of ~ 565 °C and the growth temperature of ~ 570 °C for the unmodified alloy. The addition of 40 ppm of Sr determines a decrease of T_M to ~ 562 °C, and it slowly increases up to ~ 564 °C with further additions of Sr up to 140 ppm. The ΔT_G values present a maximum for 40 ppm of Sr, and it decreases as the Sr content increases.

Table 2. 5 – Sr-alloying elements interaction: thermal parameters of the alloys

Alloy	Sr [ppm]	T_N [°C]	T_M [°C]	T_G [°C]	ΔT_R [°C]	ΔT_G [°C]
AlSi7	-	577.1	576.6	577.2	0.6	-
	40	571.6	571.2	575.2	4.0	2.0
	70	570.5	570.0	572.8	2.8	4.4
	100	571.1	570.6	573.9	3.3	3.3
	140	570.5	570.4	573.8	3.4	3.4
AlSi7 + Ti	-	577.5	576.9	577.4	0.5	-
	40	571.2	571.2	575.6	4.4	1.8
	70	571.2	570.9	575.0	4.1	2.4
	100	571.5	571.3	574.6	3.3	2.8
	140	572.1	571.9	575.0	3.1	2.4
AlSi7 + Mg	-	565.2	565.1	570.1	5.0	-
	40	562.6	562.1	564.5	2.4	5.6
	70	564.7	563.7	565.1	1.4	5.0
	100	565.2	564.0	566.0	2.0	4.1
	140	565.2	563.9	565.8	1.9	4.3
AlSi7 + MgTi	-	567.0	566.7	570.4	3.7	-
	40	564.4	563.9	566.6	2.7	3.8
	70	564.6	564.2	565.9	1.7	4.5
	100	564.4	563.8	566.0	2.2	4.4
	140	565.8	564.5	565.9	1.4	4.5
AlSi7 + CuMgTi	-	563.0	562.9	568.0	4.8	-
	40	561.0	560.7	563.5	2.8	4.5
	70	561.0	560.8	563.7	2.9	4.3
	100	561.0	561.0	564.2	3.2	3.8
	140	561.0	561.6	564.2	2.6	3.8

The unmodified AlSi7+MgTi alloy shows thermal parameters comparable with the ones of the unmodified AlSi7+Mg alloy. The addition of Sr leads to a gradual decrease in the T_G up to 70 ppm, and it stabilises at ~ 566 °C for further additions. The ΔT_G values present a comparable trend, as increase to ~ 4.5 °C and remain stable. The Cu-containing alloys behave like the ternary alloys with Mg since the ΔT_G values have a maximum with 40 ppm of Sr and then decrease as the Sr content increases. The presence of Cu lowers the cooling curves in comparison with the other alloys, as reported in the literature [19]–[23].

Figure 2. 12 depicts the representative micrographs of the alloys.

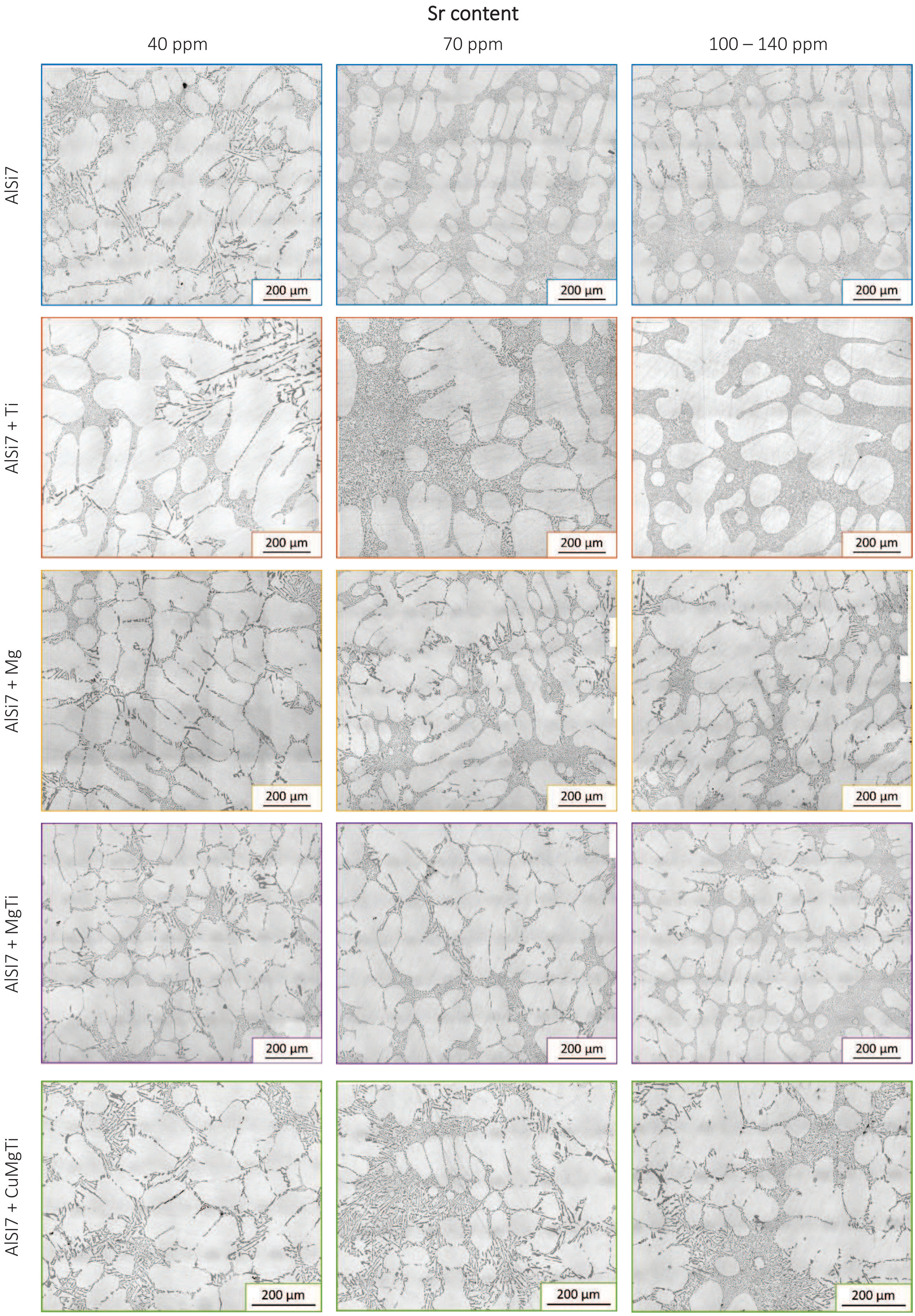

Figure 2. 12 – Sr-alloying elements interaction: micrographs of the alloys

From OM investigations results that 40 ppm is not a content of Sr able to promote the flake-fibre transition in the alloys, because acicular Si particles are present in all cases. The increase to 70 ppm of Sr is enough to entirely modify the eutectic Si particles in the AlSi7 and AlSi7+Ti alloys. Further additions of Sr up to 100 and 140 ppm of Sr do not have a significant modifying effect on the eutectic particles. Similar observations do not hold for the Mg-added alloys, in which lamellar Si particles still occur at 70 ppm of Sr. These lamellar particles are present also with higher Sr contents in the alloys that contain Mg, even if with a lower frequency than before.

Image analysis is often a useful tool to quantify the qualitative observations that come from OM. It is a technique that enabled to measure several geometrical properties of Si particles, such as area, perimeter and equivalent diameter. Specific combinations of these geometrical properties lead to tailored parameters that are sensitive to particular shape changes and highlight significant trends [24]. For the present investigation, equivalent diameter (ED) and circularity (C) are considered valid instruments to characterise eutectic Si particles. The former is related to the size of the particle and the latter to its morphology. The well-modified Si particles should present a circularity value close to 1 (the perfect circle) and a small value of equivalent diameter. To enhance their effectiveness, they are combined in Equation (2. 7):

$$ED^* = ED/\sqrt{C}\ [\mu m] \tag{2. 7}$$

Equivalent diameter does not consider the morphology of the particles and cannot distinguish lath particles from round ones; circularity, on the other hand, does not deliver information about the dimension of the particles. In the case modification of eutectic Si, it is crucial to describe well both dimension and morphology of particles, and the modified equivalent diameter ED* satisfies this need. Given two particles with the same area and thus same ED, the one that presents the more irregular shape has a higher value of ED* than the one that appears circular.

The image analysis tailored code in Matlab ® accepts as modified the eutectic Si particles that present $ED^* < 10\,\mu m$, while discards the one with $ED^* > 10\,\mu m$. The threshold value of 10 μm comes from a series of preliminary analyses on specific micrographs with unmodified and fully modified Si particles. The variation of the limits for area and circularity in the image analysis software and the ED* calculation for a wide variety of particles shape led to the determination of the threshold. Figure 2. 13 summarises the steps of image analysis that gives the ED* values of a typical micrograph. The micrograph of interest (Figure 2. 13a) is binarised (Figure 2. 13b) for the image analysis software, and the ED* = 10 μm value highlights the discarded particles (Figure 2. 13c).

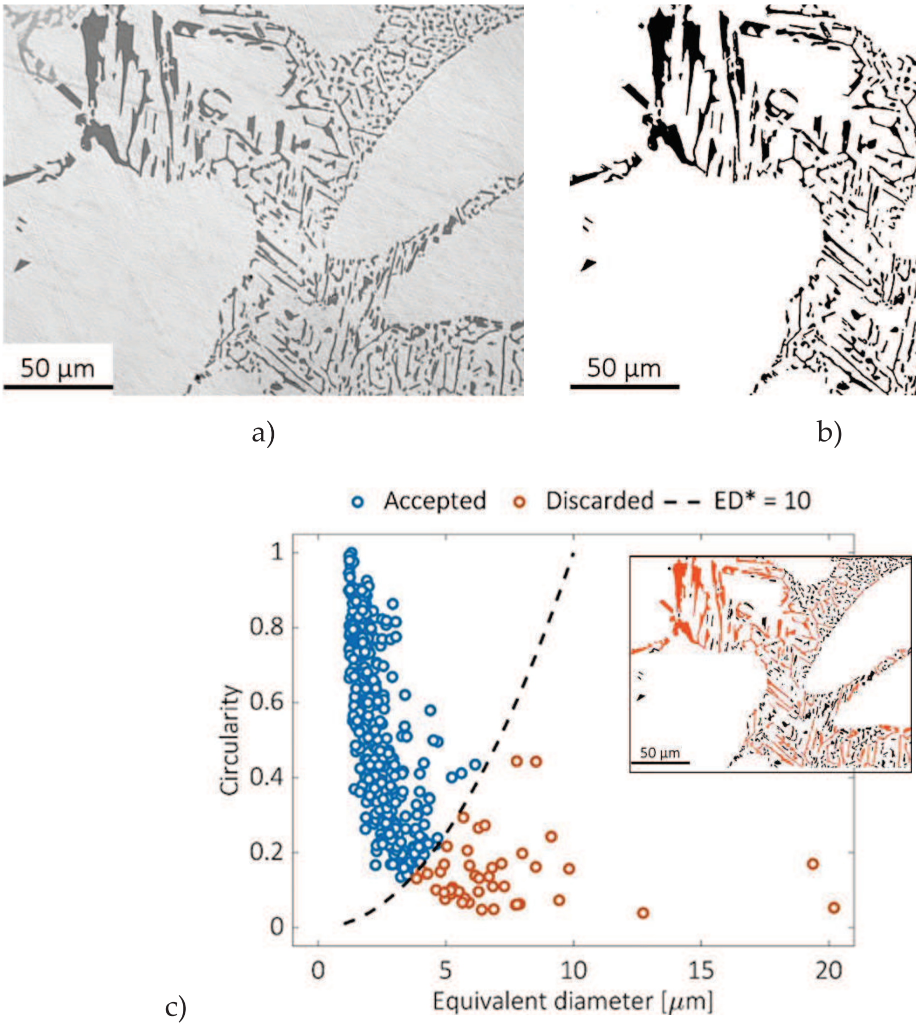

a)

b)

c)

Figure 2. 13 – Steps of image analysis: a) original micrograph; b) binary image for image analysis; c) determination of ED* = 10 μm as the threshold value

Over the years, several authors proposed various combinations of geometrical parameters in order to find the most suitable that detects modified Si particles and assess modification [25]–[27]. The present study proposes a parameter that enables to combine both morphology and dimension of the particles with the total investigated area.

The parameter W considers the area fraction of discarded particles and their ED* parameter, as follows in Equation (2. 8) :

$$W = \frac{\sum \frac{(ED_D)^2}{A_t}}{\sum \frac{(ED_A)^2}{A_t} + \sum \frac{(ED_D)^2}{A_t}} \cdot \frac{\sum (ED_D^*)^2}{\sum (ED_D^*)} \; [\mu m] \tag{2. 8}$$

where the subscript "A" stays for accepted and the subscript "D" means discarded. A_t $[\mu m^2]$ is the total investigated area of the micrographs. The first factor corresponds to the area fraction of the discarded particles over the area fraction of the Si particles, both accepted and discarded. It is essential to consider a dimensional fraction of the particles because equivalent diameter and circularity can compensate. The second factor is the weighted average of ED* of discarded particles with itself as the weighting function. In this way, the weighting function of the second term amplifies its sensitivity to the morphology of discarded particles compared to the arithmetic average.

Figure 2. 14 depicts the results of the tailored image analysis for the investigated alloys. The unmodified alloys present comparable values of W, with mean values comprised between 40 and 60. In fact, in unmodified microstructures, a considerable number of particles is discarded because of their flake morphology and significant size. The presence of 40 ppm of Sr decreases uniformly the mean W values of the alloys, comprised in the 20 ÷ 40 µm range. 40 ppm is a limited amount of Sr, not enough to determine the full flake-fibre transition in the alloys. Distinctly different behaviours occur with further additions of Sr, from 70 to 140 ppm.

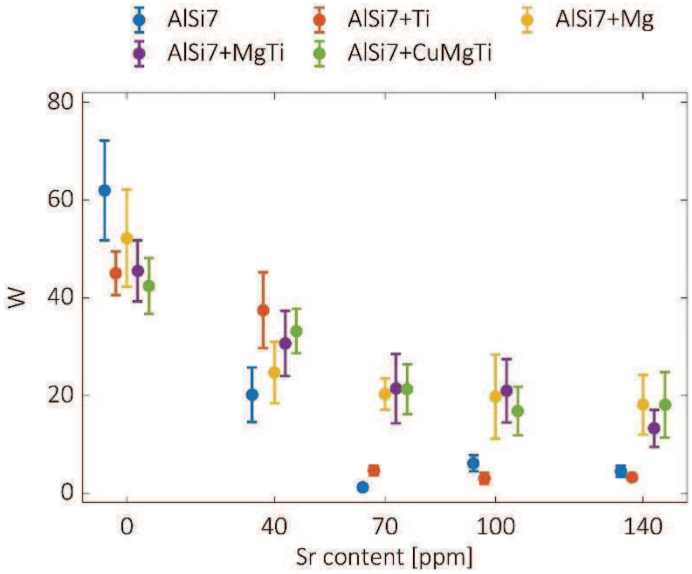

Figure 2. 14 – Sr-alloying elements interaction: image analysis results

The binary and the Ti-added alloys present significantly lower values than the Mg-added alloy, and this result mirrors the OM observations. The addition of 70 ppm of Sr results in a well-modified microstructure in the AlSi7 and AlSi7+Ti alloys, and it remains stable when the Sr content raises to 140 ppm. Different observations concern the alloys that contain Mg. The increasing content of Sr up to 140 ppm leads to a slightly decreasing trend of the W values, as depicted in Figure 2. 14. This behaviour corresponds to coarser eutectic structures than the ones in AlSi7 and AlSi7+Ti alloys, and it agrees with the observations reported by Heiberg *et al.* [28]. It is reasonable to hypothesise that lower values of W would result from higher Sr content that the ones investigated. In fact, in foundry practice, Sr content higher than 150 ÷ 200 ppm are usually employed to modify the AlSi7Mg alloys. These contents permit to overcome the negative influence of alloying elements on Sr modification.

Some authors investigated the influence of some alloying elements on the nucleation and the morphology of Al-Si eutectic and AlSi7 [23], [28], [29] and AlSi10 alloys [21], [30]. Heiberg *et al.* [29] report that the eutectic solidification front in the binary AlSi7 alloy planar and regular, independently of the Sr level. In the commercial AlSi7Mg0.3 alloy, on the other hand, the eutectic reaction is no longer isothermal, and solidification occurs through a eutectic mushy zone. The eutectic Si appears well-modified in the binary alloy with 150 ppm of Sr while it presents coarse particles in the AlSi7Mg alloy with 100 ppm of Sr. These results correspond to what observed in the present work, comparing the binary alloy and the AlSi7+MgTi alloy: the eutectic particles are finer in the former alloy than the ones in the latter. Moreover, the Mg-added alloys present high values of recalescence that can correspond to the formation of the eutectic mushy zone. The binary and Ti-added AlSi7 alloys, on the other hand, both have a limited recalescence with a flat and regular eutectic temperature profile (Figure 2. 11). Later studies by Heiberg *et al.* [23], [28] face the addition of Cu (0.7 ÷ 3 wt.%) and Mg (1 wt.%) to Sr-modified AlSi7 alloys. The micrographs show a coarsening of the eutectic microstructure as the Cu content increases, regardless of the Sr content, and the eutectic inter-flake spacing increases 2 μm to 7 μm. A similar result comes from the comparison of the AlSi7 and the AlSi7+CuMgTi alloys of the present study since in the latter the eutectic Si particles present a coarse morphology despite the Sr additions.

Darlapudi *et al.* [21], [30] further investigate the influence of Cu (1 ÷ 6 wt.%) and Mg (0.5 ÷ 2.5 wt.%) additions on the eutectic morphology of AlSi10 alloys. The studies focused on both eutectic nucleation and growth dynamics. For what concerns nucleation, the segregation of Cu in unmodified alloys has a limited effect on the already high nucleation density of eutectic cells. On the other hand, since Sr poisons the density and the potency of available nuclei, the presence of Cu leads to a constitutional supercooling ahead of the solidification front. This phenomenon limits the nucleation-free zone around the growing grains and promotes eutectic nucleation. Thus, the number of eutectic grains increases as the Cu content increases [21]. The presence of Mg determines a similar effect, as it increases the nucleation density of eutectic grains [30].

In summary, both Cu and Mg have an influence on eutectic nucleation that is opposite to the Sr one, that decreases the number of active eutectic nuclei. The nucleation density, in turn, determines the growth velocity of eutectic Si and its morphology. Few nucleating grains are associated with a high eutectic growth velocity and vice versa. The authors report that an average eutectic interface velocity higher than 16 μm/s leads to completely fibrous Si particles and is mostly related to Sr-modified alloys. In unmodified alloys, the average interface velocity is lower than 4 μm/s, and it is associated with a flake-like eutectic Si.

The presented literature highlights that the alloying elements have a two-fold effect on the eutectic morphology. The constitutional undercooling, caused by the presence of alloying elements, plays a fundamental role during the eutectic solidification and determines the resulting morphology of Si particles. Besides, Sr does not affect the morphology of the solid/liquid interface but influences only its velocity.

In conclusion, Mg and Cu both increase the density of eutectic grains and, for this reason, the eutectic Si particles result coarser than the AlSi7 and AlSi7+Ti alloys at the same Sr content. The Ti content typically present in the AlSi7Mg systems does not determine ternary eutectic precipitation, unlike Cu and Mg. The invariant Al-Si eutectic transformation remains the last solidification event in the AlSi7+Ti system. Thus Ti does not interfere with Sr modification mechanisms, and the morphology of Si particles is analogous to the one typical of the binary AlSi7 alloy.

The addition of Sr has a different effect on the eutectic recalescence of Mg-free and Mg-added alloys. Figure 2. 11a-b illustrate that 40 ppm of Sr significantly increase the ΔT_R values in comparison to the unmodified alloys. Further increases of Sr reduce and stabilise the recalescence magnitude at ~ 4 °C (Table 2. 5). Conversely, as depicted in Figure 2. 11c-e, Sr determines a lower recalescence value than the unmodified alloys that contain Mg. The decrease of ΔTR in the Mg-containing alloys can be related to the fact that Sr hinders nucleation and thus increases the eutectic interface velocity. The initial addition of 40 ppm is enough to reduce the ΔTR value, and it stabilises as Sr increases. An analogous explanation holds for the AlSi7 and AlSi7+Ti alloys with Sr contents higher than 70 ppm because recalescence has a decreasing trend. The significant recalescence related to the 40 ppm of Sr in the Mg-free alloys is a phenomenon not yet clarified, and it needs further investigation.

2.3.2.2 Interaction with trace element

Figure 2. 15 represents the effect of Ca additions on the cooling curve of AlSi7Mg alloys. The modification of an AlSi7Mg alloy with 180 ppm of Sr leads to a significant decrease of both minimum and growth temperature, together with ΔTR.

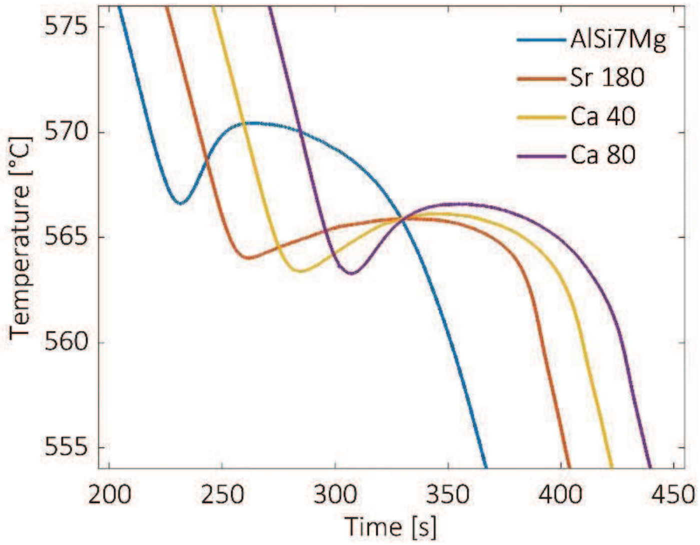

Figure 2. 15 – Sr-Ca interaction: cooling curves of the alloys

The thermal parameters of Table 2. 6 highlight that eutectic nucleation temperature decreases continuously with the addition of trace elements, firstly Sr and secondly Ca. This effect is due to the hindering of eutectic nucleation, that corresponds to increased eutectic interface velocity. The recalescence value slightly increases from 1.8 to 3.2 °C as the content of Ca increases to 40 and 80 ppm. The minimum temperature raises and stabilises at 563.4 °C when Ca is present in the alloy. TG slightly increases to ~ 566 °C and 566.6 °C with the 40 and 80 ppm additions, respectively. On the other hand, ΔTG values decrease as the Ca content raises in the alloys, and this phenomenon can highlight that eutectic interface velocity decreases slightly.

Table 2. 6 – Sr-Ca interaction: thermal parameters of the Ca-added alloys

Alloy	T_N [°C]	T_M [°C]	T_G [°C]	ΔT_R [°C]	ΔT_G [°C]
AlSi7Mg	567.0	566.7	570.4	3.7	-
Sr 180	564.8	564.1	565.9	1.8	4.5
Ca 40	564.4	563.4	566.1	2.7	4.3
Ca 80	564.0	563.4	566.6	3.2	3.8

Micrographs in Figure 2. 16 enable to compare the microstructure of the different alloys. The unmodified AlSi7Mg alloy (Figure 2. 16a) presents the typical eutectic Si flakes, which appear fully modified and fibrous in the Sr 180 alloy (Figure 2. 16b). The presence of 40 ppm of Ca slightly interferes with the Sr modification and some regions present flake-like Si particles despite the 180 ppm of Sr added to the melt (Figure 2. 16c). Figure 2. 16d represents the deleterious effect of 80 ppm of Ca on the Sr modification, that leads to an increased number of flake Si particles.

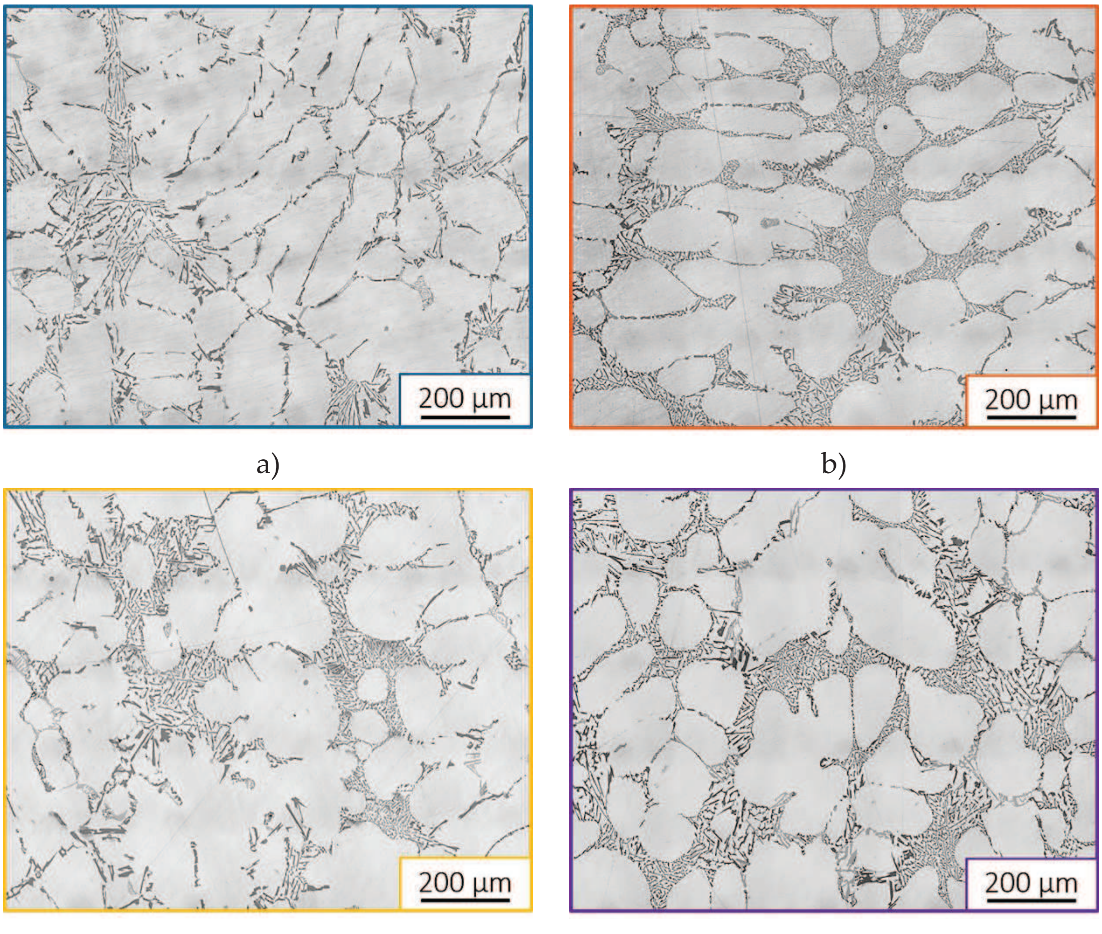

a) b)

c) d)

Figure 2. 16 – Sr-Ca interaction: micrographs of the alloys. a) AlSi7Mg; b) Sr 180; c) Ca 40; d) Ca 80

Once again, image analysis helps to quantify the qualitative observations that come from micrographs through the W parameter reported in Equation (2. 8), and Figure 2.

17 summarises the results. As expected, the Sr 180 alloy presents a W value lower than the unmodified alloy. The presence of Ca slightly affects the morphology of eutectic Si particles in some regions, as the W values increase with increasing Ca contents. This behaviour corresponds to what qualitatively observed by OM investigations.

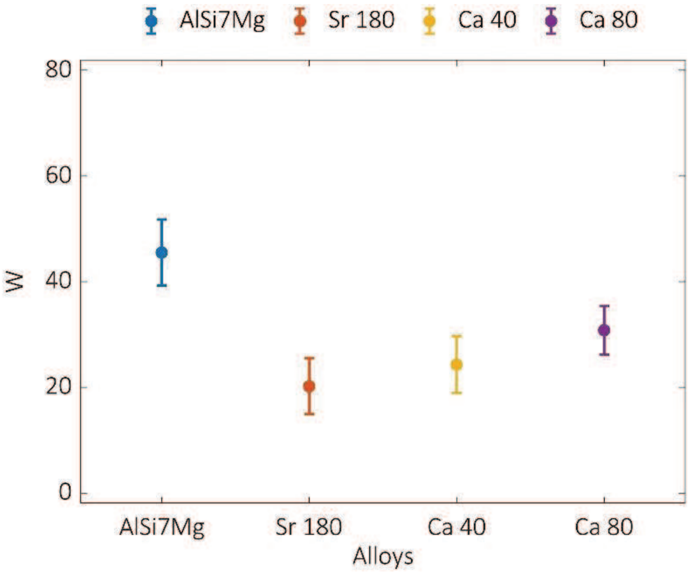

Figure 2. 17 – Sr-Ca interaction: image analysis results

The presented results about eutectic morphology agree with some studies that investigated the detrimental effect of Ca on the Sr modification [9], [31]–[33]. El-Hadad *et al.* [31] report that 20 ppm of Ca affect the modification efficacy of Sr in an AlSi7Cu3 alloy. Ca promotes the formation of $Al_x(Ca,Sr)Si_x$ compounds. Such compounds present a blocky morphology in Mg-containing alloys and nucleate either on AlP or oxide particles before the eutectic nucleation. Rakhmonov *et al.* [9] also observed that $Al_2(Ca,Sr)Si_2$ deactivates AlP particles as nucleation sites for the Al-Si eutectic. For this reason, the resulting thermal analysis presents low eutectic temperatures. Samuel *et al.* [32] presented similar results for AlSi7Cu3 alloys containing Mg, observing that 100 ppm of Ca hinder the modifying effect of 180 ppm of Sr.

SEM investigations coupled with EDS measurements enabled to detect $Al_x(Ca,Sr)Si_x$ compounds in the alloys considered in the present study. Figure 2. 18a depicts the SEM micrographs of polygonal intermetallic compounds that contain Sr and a minimum amount of Ca, according to the related EDS spectra in Figure 2. 18b. Data do not suggest the $Al_x(Sr,Ca)Si_x$ stoichiometry, because of the high content of Sr. Nevertheless, the precipitation of such intermetallic particles confirm that Ca combines with Sr before the eutectic solidification, and both do not longer act as modifiers. The eutectic particles in the area around appear with the flake morphology typical of unmodified alloys.

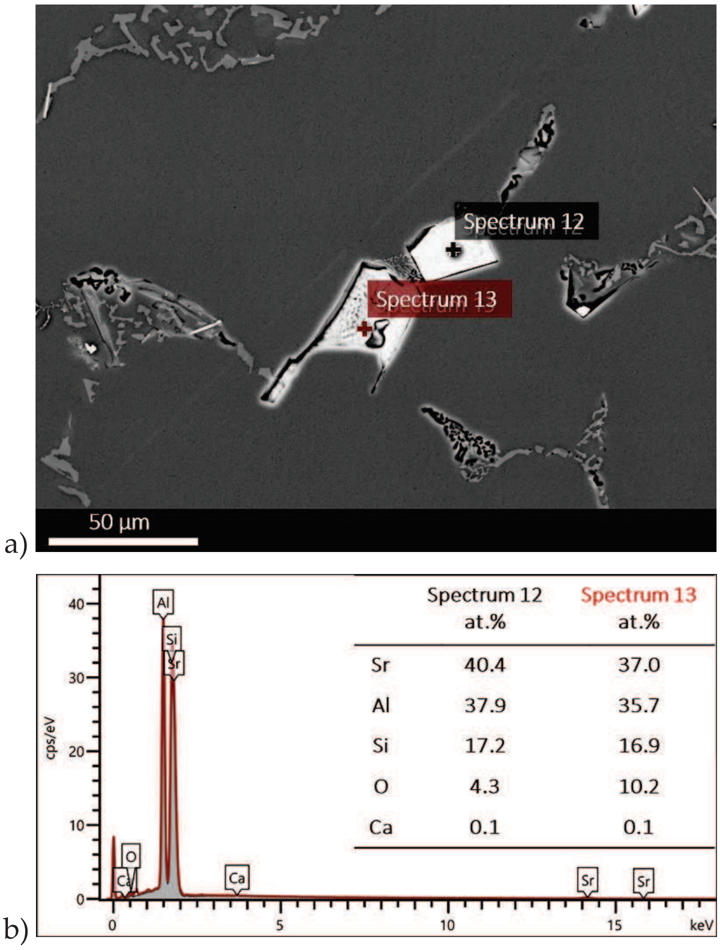

	Spectrum 12 at.%	Spectrum 13 at.%
Sr	40.4	37.0
Al	37.9	35.7
Si	17.2	16.9
O	4.3	10.2
Ca	0.1	0.1

Figure 2. 18 – Al$_x$(Ca,Sr)Si$_x$ intermetallic compounds: a) SEM micrograph and b) related EDS spectra

Figure 2. 19a reports an SEM image of a blocky intermetallic compound that contains both Ca and Sr. The related EDS spectra in Figure 2. 19b highlight that these compounds nucleate on P-based particles (spectrum 97), according to the literature [34], [35]. Eutectic nucleation sites result poisoned, the eutectic temperatures are low, and given the presence of Sr one would expect well-refined eutectic Si particles because the solid/liquid interface moves faster [36]. However, the resulting microstructure is the opposite. The consequence of the precipitation of Al$_x$(Ca,Sr)Si$_x$ compounds is that Sr is no longer available to either poison the TPRE growth of eutectic Si or lower the minimum growth velocity to obtain the complete flake-to-fibre transition [36]. Neither Ca in such small quantities is free to act as a eutectic modifier because wholly involved in the precipitation of pre-eutectic intermetallic compounds. This phenomenon results in a microstructure that appears less modified than the one of Ca free alloys.

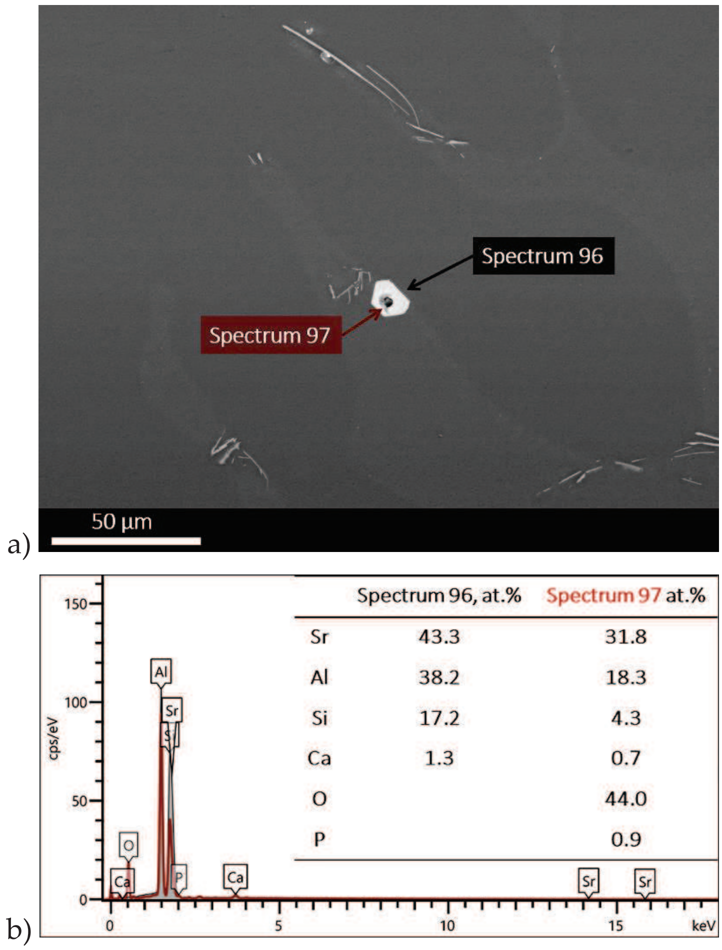

	Spectrum 96, at.%	Spectrum 97 at.%
Sr	43.3	31.8
Al	38.2	18.3
Si	17.2	4.3
Ca	1.3	0.7
O		44.0
P		0.9

Figure 2. 19 – Nucleation of an $Al_x(Sr,Ca)Si_x$ compound on a P-based particle: a) SEM micrograph and b) related EDS spectra

In conclusion, the presence of limited amounts of Ca, less than 100 ppm, should be carefully avoided or at least not underestimated in Sr-modified AlSi7Mg alloys. Even 40 ppm of Ca influence the precipitation of intermetallic compounds that reduce both the number of eutectic nuclei and the amount of Sr available to act as a modifier for Si particles. As a result, eutectic modification is hindered and the final microstructure does not match the expectations.

2.4 CONCLUSION

The present research aimed to clarify whether or not thermal analysis can be a helpful tool to predict the melt quality in the everyday routine of Al foundries. The following concluding remarks emerge from the studies about grain refining and eutectic modification:

- The efficacy of either different grain refiners or different additions of the same one corresponds to precise thermal analysis outcomes. Changes of specific thermal characteristics mirror different grain dimensions, but they cannot be directly related to a numerical value of the grain size. Thus the only limit is the cooling speed, the parameter that determines the final grain size in the cast component. Nevertheless, thermal analysis results in a performing instrument that can substitute microstructural analysis to assess grain refining.

- Conversely, thermal analysis is not suitable to assess eutectic modification, especially when various alloying or trace elements are also present. The operator that is not aware of either the chemical composition of the alloy or the influence that each element of the alloy has on solidification can draw misleading conclusions from thermal analysis results. Thus the observations related to the cooling curves have to be supported by OM micrographs to assess eutectic modification with a good grade of confidence.

REFERENCES

[1] D. Apelian, G. K. Sigworth, and K. R. Whaler, *Assessment of grain refinement and modification of Al-Si foundry alloys by thermal analysis*, AFS Trans., vol. **92**, no. 161, pp. 297–307, 1984

[2] A. A. Canales, J. Talamantes-silva, D. Gloria, S. Valtierra, and R. Colás, *Thermal analysis during solidification of cast Al-Si alloys*, Thermochim. Acta, vol. **510**, pp. 82–87, 2010

[3] V. Utiérrez, G. González, and A. García, *Thermal analysis of grain refinement and modification of an A356 cast alloy*, Chem. Mater. Res., vol. **6**, no. 6, pp. 52–63, 2014

[4] S. Argyropoulos, B. Closset, J. E. Gruzleski, and H. Oger, *The quantitative control of modification in Al-Si foundry alloys using a thermal analysis technique*, AFS Trans., vol. **91**, pp. 351–358, 1983

[5] V. A. Hosseini and S. G. Shabestari, *Study on the eutectic and post-eutectic reactions in LM13 aluminum alloy using cooling curve thermal analysis technique*, J. Therm. Anal. Calorim., vol. **124**, no. 2, pp. 611–617, 2016

[6] M. S. Abdelrahman, M. T. Abdu, and W. Khalifa, *Assessment of eutectic modification level in Al-Si alloys via thermal analysis*, in *Light Metals 2017*, 2017, pp. 885–895

[7] B. Golbahar, E. Samuel, A. M. Samuel, H. W. Doty, and F. H. Samuel, *On thermal analysis, macrostructure and microstructure of grain refined al–si–mg cast alloys: Role of sr addition*, Int. J. Cast Met. Res., vol. **27**, no. 5, pp. 257–266, 2014

[8] L. Heusler and W. Schneider, *Influence of alloying elements on the thermal analysis results of Al-Si cast alloys*, J. Light Met., vol. **2**, no. 1, pp. 17–26, 2002

[9] J. Rakhmonov, G. Timelli, and G. Basso, *Interaction of Ca, P trace elements and Sr modification in AlSi5Cu1Mg alloys*, J. Therm. Anal. Calorim., vol. **133**, pp. 123–133, 2018

[10] S. Nafisi and R. Ghomashchi, *Semi-solid processing of aluminum alloys*, 2016th ed. Berlin, Germany: Springer, 2016

[11] S. Nafisi and R. Ghomashchi, *Effects of modification during conventional and semi-solid metal processing of A356 Al-Si alloy*, Mater. Sci. Eng. A, vol. **415**, no. 1–2, pp. 273–285, 2006

[12] B. Closset, H. Dugas, M. Pekguleryuz, and J. E. Gruzleski, *The aluminum-strontium phase diagram*, Metall. Trans. A, vol. **17**, no. 7, pp. 1250–1253, 1986

[13] P. Moldovan *et al.*, *Thermodynamics of interactions in Al-K2TiF6-KBF 4 system*, Rev. Chim., vol. **61**, no. 9, pp. 828–832, 2010

[14] M. Okayasu, Y. Ohkura, S. Takeuchi, S. Takasu, H. Ohfuji, and T. Shiraishi, *A study of the mechanical properties of an Al-Si-Cu alloy (ADC12) produced by various casting processes*, Mater. Sci. Eng. A, vol. **543**, pp. 185–192, May 2012

[15] L. Y. Zhang *et al.*, *Effect of cooling rate on solidified microstructure and mechanical properties of aluminium-A356 alloy*, J. Mater. Process. Technol., 2008

[16] L. A. Dobrzański, R. Maniara, J. Sokołowski, and W. Kasprzak, *Effect of cooling rate on the solidification behavior of AC AlSi7Cu2 alloy*, J. Mater. Process. Technol., vol. **191**, no. 1–3, pp. 317–320, 2007

[17] A. M. Samuel and F. H. Samuel, *Effect of alloying elements and dendrite arm spacing on the microstructure and hardness of an Al-Si-Cu-Mg-Fe-Mn (380) aluminium die-casting alloy*, J. Mater. Sci., vol. **30**, no. 7, pp. 1698–1708, 1995

[18] N. Saheb, T. Laoui, A. R. Daud, M. Harun, S. Radiman, and R. Yahaya, *Influence of Ti addition on wear properties of Al-Si eutectic alloys*, Wear, vol. **249**, no. 8, pp. 656–662, 2001

[19] C. H. Caceres, M. B. Djurdjevic, T. J. Stockwell, and J. H. Sokolowski, *The effect of Cu content on the level of microporosity in Al-Si-Cu-Mg casting alloys*, Scr. Mater., vol. **40**, no. 5, pp. 631–637, 1999

[20] M. Zeren, E. Karakulak, and S. Gümü, *Influence of Cu addition on microstructure and hardness of near-eutectic Al-Si- x Cu-alloys*, Trans. Nonferrous Met. Soc. China, vol. **21**, pp. 1698–1702, 2011

[21] A. Darlapudi, S. D. Mcdonald, and D. H. Stjohn, *The influence of ternary Cu additions on the nucleation of eutectic grains in a hypoeutectic Al-10 wt .% Si alloy*, J. Alloys Compd., vol. **646**, pp. 699–705, 2015

[22] R. Taghiabadi, A. Fayegh, A. Pakbin, M. Nazari, and M. H. Ghoncheh, *Quality index and hot tearing susceptibility of Al–7Si–0.35Mg–xCu alloys*, Trans. Nonferrous Met. Soc. China, vol. **28**, pp. 1275–1286, 2018

[23] G. Heiberg, K. Nogita, A. L. Dons, A. K. Dahle, and L. Arnberg, *Effect of magnesium, iron and copper on eutectic solidification of hypoeutectic aluminum-silicon alloys*, AFS Trans., pp. 347–358, 2002

[24] J. J. Friel, *Practical guide to image analysis*, 1st ed. Materials Park, OH, 44073-0002:

ASM international, 2000

[25] X. Chen, H. Geng, and Y. Li, *Assessment of modification level of hypoeutectic Al-Si alloys by pattern recognition of cooling curves*, China Foundry, vol. **2**, no. 4, pp. 246–253, 2005

[26] L. Lattanzi, A. Fortini, M. Giovagnoli, and M. Merlin, *Influence of Mg and Ti on both eutectic solidification and modifying efficiency in Sr-modified Al-7Si cast alloys*, Metall. Ital., vol. **110**, no. 2, pp. 5–15, 2018

[27] M. Djurdjevic, H. Jiang, and J. Sokolowski, *On-line prediction of aluminum-silicon eutectic modification level using thermal analysis*, Mater. Charact., vol. **46**, no. 1, pp. 31–38, 2001

[28] G. Heiberg, C. Gandin, H. Goerner, and L. Arnberg, *Experimental and Modeling Studies of the Thermal Conditions and Magnesium , Iron , and Copper Content on the Morphology of the Aluminum Silicon Eutectic in Hypoeutectic Aluminum Silicon Alloys*, Metall. Mater. Trans. A, vol. **35A**, pp. 2981–2991, 2004

[29] G. Heiberg, K. Nogita, A. K. Dahle, and L. Arnberg, *Columnar to equiaxed transition of eutectic in hypoeutectic aluminium-silicon alloys*, Acta Mater., vol. **50**, no. 10, pp. 2537–2546, 2002

[30] A. Darlapudi, S. D. McDonald, S. Terzi, A. Prasad, M. Felberbaum, and D. H. StJohn, *The influence of ternary alloying elements on the Al-Si eutectic microstructure and the Si morphology*, J. Cryst. Growth, vol. **433**, pp. 63–73, 2016

[31] S. El-Hadad, A. M. Samuel, F. H. Samuel, H. W. Doty, and S. Valtierra, *Effects of Bi and Ca addition on the characteristics of eutectic Si particles in Sr-modified 319 alloys*, Int. J. Cast Met. Res., vol. **15**, no. 5, pp. 551–564, 2003

[32] A. M. Samuel, H. W. Doty, S. V. Gallardo, and F. H. Samuel, *The effect of Bi-Sr and Ca-Sr interactions on the microstructure and tensile properties of Al-Si-based alloys*, Materials (Basel)., vol. **9**, no. 3, 2016

[33] S. S. Sreeja Kumari, R. M. Pillai, K. Nogita, A. K. Dahle, and B. C. Pai, *Influence of calcium on the microstructure and properties of an Al-7Si-0.3Mg-xFe alloy*, Metall. Mater. Trans. A, vol. **37**, no. 8, pp. 2581–2587, 2006

[34] T. H. Ludwig, E. Schonhovd Dæhlen, P. L. Schaffer, and L. Arnberg, *The effect of Ca and P interaction on the Al-Si eutectic in a hypoeutectic Al-Si alloy*, J. Alloys Compd., vol. **586**, pp. 180–190, 2014

[35] Y. H. Cho, H.-C. Lee, K. H. Oh, and A. K. Dahle, *Effect of strontium and phosphorus on eutectic Al-Si nucleation and formation of β-Al5FeSi in hypoeutectic Al-Si foundry alloys*, Metall. Mater. Trans. A, vol. **39A**, no. 10, pp. 2435–2448, 2008

[36] S. D. McDonald, A. K. Dahle, J. A. Taylor, and D. H. StJohn, *Eutectic grains in unmodified and strontium-modified hypoeutectic aluminum-silicon alloys*, Metall. Mater. Trans. A Phys. Metall. Mater. Sci., vol. **35 A**, no. 6, pp. 1829–1837, 2004

CHAPTER 3

Cu ADDITION

The present chapter reports the research work performed at the Department of Materials and Manufacturing of the Jönköping University, under the supervision of Professor Seifeddine and Professor Ghassemali. The work aims to better understand the influence of Cu on the microstructure of AlSi7Mg alloys and, as a consequence, on the crack propagation behaviour.

3.1 AIM AND PURPOSE OF THE WORK

Limited research focused on the role of microstructural features of cast Al-Si alloys in influencing the fatigue crack mechanisms. Since defects levels decrease with molten metal treatments and optimised casting processes, an understanding of initiation and propagation mechanisms from a small-scale microstructural point of view (i.e. SDAS, the strength of the α-Al matrix, morphology and distribution of Si particles) becomes critical. For this reason, in the past two decades, Lados *et al.* focused their attention on the influence of such microstructural features on long and small fatigue crack growth in heat-treated Al-Si-Mg alloys. They reported that grain size has no significant impact on the fatigue crack growth response, while the crack growth threshold and fracture toughness also depend on SDAS [1]. In particular, large SDAS materials show high threshold and low fracture toughness.

Regarding the Al matrix strength, crack growth rate is higher for T4 samples (low yield strength matrix) than for T6 samples in upper region II and lower region III of the Paris curve. In upper region III, T4 samples show better fatigue crack growth resistance due to the ductile tearing of the softer Al matrix [2]. About Si particles, unmodified alloys show higher thresholds compared to the modified alloys, but the latter ones present better fatigue crack growth characteristics than unmodified alloys in region III, meaning higher toughness [1]–[3].

To date, there has not been a detailed investigation about fatigue crack growth focused on the influence of Cu microstructural features in Cu-added Al-Si-Mg systems. The influence of Cu, involved either in intermetallic compounds or in promoting shrinkage porosity, on the tensile properties has been the focus of several studies.

Nevertheless, little attention has been paid to the role that Cu solid solution and Cu-based phases play in influencing fatigue crack nucleation and propagation. A deep understanding of the link between cracking behaviour and as-cast microstructure is necessary to properly design components, from the alloy to the heat treatment selection. In facts, the knowledge of the as-cast properties is helpful to understand better and predict the influence of heat treatments. In light of the as-cast behaviour, heat treatment itself could be re-designed to optimise its effects. The present study aims to investigate the influence of Cu related microstructural features on crack nucleation and propagation through *in-situ* cyclic tests in the SEM and compares AlSi7Mg alloys with different Cu contents. Miniaturised Compact Test (CT) samples are employed for *in-situ* cyclic tests and DIC enables to measure the equivalent Von Mises strain distribution and to evaluate its interaction with the crack path. The speckle pattern for Digital Image Correlation (DIC) is produced by Focused Ion Beam (FIB) milling, a versatile method proposed by Kasvayee *et al.* [4].

3.2 MATERIALS AND EXPERIMENTAL PROCEDURE

3.2.1 Melt preparation

Pure Al ingots and pure Si were melted in a boron nitride coated crucible to prepare four A356 alloys with different Cu additions. An Al-50Mg master alloy was added to reach the Mg content of 0.4 wt.%. Different Cu contents were obtained with the addition of an Al-50Cu master alloy. After complete melting, refining Al-5Ti-1B and modifying Al-10Sr master alloys were also added to obtain the targeted contents of 650 ÷ 700 ppm of Ti and 200 ÷ 250 ppm of Sr. Table 3. 1 reports the chemical composition of each alloy, evaluated with a Spectromaxx CCD LMXM3 optical emission spectrometer. The quality of the melt was monitored using thermal analysis.

Table 3. 1 – Chemical composition of the investigated alloys for different Cu additions [wt.%]

Alloy name	Si	Fe	Cu	Mg	Ti	Sr [ppm]	Al
Cu 0.0	6.80	0.10	-	0.38	0.07	260	bal.
Cu 0.5	7.01	0.09	0.51	0.37	0.07	230	bal.
Cu 1.5	7.14	0.09	1.61	0.38	0.07	230	bal.
Cu 3.0	6.98	0.17	3.23	0.36	0.08	210	bal.

Cooling curves were recorded for each alloy before and after the addition of the refining and modifying rods, to verify their effect on solidification and to assess the influence of

Cu (Figure 3. 1a-d). The first derivative of the regions before *liquidus* and after *solidus* was well-fitted ($R^2 > 0.9999$) by a two-term exponential baseline.

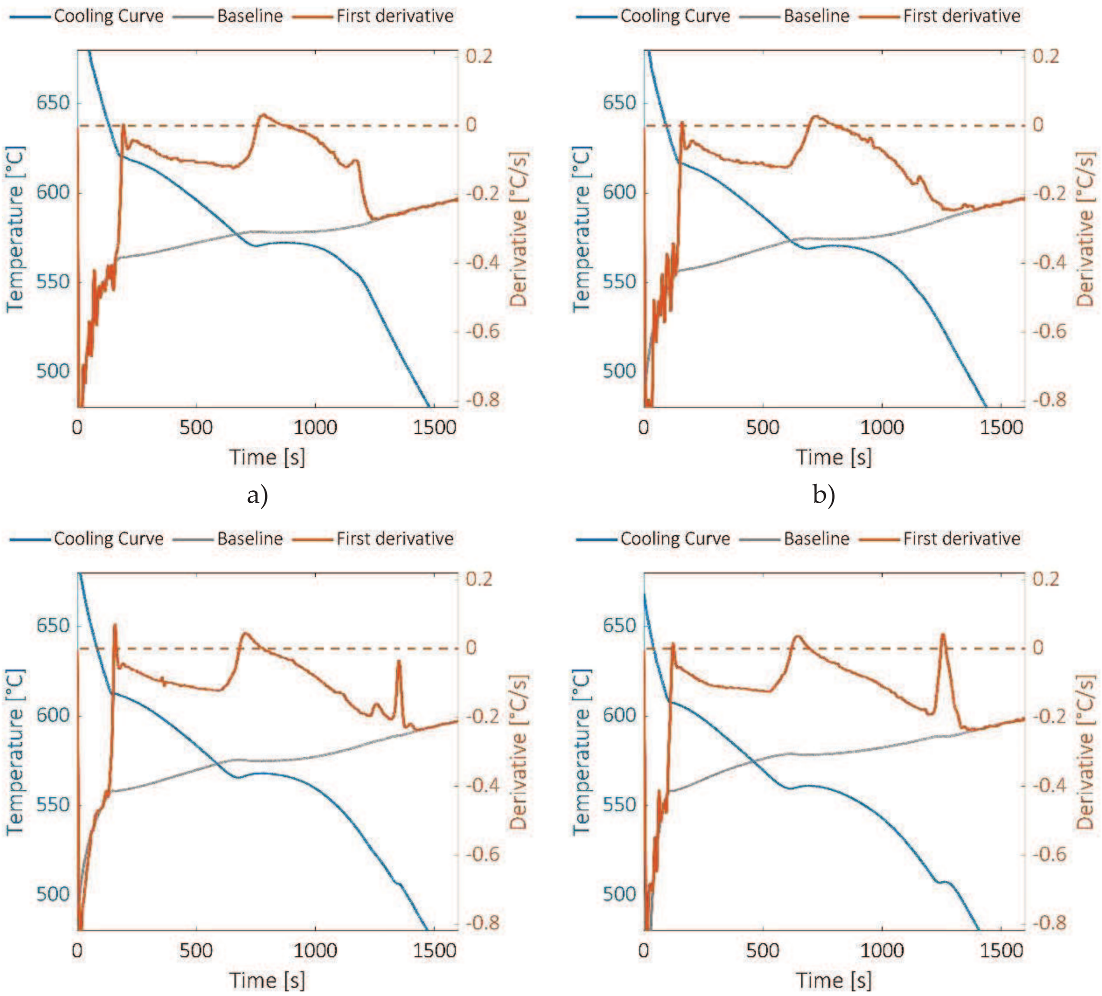

a) b) c) d)

Figure 3. 1 – Cooling curve, first derivative and baselines: a) alloy Cu 0.0; b) alloy Cu 0.5; c) alloy Cu 1.5; d) alloy Cu 3.0

3.2.2 Mechanical tests

Cylindrical rods with a length of 150 mm and diameter of 9 mm were cast in a pre-heated graphite coated permanent mould. The rods were re-melted at 730 °C for 30 minutes in an inert gas atmosphere and then drawn from a directional solidification furnace raising at a ~ 6 mm/s (Figure 3. 2), in order to obtain a targeted SDAS of ~ 10 μm and targeted grain size of ~ 90 μm. Both tensile bars and CT samples were obtained from the directionally solidifed rods. Tensile tests were performed at room temperature with a costant cross-head speed of 0.5 mm/min, and a minimum of three samples was tested for each condition. The miniaturised CT samples depicted in Figure 3. 3a were cut by electron discharge machining method with a wire of 0.25 mm diameter. The dimensions of the CT samples were designed and modified according to the ASTM E647-00 Standard. CT samples were mechanically polished and slightly etched with a 10 % NaOH solution.

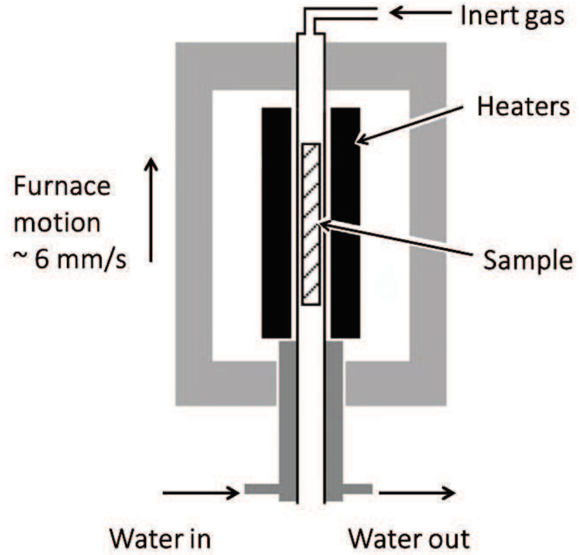

Figure 3. 2 – Schematic image of the directional solidification equipment

Several SEM-related techniques enabled to characterise Cu-based phases. Wavelength Dispersive X-ray Spectroscopy (WDS) permitted to measure the content of Cu in the primary Al matrix, both in the centre and at the edge of the dendrite, while Energy Dispersive X-ray Spectroscopy (EDS) was employed to identify different Cu phases. The Thermocalc Scheil simulation is a useful tool to predict the solidification sequence and the number of different phases in the investigated alloys.

In-situ cyclic tests were performed on the Kammrath & Weiss module, depicted in Figure 3. 3b, inside a Tescan Lyra3 FIB-SEM, equipped with a Ga ion source.

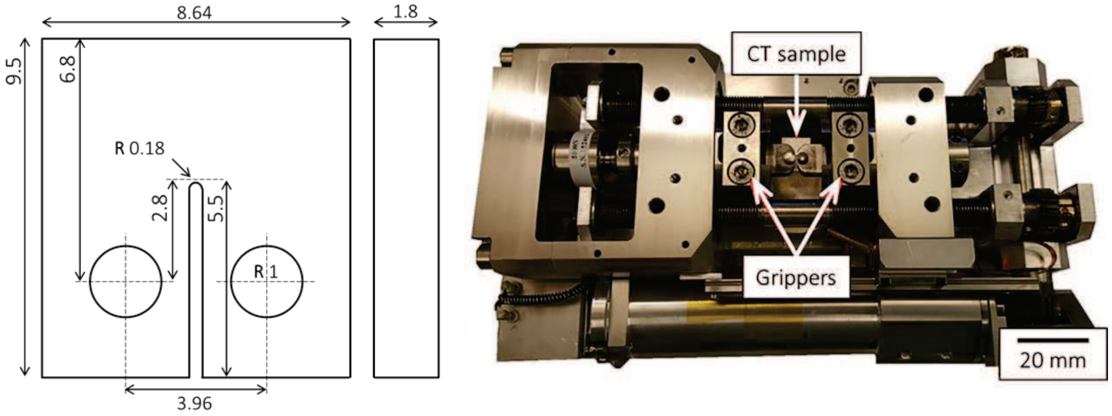

a) b)

Figure 3. 3 – a) Dimensions of the CT sample in mm; b) Miniature stage for *in-situ* cyclic tests

Electron Backscattered Diffraction (EBSD) maps were acquired before and after the *in-situ* cyclic tests, in order to follow the interaction between the crack path and the grain boundaries. Before cyclic loading, monotonic tension loading up to failure (Figure 3. 4) showed that the crack initiated at the notch with a load of 220 ÷ 245 N for all the alloys.

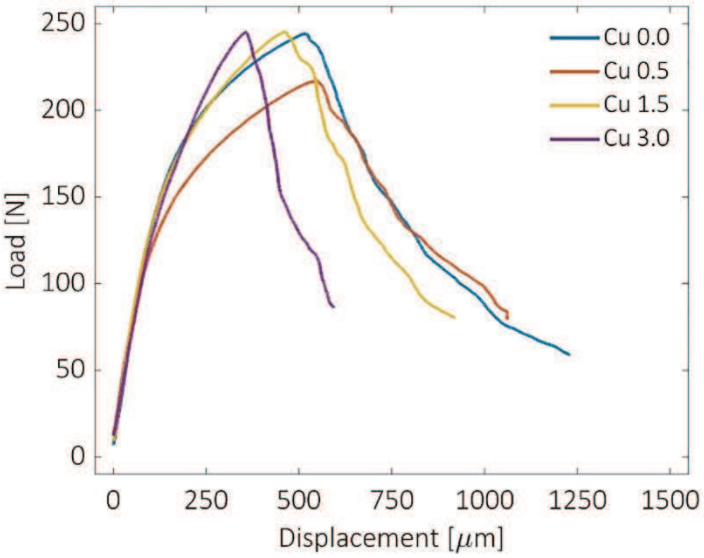

Figure 3. 4 – Monotonic tension curves of the CT samples

The critical stress intensity factor Kc that corresponds to 245 N is equal to 21 ± 0.4 MPa·√m, following the Equation (3. 1) provided by the ASTM E647-00 standard:

$$K = \frac{P}{B \cdot \sqrt{W}} \cdot \frac{(2+\alpha)}{\sqrt{(1-\alpha)^3}} \cdot (0.886 + 4.64 \cdot \alpha - 13.32 \cdot \alpha^2 + 14.72 \cdot \alpha^3 - 5.6 \cdot \alpha^4) \quad (3.\ 1)$$

where $P\ [N]$ is the load. For the geometry of the sample, $B = 1.8\ mm$, $W = 6.8\ mm$ and $\alpha = 0.5882$. To the knowledge of the author, values of the ΔK threshold for the investigated alloys in the as-cast condition are not available in the literature. Available data report a ΔK threshold range of 3.3 ÷ 5.1 MPa·√m for unmodified and Sr-modified A356 and A319 alloys in the T4, T61, and T71 heat-treated conditions. In light of data available in the literature, $\Delta K = (1 - R)K_{max}$ was imposed equal to 12 MPa·√m, with the load ratio R of 0.2 and K_{max} of 15 MPa·√m. A preload of 200 N was applied and a minimum of two samples was tested for each condition. Each sample survived at least 300 cycles. The crosshead speed was 10 μm/s, that correspond to ~ 6 cycles/min and thus ~ 0.1 Hz. FIB milling was used to produce a random speckle pattern for DIC analysis, according to the method proposed and validated by Kasvayee *et al*. [4] in a previous work on cast iron samples. Figure 3. 5 depicts the surface of the CT sample before (Figure

3. 5a) and after (Figure 3. 5b) FIB milling. The speckles generated are squares 1 x 1 µm² and 1.5 µm depth. The milled area is a 300 x 300 µm² square around the notch tip and contains 2500 random speckles. The NaOH etching enables to maintain a good contrast between the Si particles and the α-Al matrix in the secondary electron images, even after the FIB pattern generation.

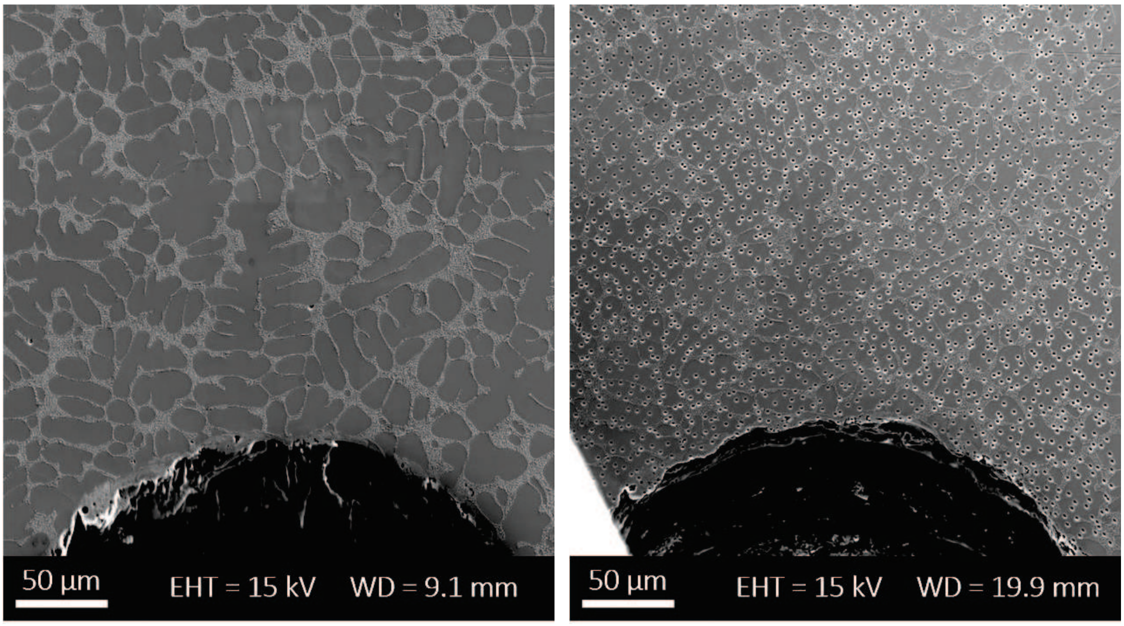

a) b)

Figure 3. 5 – CT sample surface a) before and b) after FIB milling for pattern generation

DIC was performed with the commercial software MatchID to obtain the strain distribution on the deformed micrographs at different cycles. Table 3. 2 presents the correlation parameters used for the DIC analysis. The size of the field of view (FOV) was 300 x 300 µm², and it comprehended the notch tip to investigate the local strain development. The Von Mises equivalent strain, among other strains, is chosen as output. It combines the horizontal and vertical strains as described in Equation (3. 2):

$$\varepsilon_{eq} = \frac{2}{3} \cdot \sqrt{\left(\varepsilon_{xx}^2 + \varepsilon_{yy}^2 - \varepsilon_{xx} \cdot \varepsilon_{yy}\right) + 3 \cdot \varepsilon_{xy}} \tag{3. 2}$$

in accordance with the Von Mises yield criterion.

Table 3. 2 – Parameters of the DIC analysis

Parameter	Value
Pixel size [mm]	0.24
SS = Subset size [pixel]	61
ST = Step size [pixel]	8

Correlation criterion	zero-normalized sum of squared difference
Shape function	quadratic
Interpolation function	bi-cubic polynomial
Displacement standard deviation [pixel]	0.1
SW = Strain window size [pixel]	15
SSR = Strain spatial resolution [pixel] = SS + [(SW-1)·ST]	173 (42 µm)

3.2.3 Microstructure evaluation

The different secondary phases were observed with a Zeiss EVO SEM and identified through EDS. The area fraction on Cu-phases was determined with the evaluation of 30 frames of area 7.3 SDAS x 5.7 SDAS for the Cu added alloys, according to previous work [5]. The concentrations of Mg, Cu and Si in the α-Al matrix were measured using WDS. Measurements were made over dendrite arms, both on the side and in the centre of the dendrite arm, a minimum of 5 points per samples. The acceleration voltage was set to 20 kV for Cu, and 10 kV for Mg and Si measurements and pure elements were used as standards. Dwell times were set to achieve about 600 counts above the background counts at the peak energy for the element of interest.

3.3 RESULTS AND DISCUSSION

The following paragraphs report the results of microstructural characterisation and mechanical investigations with the related discussion.

3.3.1 Microstructural characterisation

Table 3. 3 reports the main results of the microstructural investigations on the alloys. The SDAS was measured and, as expected from the cooling rate during directional solidification, results an average value of 9 ± 0.7 µm, that corresponds to a cooling rate (CR) of 42.8 °C/s according to the relation $CR = 2\cdot10^{4}\cdot SDAS^{-2.67}$ proposed by Samuel and Samuel for Al foundry alloys [6]. The average grain size of the alloys was 90 ± 2 µm, confirming that the four alloys were in the same grain refining condition. Similarly, the modification treatment on the alloys led to Si particles with comparable dimensional and geometrical parameters, i.e. area, equivalent diameter, aspect ratio (length/width) and

roundness. The directional solidification did not affect the microstructure, which presents the same features in both longitudinal and cross directions.

Table 3. 3 – Microstructural characteristics of the alloys. Error is the standard error

Alloy	AGS [µm]	SDAS [µm]	Si particles ED [µm]	Si particles Aspect Ratio	Si particles Area [µm^2]	Si particles Roundness
Cu 0.0	85 ± 5	8.9 ± 0.7	0.4 ± 0.01	2.0 ± 0.04	0.2 ± 0.01	2.1 ± 0.04
Cu 0.5	85 ± 5	9.0 ± 0.8	0.4 ± 0.01	1.9 ± 0.03	0.2 ± 0.01	2.0 ± 0.03
Cu 1.5	95 ± 9	9.2 ± 0.2	0.5 ± 0.01	1.9 ± 0.03	0.3 ± 0.01	2.0 ± 0.03
Cu 3.0	94 ± 10	8.8 ± 0.1	0.4 ± 0.01	1.9 ± 0.03	0.2 ± 0.01	2.2 ± 0.04

WDS measurements permitted to verify the content of Cu in the primary α-Al matrix, both in the centre and at the edge of the dendrite. As reported in Table 3. 4, in Alloy Cu 0.5 there is not a difference in Cu content between the centre and the edge of the dendrite.

Table 3. 4 – Cu content of microstructural components. Error is the standard error

	Primary α-Al			Q Phase		θ Phase	
Alloy	Cu [wt. %] center	Cu [wt. %] edge	HV$_{0.01}$	Area %	Cu [wt.%]	Area %	Cu [wt.%]
Cu 0.0	-	-	63.9 ± 0.1	-	-	-	-
Cu 0.5	0.11 ± 0.01	0.11 ± 0.02	68.1 ± 0.0	0.5	0.11	-	-
Cu 1.5	0.37 ± 0.03	0.51 ± 0.07	70.3 ± 0.1	1.4	0.29	0.8	0.43
Cu 3.0	0.74 ± 0.04	0.90 ± 0.13	75.5 ± 0.0	2.2	0.45	2.6	1.39

For alloys Cu 1.5 and Cu 3.0, the edge of the dendrite results slightly richer in Cu than the centre. This concentration profile in the dendrite agrees with the Al-Cu phase diagram and becomes more evident as the Cu content increases. For the four alloys, the content of Si and Mg in the matrix at the centre of the dendrite resulted in 1.47 ± 0.09 wt. % and 0.03 ± 0.01 wt.%, respectively. The WDS measurements of Cu, Si and Mg solid solution in the α-Al matrix agree with previous work by Sjölander and Seifeddine [7].

The cooling curves in Figure 3. 6 highlight the effect that Cu has the characteristic temperatures of the AlSi7Mg0.3 alloy. As the Cu content increases, the solidification temperatures of both the primary Al phase and the eutectic decrease. This behaviour agrees with the observations reported in the literature [8]–[12] and related to the thermodynamic effect of Cu on the Al-Si phase diagram.

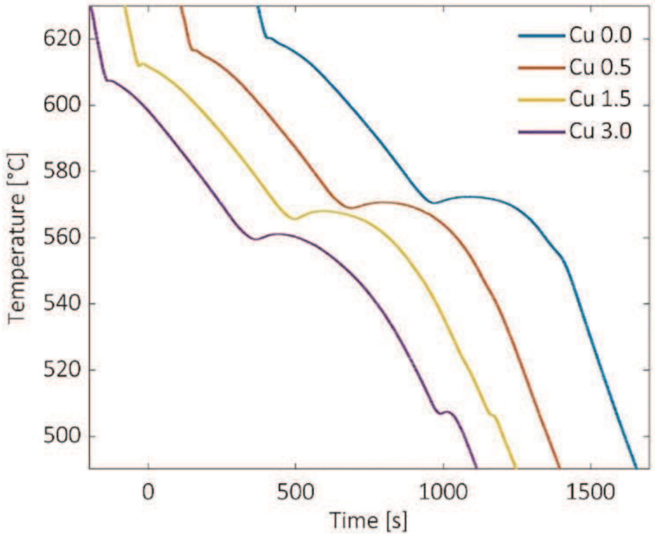

Figure 3. 6 – Cooling curves of the alloys

The thermal parameters in Table 3. 5 result from the cooling curves in Figure 3. 6 and confirm the role that Cu has in decreasing the solidification temperature of the alloys.

Table 3. 5 – Thermal parameters of the alloys

Phase	T [°C]	Cu 0.0	Cu 0.5	Cu 1.5	Cu 3.0
Primary α-Al	T_N	620.5	619.4	618.3	617.7
	T_M	620.3	616.5	612.6	607.4
	T_G	620.3	616.6	612.5	607.5
	ΔT_R	0.1	0.1	0.1	0.1
Al-Si eutectic	T_N	580.6	580.8	580.7	580.8
	T_M	571.3	569.9	566.2	560.3
	T_G	572.3	570.7	567.1	561.1
	ΔT_R	1.0	0.8	0.9	0.8

The nucleation temperature of primary α-Al decreases continuously from 620.5 to 617.7 °C as the Cu content increases up to 3 wt.%. Similarly, minimum and growth temperature decrease but the recalescence value remains constant. The latter result confirms that alloys are all in the same grain refining condition, as expected. The eutectic temperatures follow the same trend, with an inverse relationship with the Cu content in the alloy. The ΔT_R values present a limited variation, and it should correspond to a stable solidification front and a comparable modification condition.

Figure 3. 7 compares the solid fraction curve calculated via the Scheil simulation in Thermo-Calc Software® and through the recorded cooling curves. The Scheil simulation predicts that with increasing Cu, the solidification sequence changes slightly. In the alloys with Cu content lower than 0.5 wt.% (Figure 3. 7a,c), Mg leads to the formation of β-Mg_2Si and π-AlFeMgSi phases. As the Cu content in the alloy increases to 1.5 wt.%

(Figure 3. 7e), Mg is involved in π-AlFeMgSi and Q-$Al5Mg_8Cu_2Si_6$ phases, and a limited fraction of θ-Al_2Cu also precipitates. In the alloy Cu 3.0 (Figure 3. 7g), the main intermetallic compounds are Q-$Al_5Mg_8Cu_2Si_6$ and θ-Al_2Cu phases. The intermetallic compounds that contain Mg and Cu nucleate in the interdendritic region, after the eutectic nucleation. The solid fraction evolution calculated by cooling curves well relates to the simulated one. The alloy Cu 0.0 presents the solidification peak that confirms the precipitation of the β phase (Figure 3. 7b). The addition of 0.5 wt.% of Cu determines at first the presence of the Q phase that contains both Cu and Mg (Figure 3. 7d). The main Cu-based phase becomes the θ phase as the Cu content further increases to 3 wt.% (Figure 3. 7f, h). The solidification range is slightly wider in the real solid fraction curves that in the simulated ones.

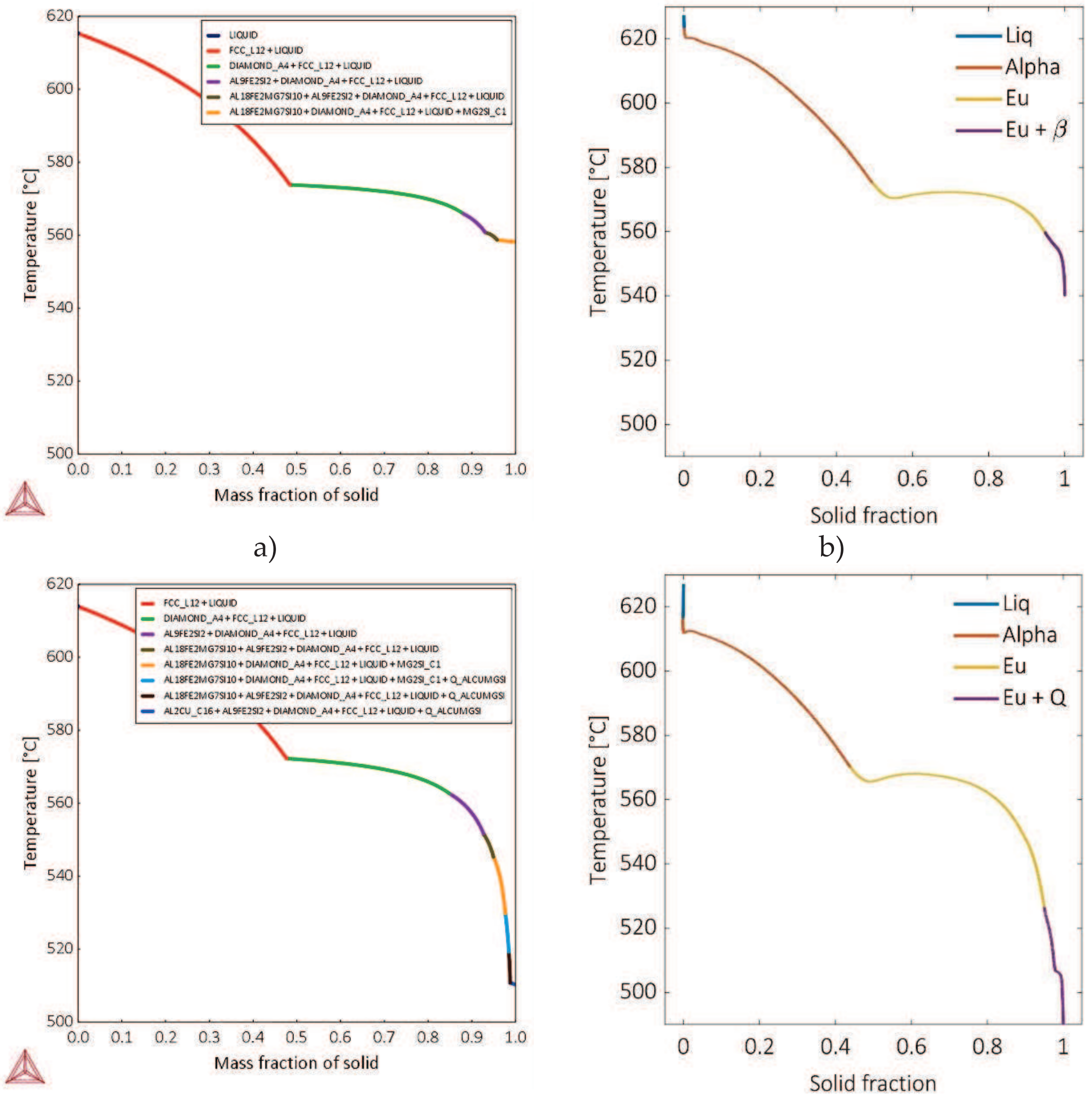

a)

b)

c)

d)

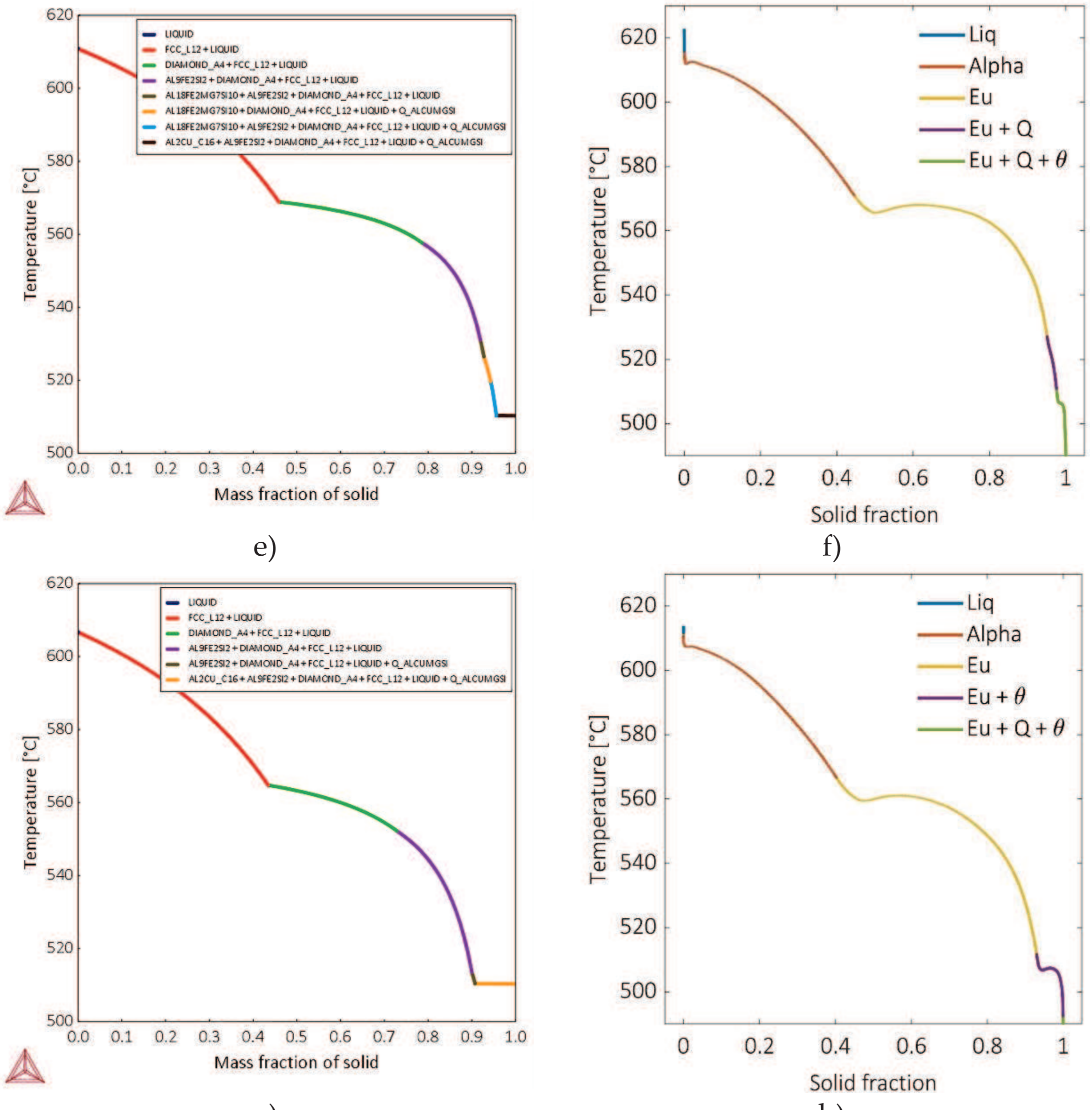

e) f)

g) h)

Figure 3. 7 – Temperature v. solid fraction. Scheil simulations: a) alloy Cu 0.0, c) alloy Cu 0.5, e) alloy Cu 1.5, g) alloy Cu 3.0; thermal analysis: b) alloy Cu 0.0, d) alloy Cu 0.5, f) alloy Cu 1.5, h) alloy Cu 3.0

SEM observations with EDS analyses enabled to distinguish Q and θ phases in alloy Cu 3.0, as depicted in Figure 3. 8 and confirmed that Cu is mainly involved in Q phase in alloys Cu 0.5 and Cu 1.5. Both phases precipitate in the interdendritic region and appear deeply interconnected to each other and with eutectic Si.

The Cu-based Q and θ phases do not show a specific morphology, but they are coarser than eutectic Si particles. The θ phase in alloy Cu 3.0 presents both the fine eutectic morphology (Figure 3. 8a), linked to Si particles because of the ternary eutectic reaction (3. 3):

$$Liquid \rightarrow \alpha Al + Si + \theta Al_2Cu \qquad (3.\ 3)$$

as reported by Edwards [13], and the polygonal morphology (Figure 3. 9a). Several studies confirmed that the presence of Sr increases the tendency to form the blocky θ-Al_2Cu [14]–[17].

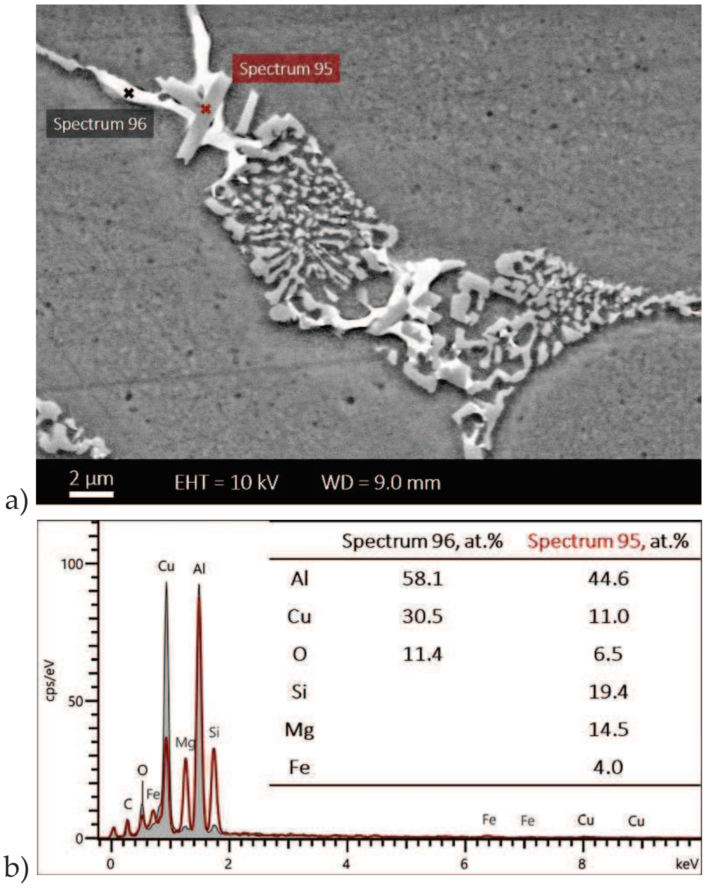

	Spectrum 96, at.%	Spectrum 95, at.%
Al	58.1	44.6
Cu	30.5	11.0
O	11.4	6.5
Si		19.4
Mg		14.5
Fe		4.0

Figure 3. 8 – Eutectic θ-phase: a) SE image of Alloy Cu 3.0 and b) related EDS spectra

Samuel *et al.* [14] observed that the different morphologies of Cu-based θ phase correspond to a different amount of Cu content: the polygonal form presents ~ 40 wt.% of Cu while the eutectic one has the ~ 24 wt.% of Cu.

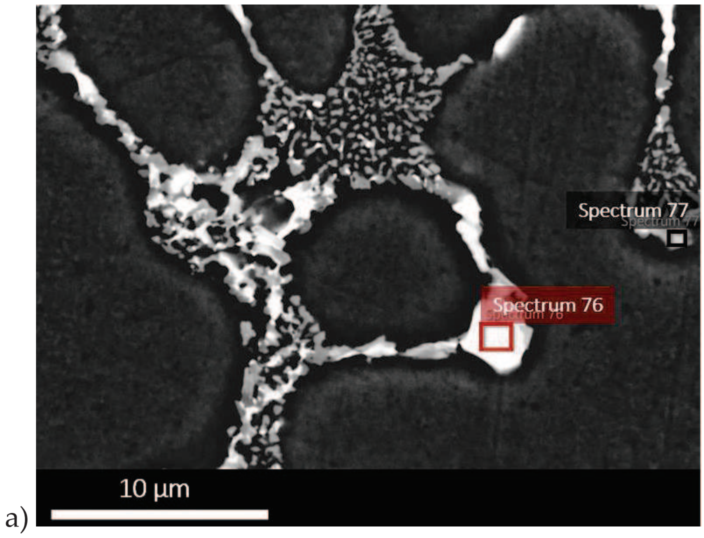

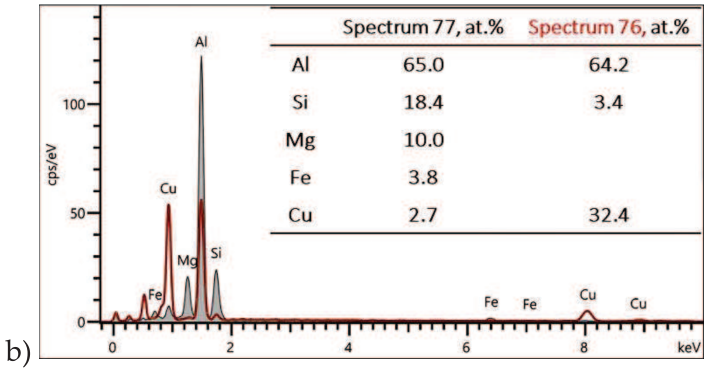

	Spectrum 77, at.%	Spectrum 76, at.%
Al	65.0	64.2
Si	18.4	3.4
Mg	10.0	
Fe	3.8	
Cu	2.7	32.4

Figure 3. 9 – Polygonal θ-phase a) SE image of Alloy Cu 3.0 and b) related EDS spectra

The cooling rate, the presence of the β phase and the modification with Sr are factors that influence the morphology of the θ phase. The EDS spectra show that the blocky morphology (Figure 3. 9b) presents a slightly higher atomic content of Cu that the eutectic one (Figure 3. 8b).

Table 3. 4 also reports the area fraction of Cu phases and their Cu wt.% content in each alloy. As expected, only Q phase is present in the alloy Cu 0.5 while in the alloys Cu 1.5 and Cu 3.0 Q and θ phases are both detectable. The amount of Cu content in the intermetallic phases is in line with the WDS measurements of the Cu content in the primary matrix.

3.3.2 Tensile and *in-situ* cyclic tests

Table 3. 6 lists the tensile properties, obtained via tensile tests, and they are in agreement with the literature results of Table 1. 5: elongation continuously decreases while YS increases with increasing Cu content in the alloys. The percentage increase of YS is comparable to the results reported by Seifeddine *et al.* [18], who investigated alloys with chemical compositions, modification treatment and solidification conditions similar to the ones described in the present work. The UTS drop is observed with the Cu content of 3 wt.%, while other authors reported the drop at lower Cu contents, around 1.5 ÷ 2 wt.%.

Table 3. 6 – Mechanical properties of the alloys. Error is the standard error

Alloy	YS [MPa]	Δ_{YS} [%]	UTS [MPa]	Δ_{UTS} [%]	e [%]	Δ_e [%]
Cu 0.0	107 ± 0.3		255 ± 0.2		19 ± 0.3	
Cu 0.5	117 ± 0.3	+ 9	281 ± 2.5	+ 10	15 ± 2.2	- 21
Cu 1.5	136 ± 0.1	+ 27	317 ± 1.0	+ 24	14 ± 0.4	- 26
Cu 3.0	149 ± 0.2	+ 39	252 ± 9.0	- 1.2	2 ± 0.3	- 90

Fatigue cracks are expected to seek the path of least resistance, offered by the most damaged microstructural feature ahead of them. According to the EBSD pattern acquired before (Figure 3. 10) and after (Figure 3. 11) failure, cracks propagate with trans-granular paths in all the investigated alloys.

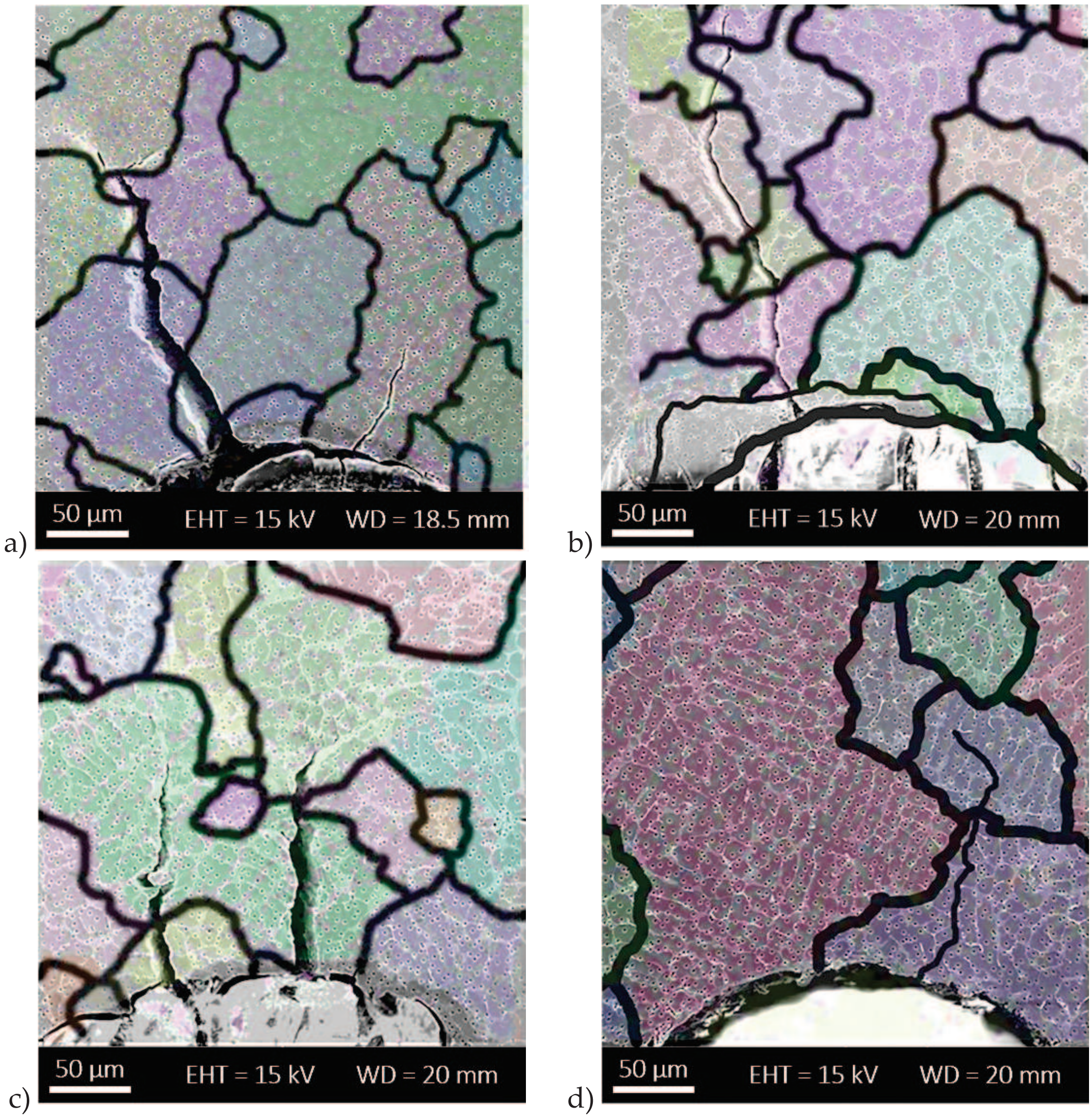

Figure 3. 10 – SEM images of crack paths overlapped to the related EBSD pattern: a) alloy Cu 0.0; b) alloy Cu 0.5; c) alloy Cu 1.5; d) alloy Cu 3.0 (drawn of the crack path)

Figure 3. 10d reports the draw of the crack path to underline the trans-granular and trans-dendritic behaviour. Propagation is also trans-dendritic as cracks cross the primary α-Al matrix in all cases. DIC analysis, in some cases, highlights the highest strain concentration at the grain boundary, but the crack in proximity does not follow that path and propagates across the dendrite arms.

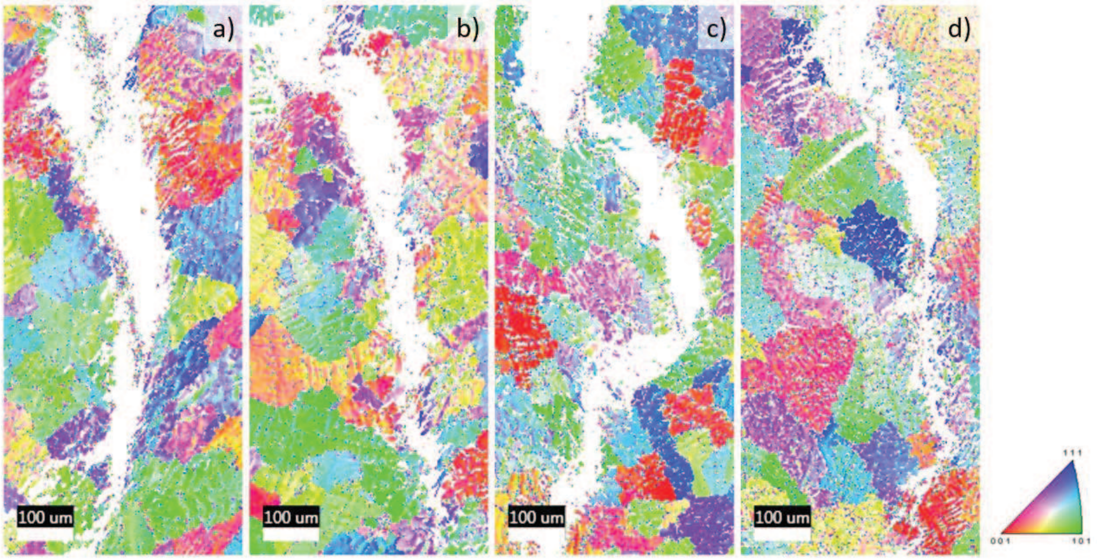

Figure 3. 11 – EBSD patterns (inverse polar figure) of the alloys after failure: a) alloy Cu 0.0; b) alloy Cu 0.5; c) alloy Cu 1.5; d) alloy Cu 3.0. The white regions correspond to the cracks

Evident slip bands appear in the region that surrounds the propagating crack during the cycling test in the alloy Cu 0.0 (Figure 3. 12a,c). With increasing Cu, the α-Al matrix results strengthened, as confirmed by microhardness measures reported in Table 3. 6, and slip bands become less and less visible in regions far 100 ÷ 150 μm from the crack (Alloy Cu 1.5 in Figure 3. 12c). Slip bands remain evident at the crack edge (Figure 3. 12d). Nevertheless, propagation prefers the α-Al matrix over Si particles and Cu-based compounds. Crack propagation becomes more difficult as Cu content in the primary matrix increases, and the crack path is less straight as hindered somehow by the strengthening of the matrix. In this case, brittle components as Si particles and Cu phases were expected to behave as a preferential path for propagation, but this phenomenon does not seem to occur.

Lados *et al.* [19] studied the fatigue crack propagation in T61 and T4 heat-treated A356 alloys and reported that crack path changes with increasing ΔK. Crack propagates in primary dendrites for ΔK of 5 MPa·√m and progressively moves towards eutectic interdendritic regions as ΔK increases to 12 MPa·√m. In the present study, cracks are trans-dendritic during all the tests, either propagating along the centre of the dendrite or across its arms. It does not follow the interdendritic region cracking Si particles and Cu bearing phases. The presence of Cu phases does not weaken the fatigue behaviour of the alloy because those phases, although often cracked and debonded from the matrix, do not interfere with the crack path. The matrix strength becomes a critical factor since it represents the favourite way of propagation, and the Cu content has a definite effect on the matrix strengthening, as reported in Table 3. 6. Primary α-Al strengthened by retained Cu atoms is less prone to deformation, as can be deduced from Figure 3. 12b,d, and hinders crack propagation. Figure 3. 12 depicts the deformation of the primary α-Al in the alloy Cu 0.0, and the slip bands are visible at the crack edge (Figure 3. 12c) and further from it (Figure 3. 12a). On the contrary, the primary α-Al in the alloy Cu 1.5 does not present slip bands in the region at ~ 150 μm from the crack edge (Figure 3. 12b) and limited deformation is visible in the vicinity of the crack (Figure 3. 12d).

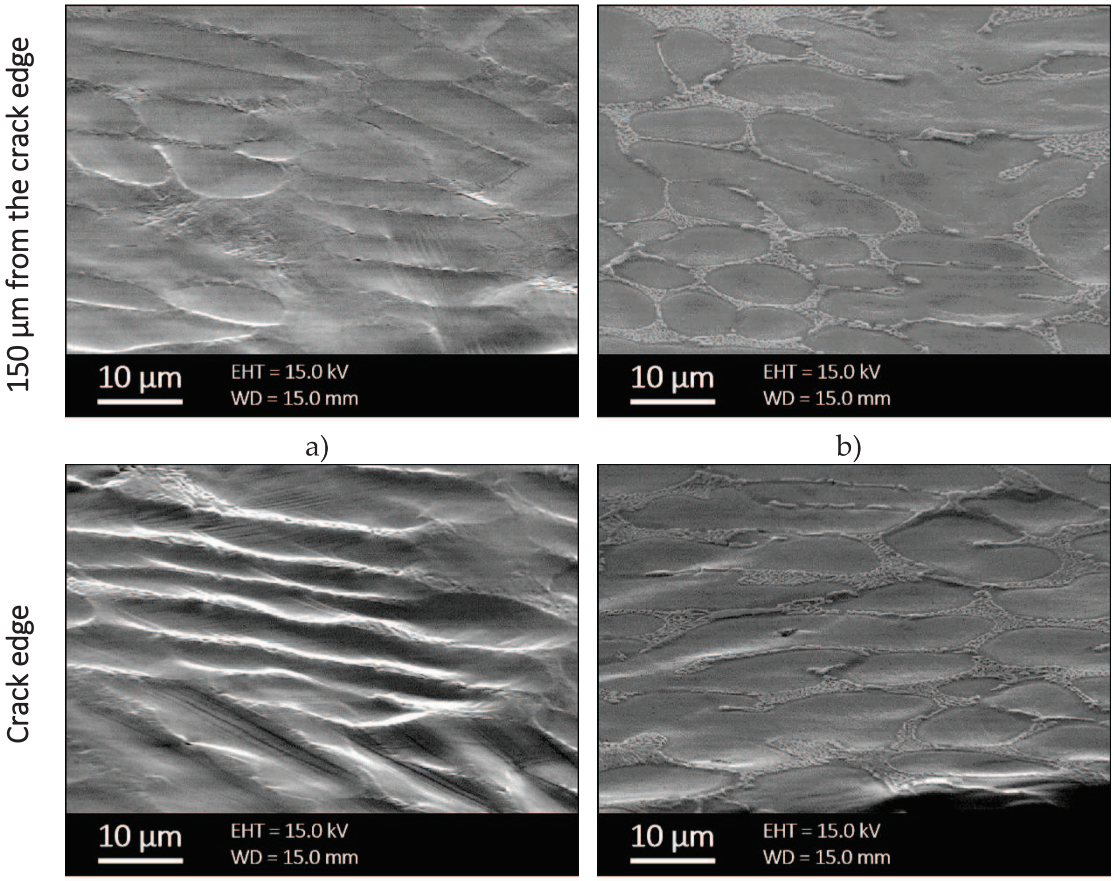

a) b)

c) d)

Figure 3. 12 – Slip bands: a,c) alloy Cu 0.0; b,d) alloy Cu 1.5

The hardness of eutectic Si is 11.13 ± 0.1 GPa, while it is 6.51 ± 1.5 GPa and 5.77 ± 0.7 GPa for Q and θ phases, respectively, as reported in the literature [7]. The primary α-Al hardness varies in the range from 0.63 to 0.74 GPa (converted from $HV_{0.001}$ hardness values measured at the centre of the dendrites) with increasing Cu content and, in each alloy, it remains the preferred choice for the crack propagation, given the higher hardness of secondary phases.

Figure 3. 13 reports the DIC image analysis of the investigated alloys and the crack micrographs of the subsequent cycles. The DIC software in some areas has difficulties in recognising the pattern. Nevertheless, it highlights the region where the crack will propagate in the following cycles. In alloy Cu 0.0, an almost horizontal area suffers from the maximum Von Mises equivalent strain (bright green, that corresponds to ~ 0.075 strain) but the crack, in this case, follows a different path. It develops a vertical way and moves to other grains. The DIC analysis of alloy Cu 1.5 underlines an area with high strain concentration that is not yet interested by a crack, but it will suddenly propagate within a few cycles and finally lead to failure. The final crack thus nucleated under the surface and emerged fully developed. In alloy Cu 3.0 a rapid failure occurs without any previously detectable deformation in the DIC image, and the SEM image of the crack path is not available. The primary matrix results strengthened but also becomes brittle with 1 ÷ 1.4 wt. % of Cu measured via WDS analysis. This behaviour mirrors what observed in tensile tests, with a sudden UTS drop despite the increase in YS.

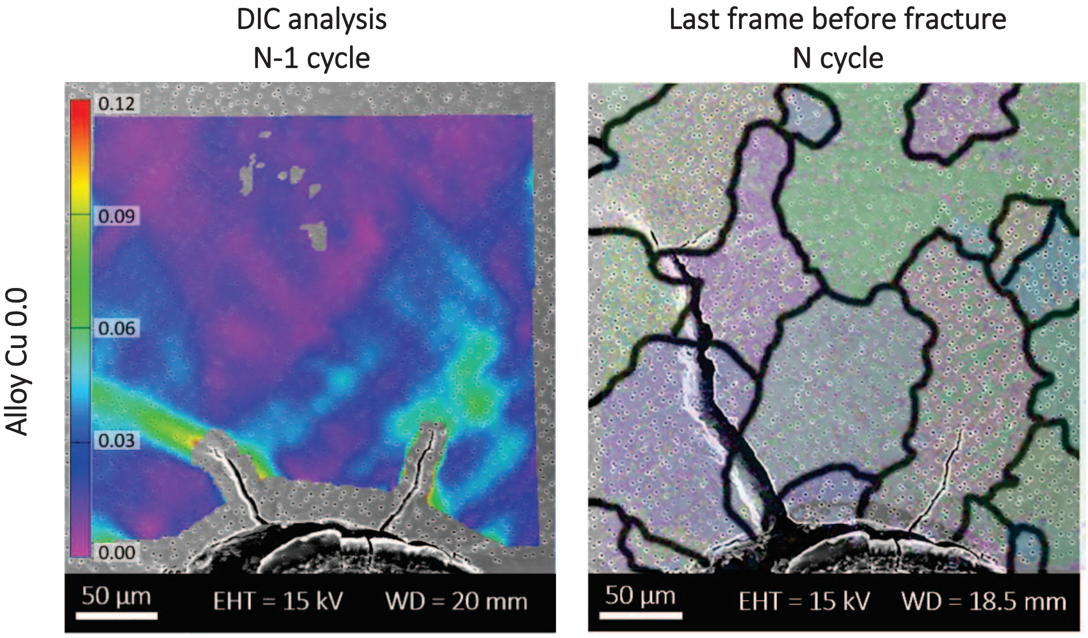

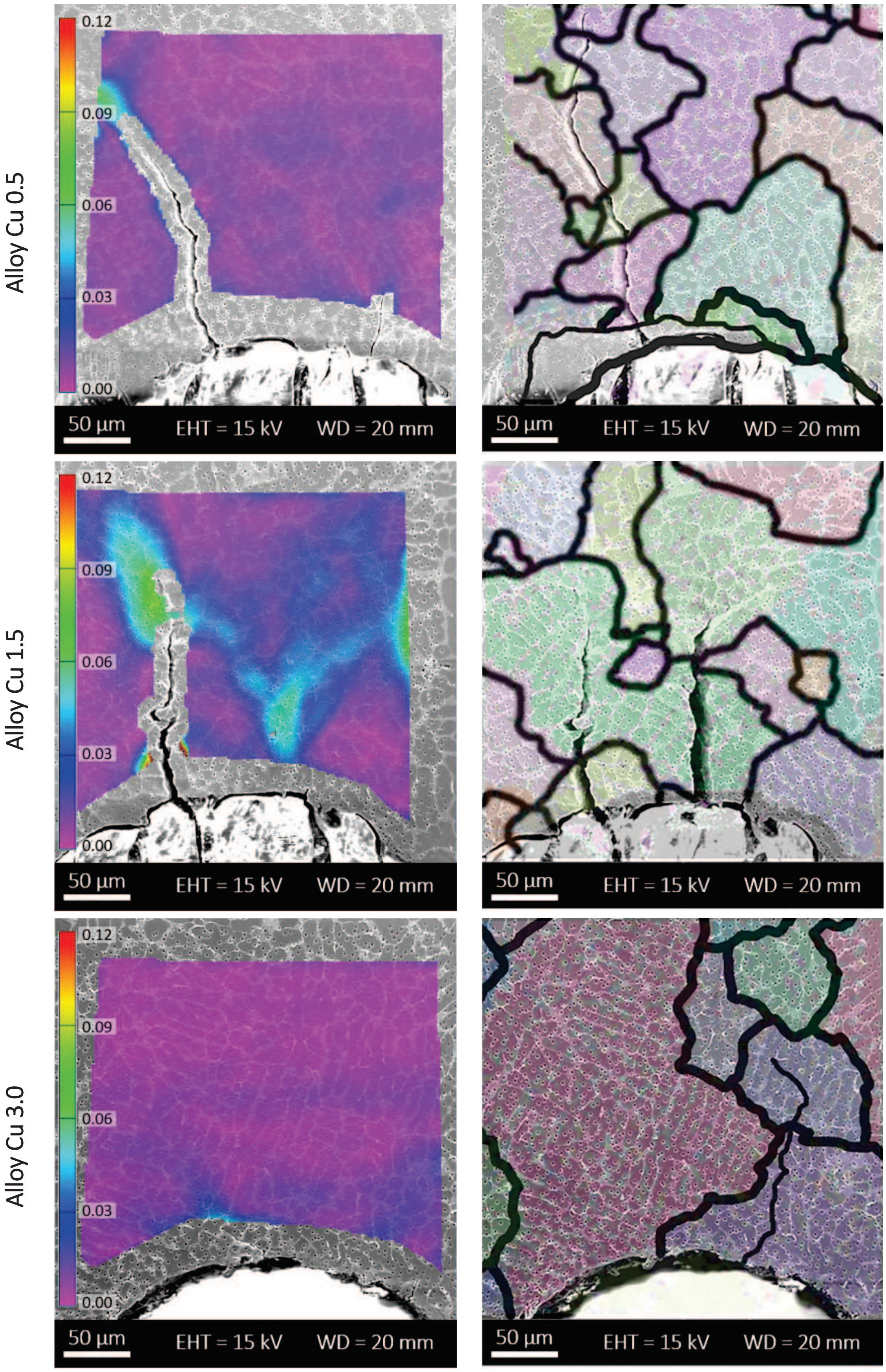

Figure 3. 13 – DIC images of the N-1 cycle and micrograph at the N cycle, which is the last frame before the final fracture. Colour bar is related to the Von Mises equivalent strain

The drawbacks of the present study regard the DIC software, that does not follow the speckles in the area around the crack path, even when not deformed. Probably this method for pattern generation is not suitable for easily deformed materials, as the pattern itself deforms during tests and DIC software does not recognise speckles after deformation. Since the microstructural features are in grayscale with not evident contrast as in a cast iron [4], it is difficult for the software to follow speckles from one frame to the next one. Besides, the appearance of FIB milled pattern strongly depends on the grain orientation, and it can result without enough contrast for DIC software.

It is fundamental to keep in mind that the present study is a two-dimensional investigation of a 3D phenomenon, even if the thickness of the specimen is limited. Fracture surface analysis after complete failure can partially overcome this limit, but it remains challenging to define crack nucleation sites. The investigation of fracture surfaces in alloy Cu 0.0 (Figure 3. 14a) reveals the starting point of the fatigue crack at the notch. The stable propagation region has a radius of 200 μm and the surface appears smooth with some linear features that can be identified as propagation rivers, converging in the initiation site. The remaining crack surface presents an irregular surface and corresponds to the final static fracture. Dendrite arms appear on this rugged area of the surface. Similar observations come from surfaces of alloys Cu 0.5 (Figure 3. 14b) and Cu 1.5 (Figure 3. 14c), although the initiation point of the crack becomes less evident than the Cu-free alloy.

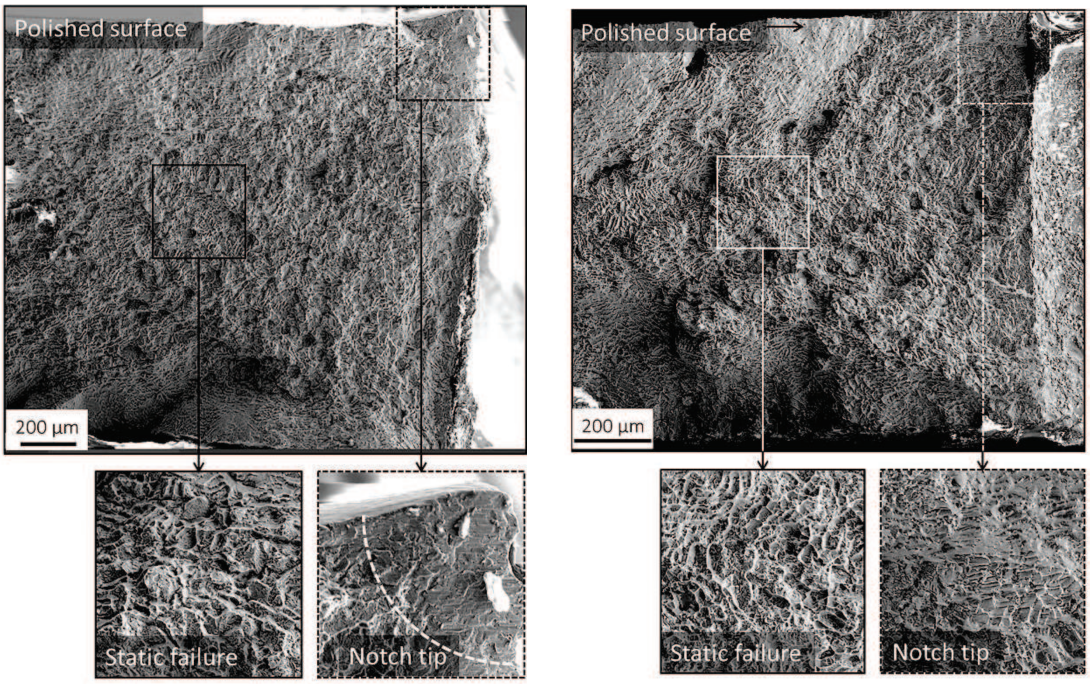

a) b)

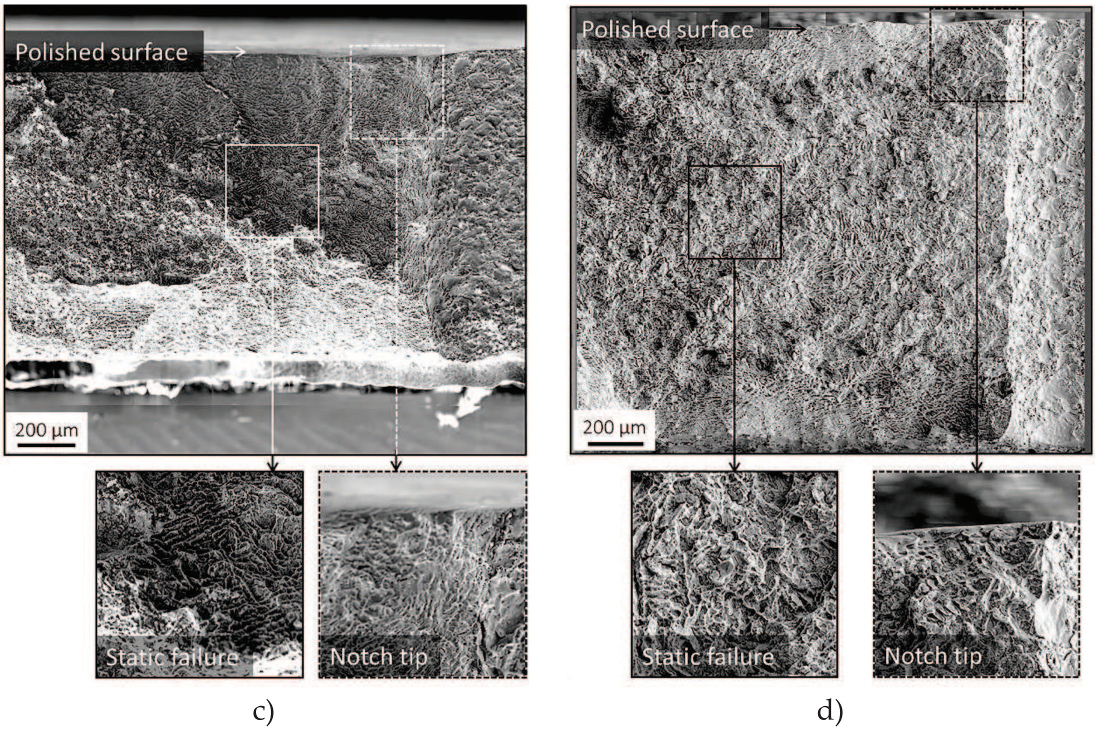

c) d)

Figure 3. 14 – Fatigue fracture surfaces: a) alloy Cu 0.0; b) alloy Cu 0.5; c) alloy Cu 1.5; d) alloy Cu 3.0

A clear distinction with the rest of the surface, related to the static failure, is still visible as the Cu content increases up to 1.5 wt.%. It appears that the crack nucleated from the notch in a region close to the polished surface, and no other evident starting point are visible on the fracture surface. On the other hand, in alloy Cu 3.0 (Figure 3. 14d), the same distinction of the initiation and propagation areas cannot be observed. Evident initiation point and stable propagation area are not present, and the entire section presents the irregular surface related to the static failure. Similarly to what previously observed, dendrite arms emerge clearly on the surface. These observations mirror the fatigue behaviour observed for the alloys, in particular the stable propagation of the fatigue crack present in all the alloys except for the one with the highest Cu content, that suffered a sudden static failure.

3.4 CONCLUSION AND FUTURE DEVELOPMENTS

The present study describes how specific microstructural features, related to the addition of Cu in the AlSi7Mg alloy, influence the fatigue crack nucleation and propagation. *In-situ* cyclic tests correlated to DIC analysis highlight that the main effect related to Cu is the α-Al matrix strengthening because the reinforcement due to the presence of Cu atoms significantly changes its response to deformation. The fatigue crack path remains trans-granular and trans-dendritic for a Cu content that raises to 3.0 wt.%. The primary α-Al matrix becomes less prone to deformation, and stable propagation of the crack turns into almost static failure. The two-dimensional DIC analysis could not detect any previous strain before failure on the surface of the alloy Cu 3.0 samples. Since the Cu-based compounds do not influence the crack path and propagation, the different behaviour of Alloy Cu 3.0 can only depend on the Cu atoms retained in the primary matrix. Either Cu contributes to strengthening via solid solution or coherent and semi-coherent precipitates, its effect on the α-Al matrix leads to a different response during cyclic stress. A more detailed investigation about the arrangement of Cu atoms in the primary matrix will give a definite answer.

A behaviour similar to the one observed for alloy Cu 3.0 could occur with alloy Cu 1.5 after heat treatment, which determines the dissolution of Cu phases and the enrichment in Cu of the primary matrix. Tailored heat treatments on alloy Cu 0.5 can lead to an optimised microstructure, with a strengthened but yet not brittle primary α-Al matrix and a limited amount of well-dispersed Cu phases. Besides, the heat treatment also dissolved Si particles and Mg compounds, and it can contribute to reinforcing the microstructure. Further investigations of heat-treated alloys will clarify the present assumptions.

The study of the deformation around sub-grain microstructural features, such as Si particles and Cu phases, requires a smaller pattern and a smaller FOV than the ones employed in this research. As a time-saving alternative, Si particles themselves can act as speckles of a random pattern, given enough contrast with the primary matrix. If the pattern results validated, this procedure can be a useful alternative in materials that present a similar built-in pattern and that suffer from deformation during FIB milling.

REFERENCES

[1] D. A. Lados and D. Apelian, *Fatigue crack growth characteristics in cast Al-Si-Mg alloys Part I. Effect of processing conditions and microstructure*, Mater. Sci. Eng. A, vol. **385**, no. 1–2, pp. 200–211, 2004

[2] D. A. Lados, D. Apelian, and J. F. Major, *Fatigue Crack Growth Mechanisms at the Microstructure Scale in Al-Si-Mg Cast Alloys : Mechanisms in Regions II and III*, Metall. Mater. Trans. A, vol. **37**, no. August, pp. 2405–2418, 2006

[3] A. G. Spangenberger, X. Chen, and D. A. Lados, *Processing Parameter Control of Lifetime-Limiting Failure Mechanisms in Al-Si Cast Alloys at Room and Elevated Temperatures*, Metall. Mater. Trans. B Process Metall. Mater. Process. Sci., vol. **49B**, no. October 2018, pp. 2133–2144, 2018

[4] K. A. Kasvayee, E. Ghassemali, K. Salomonsson, S. Sujakhu, S. Castagne, and A. E. W. Jarfors, *Microstructural strain mapping during in-situ cyclic testing of ductile iron*, Mater. Charact., vol. **140**, pp. 333–339, 2018

[5] E. Sjölander, *Heat treatment of Al-Si-Cu-Mg casting alloys*, Jönköping University, 2011

[6] A. M. Samuel and F. H. Samuel, *Effect of alloying elements and dendrite arm spacing on the microstructure and hardness of an Al-Si-Cu-Mg-Fe-Mn (380) aluminium die-casting alloy*, J. Mater. Sci., vol. **30**, no. 7, pp. 1698–1708, 1995

[7] E. Sjölander and S. Seifeddine, *Optimization of Solution Treatment of Cast Al-7Si-0.3Mg and Al-8Si-3Cu-0.5Mg Alloys*, Metall. Mater. Trans. A, vol. **45A**, pp. 1916–1927, 2013

[8] C. H. Caceres, M. B. Djurdjevic, T. J. Stockwell, and J. H. Sokolowski, *The effect of Cu content on the level of microporosity in Al-Si-Cu-Mg casting alloys*, Scr. Mater., vol. **40**, no. 5, pp. 631–637, 1999

[9] G. Heiberg, K. Nogita, A. L. Dons, A. K. Dahle, and L. Arnberg, *Effect of magnesium, iron and copper on eutectic solidification of hypoeutectic aluminum-silicon alloys*, AFS Trans., pp. 347–358, 2002

[10] M. Zeren, E. Karakulak, and S. Gümüs, *Influence of Cu addition on microstructure and hardness of near-eutectic Al-Si-xCu-alloys*, Trans. Nonferrous Met. Soc. China, vol. **21**, pp. 1698–1702, 2011

[11] A. Darlapudi, S. D. Mcdonald, and D. H. Stjohn, *The influence of ternary Cu*

additions on the nucleation of eutectic grains in a hypoeutectic Al-10 wt .% Si alloy, J. Alloys Compd., vol. **646**, pp. 699–705, 2015

[12] R. Taghiabadi, A. Fayegh, A. Pakbin, M. Nazari, and M. H. Ghoncheh, *Quality index and hot tearing susceptibility of Al–7Si–0.35Mg–xCu alloys*, Trans. Nonferrous Met. Soc. China, vol. **28**, pp. 1275–1286, 2018

[13] G. A. Edwards, G. K. Sigworth, C. H. Caceres, D. H. StJohn, and J. Barresi, *Microporosity formation in Al-Si-Cu-Mg casting alloys*, AFS Trans., vol. **97**, no. 59, pp. 809–818, 1997

[14] F. H. Samuel, A. M. Samuel, and H. W. Doty, *Factors controlling the type and morphology of Cu-containing phases in 319 Al alloy*, AFS Trans., vol. **96**, no. 30, pp. 893–901, 1996

[15] P. Ouellet, F. H. Samuel, D. Gloriat, and S. Valtierrat, *Effect of Mg content on the dimensional stability and tensile properties of heat treated Al-Si-Cu (319) type alloys*, Int. J. Cast Met. Res., vol. **10**, pp. 67–78, 1997

[16] M. Djurdjevic, T. Stockwell, and J. Sokolowski, *The effect of strontium on the microstructure of the aluminium-silicon and aluminium-copper eutectics in the 319 aluminium alloy*, Int. J. Cast Met. Res., vol. **12**, pp. 67–73, 1999

[17] N. Tenekedjiev, H. Mulazimoglu, B. Closset, and J. Gruzleski, *Alloy 355*, in *Microstructures and thermal analysis of strontium-treated aluminum-silicon alloys*, Des Plaines, IL: American Foundrymen's Society, 1995, pp. 32–52

[18] S. Seifeddine, E. Sjölander, and T. Bogdanoff, *On the Role of Copper and Cooling Rates on the Microstructure, Defect Formations and Mechanical Properties of Al-Si-Mg Alloys*, Mater. Sci. Appl., vol. **4**, pp. 171–178, 2013

[19] D. A. Lados, D. Apelian, and J. F. Major, *Fatigue Crack Growth Mechanisms at the Microstructure Scale in Al-Si-Mg Cast Alloys : Mechanisms in Regions II and III*, Metall. Mater. Trans. A, vol. **37**, no. August, pp. 2405–2418, 2006

CHAPTER 4

SIDE PROJECT – Ni ADDITION

The present chapter deals with the final part of a collaboration with the Norwegian University of Science and Technology in Trondheim, Norway. The project regarded the evaluation of tensile and impact properties of Ni-added AlSi7Mg alloys both at high and room-temperature. The results here presented are about room-temperature mechanical properties.

4.1 LITERATURE SURVEY

Since mechanical properties of Al alloys rapidly decrease when temperature increases, the addition of transition elements, such as Cu and Ni, is a crucial aspect for applications that require improved high-temperature resistance [1]–[4]. Differently from Cu, Ni has minimal solubility in Al (0.05 wt.% at 640 °C and decreases to 0.003 wt.% at 527 °C) and thus it is mainly found in intermetallic compounds with Al, Cu or Fe. The presence of Ni in eutectic and hypoeutectic Al-Si alloys leads to the formation of thermally stable ε-Al_3Ni and T-Al_9FeNi intermetallic compounds [5]–[7]. In particular, the latter one precipitates through a peritectic reaction from the β-Al_5FeSi phase [8]. A Ni/Fe ratio of approximately 2 is considered the threshold, above which all the Fe present in the alloy forms the T-phase, and the formation of β-phase is suppressed [9], [10]. These Ni-based aluminides and binary Al-Si eutectic are observed to nucleate in overlapping temperature ranges [11]. These characteristics lead to the formation of a three-dimensional (3D) interconnected network made of eutectic Si and Ni-based intermetallic phases. The interconnected structure acts as a rigid reinforcement for the α-Al matrix since both eutectic Si and Ni aluminides have higher strength and higher Young's modulus than primary α-Al [12]. Besides, the presence of Ni-bearing compounds has a poisoning effect on the spheroidization of Si eutectic particles during solution heat treatment. According to Asghar et al. [6], the interface between eutectic Si and Ni-based compounds remains after solution heat treatment, and the reason for this phenomenon concerns the interfacial energy between aluminides and Si. This interfacial energy is more favourable than the one between primary α-Al and Si, and thus stabilises the interconnected structures of Si and Ni aluminides. These aluminides maintain the interconnection of the 3D network during eutectic Si spheroidization acting as linking elements for isolated Si particles. Therefore, the 3D network provides good high-temperature strength to the alloy and makes it suitable for applications that require high-temperature performances [6], [13]. In previous studies, several authors evaluated the effect of Ni additions varying from 0.5 wt.% to 4 wt.% [1], [5], [13]–[16] on near-eutectic Al-Si10 and Al-Si12 cast alloys, widely employed for cylinder heads and pistons. High-temperature compression strength is a crucial requirement for piston alloys since these components have to withstand severe compression stresses as well as temperatures up to 400 °C during their service life [1], [5].

Additionally, some authors investigated the influence of Ni on room-temperature mechanical properties [16], [17]. Yang et al. [16] reported that the evolution of Ni-rich compounds has a beneficial effect on the room-temperature mechanical properties of an Al-Si piston alloy; moreover, the elevated temperature tensile strength was observed to increase by about 19.7 %. Yang et al. [17] found that the addition of Ni to an Al-Mg-Si-Mn alloy resulted in a slight increase in both room-temperature YS and UTS.

4.2 AIM AND PURPOSE OF THE WORK

Hypoeutectic Al-Si alloys, such as the A356 alloy, are the most used Al foundry alloys in several automotive applications, which require both room and high-temperature services. Few authors [3], [18]–[20] investigated the influence of Ni on tensile mechanical properties of hypoeutectic Al-Si alloys at both room and high-temperature. These works report contradictory findings, and the actual impact of Ni on the mechanical properties is yet to be determined. Stadler et al. [18] investigated the effect of different Ni amounts (0.5, 1.0, and 1.5 wt.%) on the high-temperature mechanical properties of T4 heat-treated specimens. YS, UTS, and percentage elongation were found to increase up to 1.0 wt.% of Ni. No further increase in mechanical properties occurs at higher Ni concentrations. Casari et al. [3] studied the effect of different Ni concentrations (0.5, 1.0, and 2.0 wt.%) on high-temperature mechanical properties by comparison of as-cast and T6 heat-treated specimens. The authors reported that Ni contents over 0.5 wt.% determine a significant reduction of both YS and UTS in heat-treated alloys. Fang et al. [19] reported that the Ni and Sr-containing A380 alloy exhibits a significant improvement in tensile properties, specifically UTS and YS. Garcia-Hinojosa et al. [20] examined the effect of Ni additions

(0.5 and 1.0 wt.%) on room-temperature mechanical properties of as-cast A356 alloys, both unmodified and modified with Sr. In both alloys, Ni additions did not improve the mechanical properties compared to the base A356 alloy because of the presence of massive ε-Al_3Ni conglomerates that weaken the alloy structural characteristics.

Additionally, very few works focus on the effect of Ni additions on room-temperature mechanical properties of hypoeutectic Al-Si alloys in both as-cast and T6 conditions. This research aims to explore the evolution of microstructure and room-temperature performances of Ni-added AlSi7Mg alloys. A comprehensive investigation revealed the role played by Ni-based intermetallic compounds on the room-temperature tensile properties in as-cast and T6 heat-treated conditions. Microstructural investigations are useful to describe possible variations of microstructural features with increased Ni additions. Fractographic observations deepen the role of Ni aluminides on the fracture behaviour of the examined alloys.

4.3 MATERIALS AND EXPERIMENTAL PROCEDURE

4.3.1 Melt preparation

The melt preparation was carried out at the beginning of the collaboration project by Dr Casari and Professor Di Sabatino at the NTNU in Trondheim, Norway. Details are reported in previous works [3], [21]. Samples from three different melts were taken and analysed by glow discharge OES, and Table 4.1 reports the chemical composition of the alloys. Except for the Ni contents, the concentration of each alloying element complies with the UNI EN 1706:2010 specification for AlSi7Mg alloys.

Table 4. 1 – Chemical composition of the alloys investigated for Ni additions [wt.%]

Alloy name	Si	Fe	Mg	Ni	Al
Ni 0.5	7.00	0.09	0.21	0.48	bal.
Ni 1.0	6.81	0.08	0.28	0.92	bal.
Ni 2.0	7.31	0.09	0.20	1.90	bal.

Cooling curves were recorded for each alloy to assess the effect of Ni on solidification (Figure 4. 1a-c). The first derivative of the regions before liquidus and after solidus was well-fitted ($R^2 > 0.9887$) by a two-term exponential baseline, that enabled to calculate the evolution of the solid fraction over time.

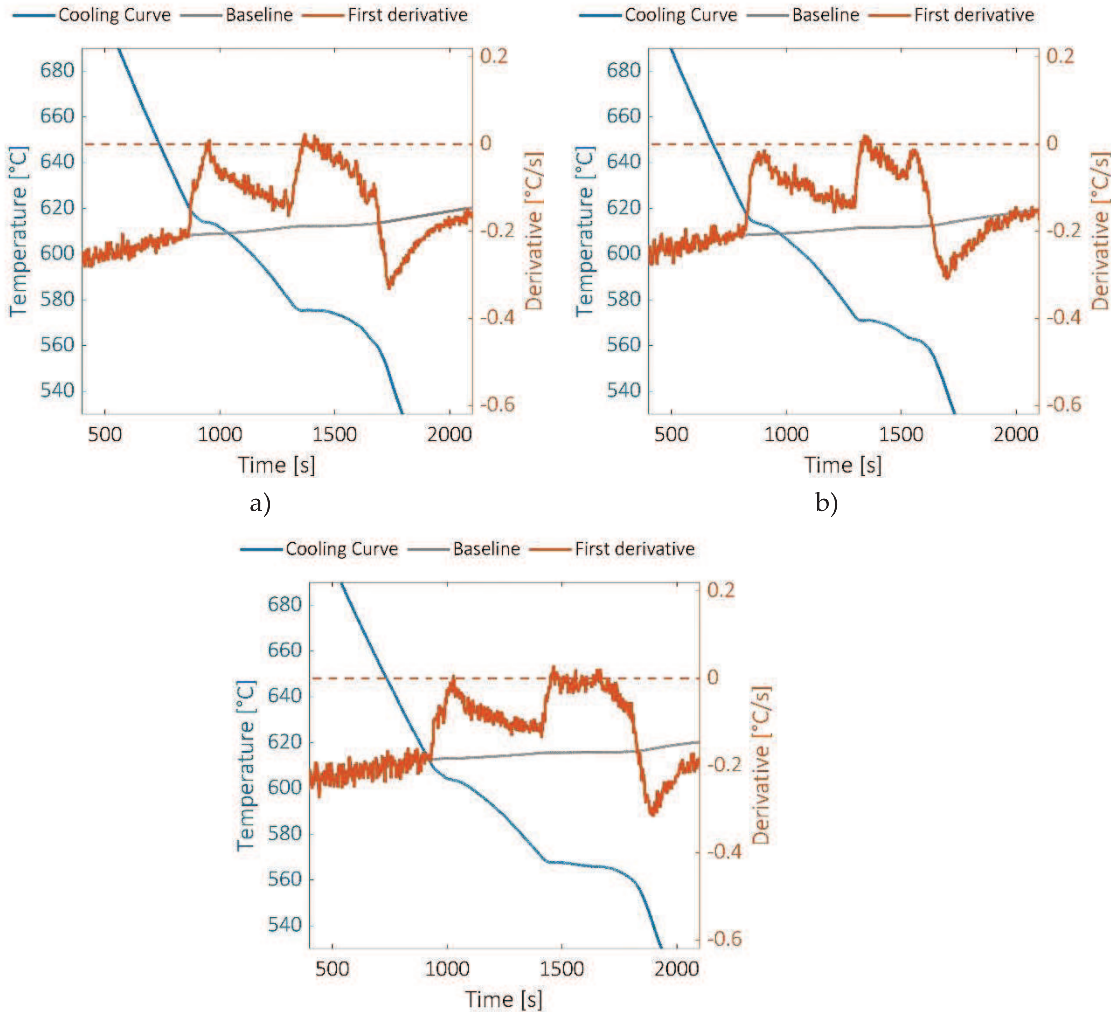

a)

b)

c)

Figure 4. 1 – Cooling curve, first derivative and baseline: a) alloy Ni 0.5; b) alloy Ni 1.0; c) alloy Ni 2.0

The T6 heat treatment involved a two-step solution treatment at 520 °C for 2 hours and then at 540 °C for 2 hours, followed by quench in water at 20 °C and final ageing at 160 °C for 6 hours.

4.3.2 Mechanical tests

Tensile specimens with a round cross-section (8.5 mm diameter and 40 mm gauge length) were machined and subsequently tested at room temperature, according to the UNI EN ISO 6892-1:2016 standard, with an MTS 810 servo-hydraulic testing machine equipped with a 250 kN load cell. The crosshead speed was of $16.7 \cdot 10^{-3}$ mm/s. Charpy impact V-notch specimens were machined accordingly to the ISO 148-1 standard. For each experimental condition, ten specimens were tested according to the ASTM E-23 standard using a CEAST instrumented pendulum with available energy of 50 J. The data were collected using a DAS 64K analyser. The instrumented pendulum records the load-displacement curve (Figure 4. 2) during the tests. The analysis of these data reports the peak force and the total absorbed energy calculated as integral of the curve during the entire test. The latter consists of the crack initiation energy, the integral of the curve from the beginning to the maximum-load point, and the crack propagation energy, the integral from the maximum-load point to the end.

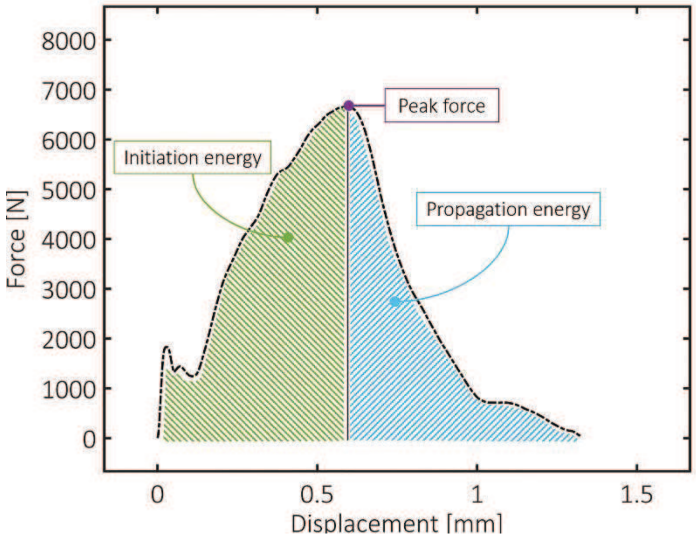

Figure 4. 2 – Impact parameters obtained from the load-displacement curve

To test the α-Al matrix, Vickers microhardness tests were performed with a load of 0.1 N and a dwell time of 15 s, following the UNI EN ISO 6507:2006 standard.

4.3.3 Microstructural evaluation

Samples for microstructural investigations were cut from the tensile specimens, embedded in phenolic resin and prepared using standard grinding and polishing procedures. Microstructure analyses were performed using an OM equipped with polarised light. The 0.5 mL HF + 100 mL H2O etchant enhances the contrast between the Mg-based intermetallic and the Ni-based phases. Quantitative image analysis was conducted by the BS ISO 13322-1:2014 on the same measurement field for each sample. Twenty frames of area ~10,600 μm^2 were analysed at a magnification of 1000× for a total investigated area of ~212,000 μm^2. Equivalent diameter (ED = $(4\cdot area/\pi)^{1/2}$) and shape factor (SF = $length^2/4\pi\cdot area$) are the geometric parameters investigated for this study, and the Anderson-Darling test permits to evaluate the goodness of the statistical distribution fittings.

The different phases were also investigated and identified with the SEM equipped with EDS microanalysis. Deep-etched specimens were investigated to give a qualitative evaluation of the 3D structure of eutectic Si and Ni-containing compounds. The deep-etch lasts in total three minutes, alternatively for 20 seconds in 10 % NaOH and 5 % HCl water solutions, respectively.

4.4 RESULTS

4.4.1 Microstructural investigations

Figure 4. 3 depicts representative SEM micrographs of the alloys Ni 0.5, Ni 1.0 and Ni 2.0 in the as-cast and T6 heat-treated conditions. The typical microstructure of an AlSi7Mg alloy consists of primary α-Al dendrites and eutectic Si particles in the interdendritic regions. The number and size of Ni-based intermetallic compounds depend on the alloy chemical composition. These intermetallic compounds present primarily with a Chinese-script morphology and occasionally a blocky polyhedral morphology. These intermetallic compounds are ε-Al$_3$Ni and T-Al$_9$FeNi, as labelled in the micrographs of Figure 4. 3a,c,e. Fe-based compounds as β-Al$_5$FeSi are not present in the investigated alloys because the Ni/Fe ratio is always higher than two. It suggests that the total amount of Fe is bound to Ni in the T-Al$_9$FeNi phase, as reported by Farkoosh *et al.* [13]. The T6 heat treatment causes some changes in the microstructure: eutectic Si particles, with a needle-like morphology in the as-cast microstructure, become fine and rounded after T6 heat treatment. Figure 4. 3b,d,f illustrate that a variation in the shape of particles also interests the Ni-based intermetallic phases, that show rounded and smoothed edges.

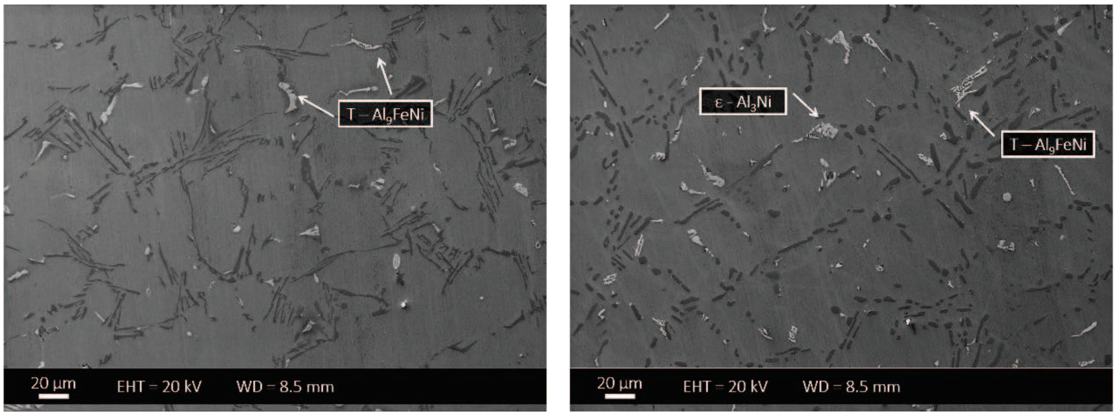

a) b)

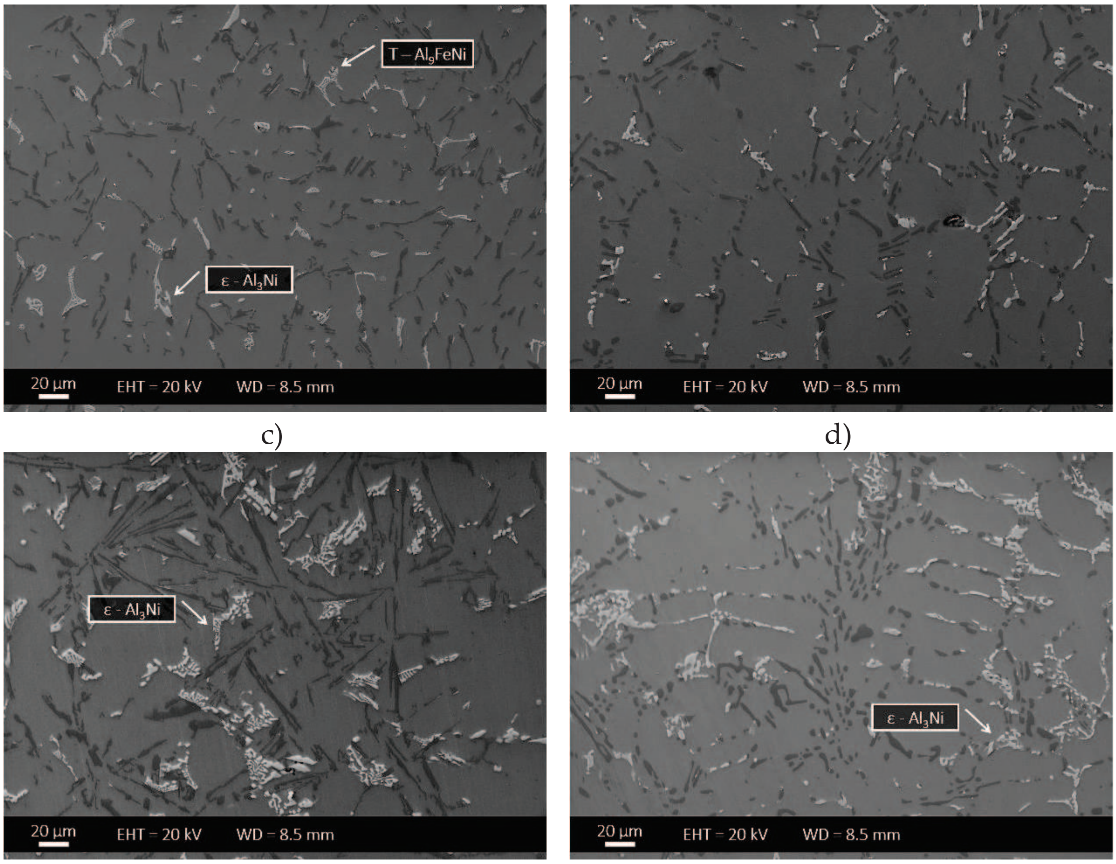

c) d)

e) f)

Figure 4. 3 – SEM micrographs of the alloys: a) Ni 0.5, as-cast; b) Ni 0.5, T6 heat-treated; c) Ni 1.0, as-cast; d) Ni 1.0, T6 heat-treated; e) Ni 2.0, as-cast; f) Ni 2.0, T6 heat-treated

Figure 4. 4 shows some Ni-based intermetallic compounds found in the as-cast alloy Ni 0.5 (Figure 4. 4a) and the heat-treated alloy Ni 1.0. The EDS spectra of Figure 4. 4c-d confirmed the presence of T-Al_9FeNi and ε-Al_3Ni respectively, given the atomic content of the elements in Table 4. 2. The T phase presents a Ni content of 10.2 ÷ 16.6 at.% and Fe in the 2.2 ÷ 3.9 at.% range. The ε phase contains 18.1 ÷ 28.2 at.% Ni and the Fe content is lower than 2.0 at.%. The EDS measurements agree with previous research [22].

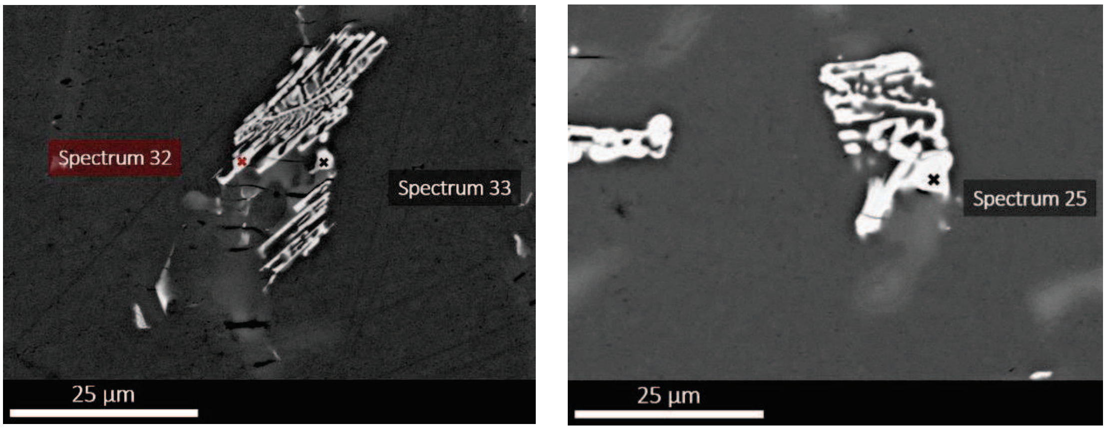

a) b)

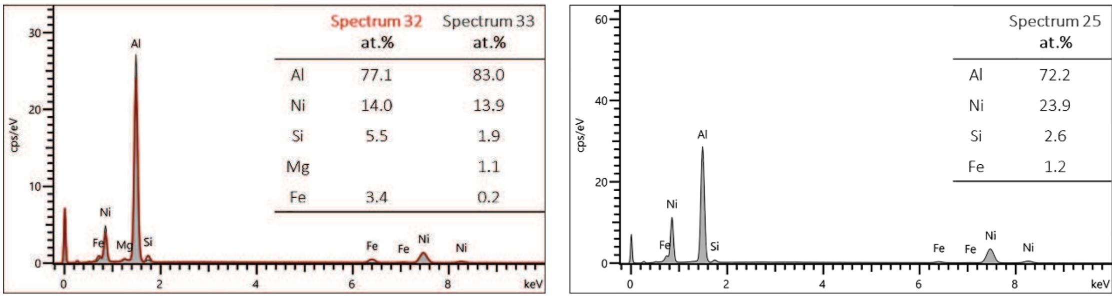

	Spectrum 32 at.%	Spectrum 33 at.%
Al	77.1	83.0
Ni	14.0	13.9
Si	5.5	1.9
Mg		1.1
Fe	3.4	0.2

	Spectrum 25 at.%
Al	72.2
Ni	23.9
Si	2.6
Fe	1.2

c) d)

Figure 4. 4 – SEM micrographs of Ni-based intermetallic compounds a) alloy Ni 0.5, as-cast; b) alloy Ni 1.0, heat-treated. EDS spectra: c) spectra related to a); d) spectrum related to b)

The Ni-based compounds in alloys Ni 1.0 and Ni 2.0 present a Fe content lower than 2.0 at.% in most cases. The high amount of Ni seems to promote the precipitation of compounds rich in Ni that also contain small amounts of Fe, and thus the T phase was not distinct from the ε-Al_3Ni compounds.

Table 4. 2 – Composition ranges [at.%] of Ni-based compounds measured by EDS

Phase	Al	Si	Fe	Ni
ε-Al_3Ni	79.8 - 89.0	1.3 - 2.0	< 2.0	18.1 - 28.2
T-Al_9FeNi	73.9 - 83.5	2.9 - 5.7	2.2 - 3.9	10.2 - 16.6

The Scheil simulation in Thermo-Calc Software ® predicts the formation of the ε phase and different Fe-based compounds ($Al_9Fe_2Si_2$ and $Al_{18}Fe_2Mg_7Si_{10}$) but does not assess the presence of the T phase in the three alloys (Figure 4. 5a,c,e). Since it is not related to a limitation of the database TCAL5 provided by the software, the lack of T-phase can be explained with the limited amount of Fe present in the alloys. According to the Scheil simulation, Fe is involved entirely in $Al_9Fe_2Si_2$ and $Al_{18}Fe_2Mg_7Si_{10}$ and not in Ni-based phases.

Similarly, the analysis of cooling curves depicted in Figure 4. 1 does not highlight nucleation peaks that can be related to the precipitation of T-Al_9FeNi with the investigated Ni contents. Therefore, the solid fraction of the T phase cannot be calculated (Figure 4. 5b,c,f). The reason once again is probably related to the limited amount of these compounds, because a small fraction of T-Al_9FeNi does not lead to detectable solidification peaks and the equilibrium simulation does not assess it.

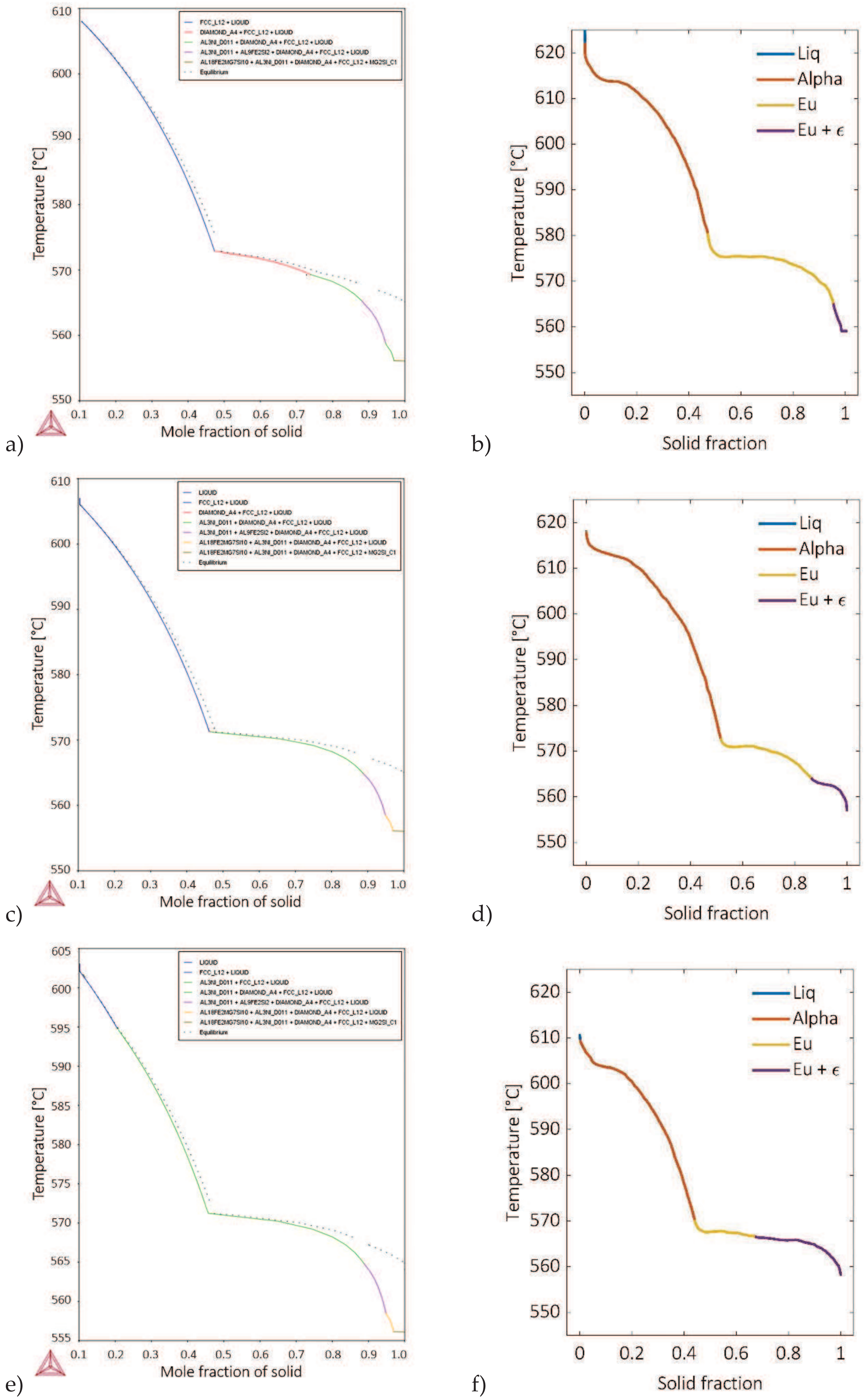

a) b) c) d) e) f)

Figure 4. 5 – Temperature v. solid fraction. Scheil simulations: a) alloy Ni 0.5, c) alloy Ni 1.0, e) alloy Ni 2.0; thermal analysis: b) alloy Ni 0.5, d) alloy Ni 1.0, f) alloy Ni 2.0

The Ni-based compounds show irregular shapes, and they are connected one to another by eutectic Si plate-like particles, forming a three-dimensional network. This interconnection becomes evident after deep etching of the samples, as depicted in Figure 4. 6 for alloy Ni 2.0. In the as-cast condition (Figure 4. 6a), the Si particles and the Ni-based compounds show sharp edges, and the network is continuous. Figure 4. 6b highlights that heat treatment has a significant influence on the continuity of the secondary phases. Both Si particles and Ni phases present rounded edges and the partial dissolution of Si during solution heat treatment can affect the initial interconnection.

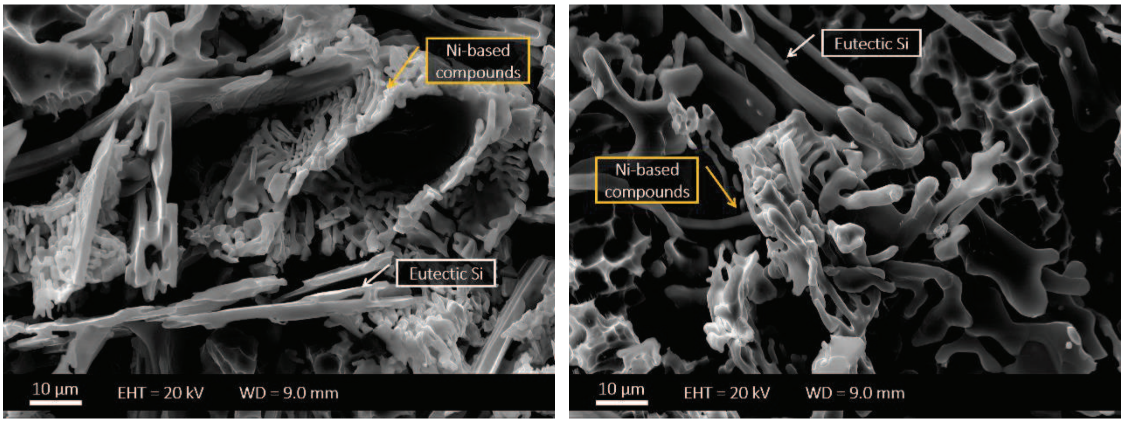

a) b)

Figure 4. 6 – SEM images of deep-etched alloy Ni 2.0: a) as-cast; b) heat-treated

To evaluate the influence of both Ni content and heat treatment on the morphology of Ni-based compounds, and thus their effect on alloy mechanical properties, ED and SF were investigated for such intermetallic compounds. ED and SF distributions were fitted with a three-parameter lognormal distribution (Figure 4. 7).

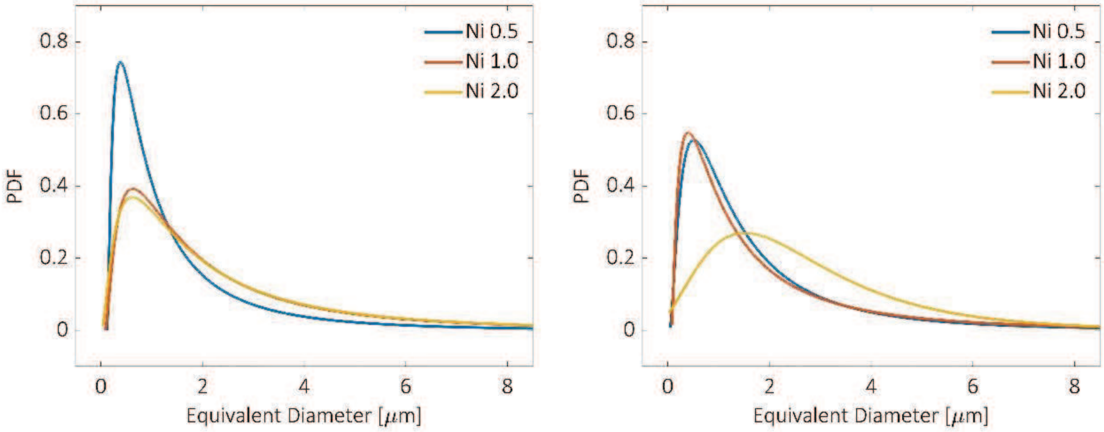

a) b)

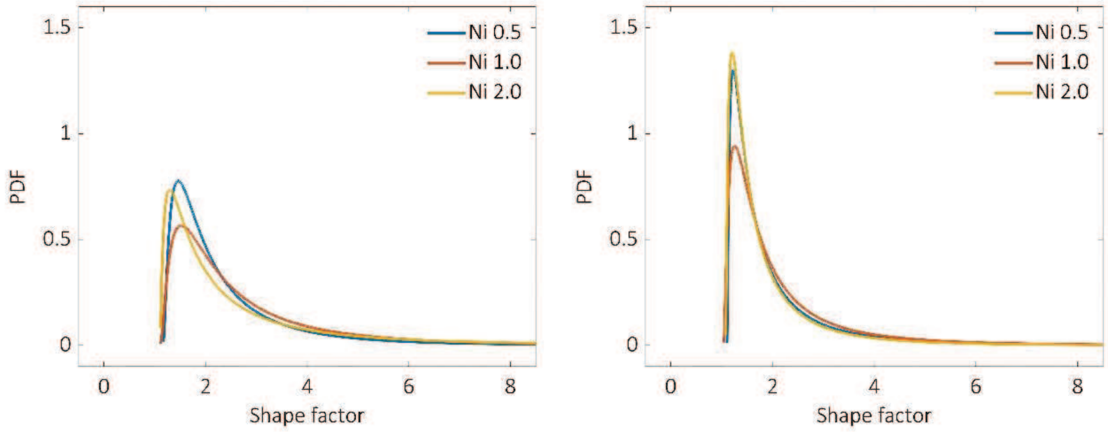

c) d)

Figure 4. 7 – Lognormal distribution of geometrical parameters of Ni-based compounds: ED, a) as-cast and b) T6 heat-treated; SF, c) as-cast and d) T6 heat treated

In the as-cast Ni 0.5 alloy (Figure 4. 7a) compounds with an ED lower than one μm are predominant. As expected, the size of Ni aluminides increases as the content of Ni increases. Particles become more homogeneous in size as ED distribution peaks decrease and right tails increase. After T6 heat treatment PDF values for ED reduce (Figure 4. 7b), meaning that the ED of Ni intermetallic compounds become more homogeneous than in the as-cast condition. The SF value approaches 1 when the particle shape is regularly round. Figure 4. 7c highlights that in as-cast alloys particles show the SF modes between 1.30 and 1.52, while after T6 heat treatment (Figure 4. 7d) the SF mode slightly decreases to an average value of 1.23. In both cases, the Ni content does not significantly influence the SF distribution, while the heat treatment decreases the SF mode values.

4.4.2 Tensile properties

Figure 4. 8 illustrates the results of tensile tests for the as-cast and the T6 heat-treated alloys. The black markers represent the results for the AlSi7Mg base alloy reported in previous work [3]. In the as-cast condition, the average value of YS increases from 74 MPa for the Ni 0.5 alloy to 83 MPa when the Ni concentration is 1.0 wt.% (Figure 4. 8a). No further statistically significant variation is found by increasing the Ni content up to 2.0 wt.%. Moreover, the UTS of the as-cast specimens does not appear to be dependent on the Ni concentration (Figure 4. 8b). On the contrary, in the T6 condition, a significant drop in mechanical properties can be observed as the Ni concentration reaches 2.0 wt.%. The mechanical properties of the heat-treated Ni 2.0 alloy are comparable with the values observed for the same alloy in the as-cast condition. Ni seems to neutralise, to some

extent, the positive effects of the T6 heat treatment. Figure 4. 8c depicts the trend of elongation with the Ni content. Surprisingly, elongation increases in comparison with the AlSi7Mg alloy. The drop of YS and UTS observed in the T6 heat-treated samples is not coupled with a significant decrease of elongation; on the contrary, it results increased by the presence of Ni.

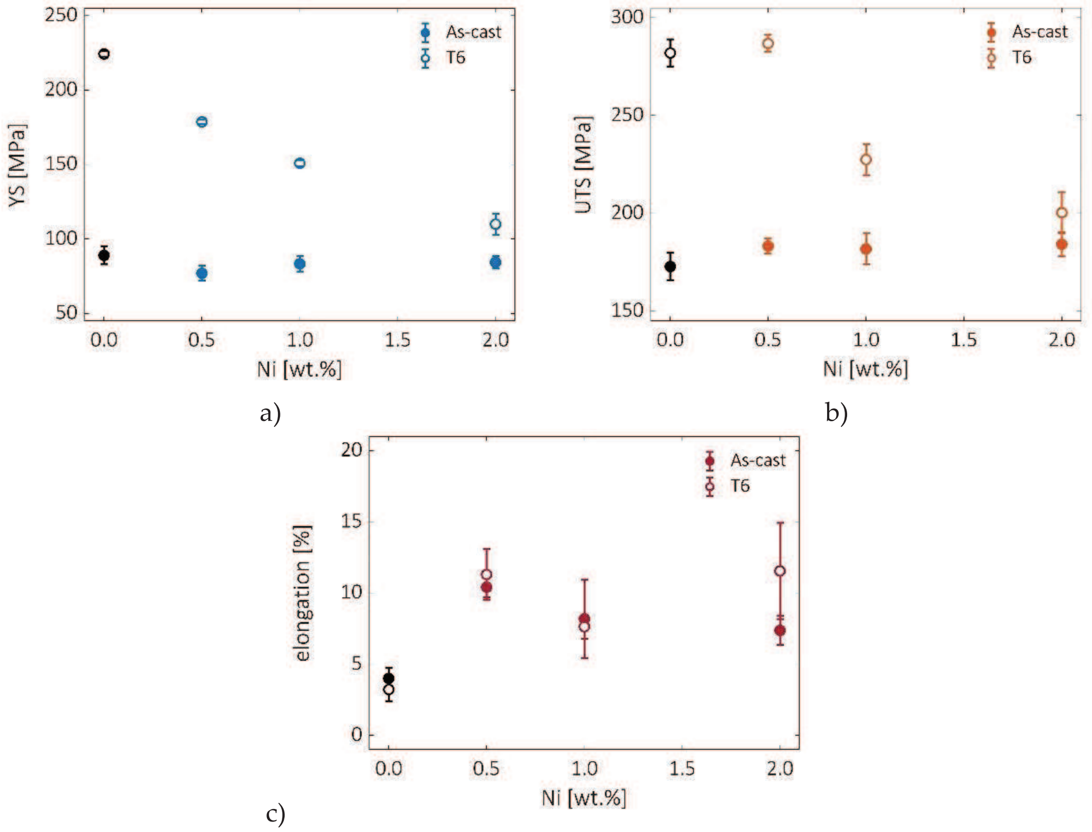

a)

b)

c)

Figure 4. 8 – Tensile properties of specimens in s-cast and T6 conditions: a) YS; b) UTS; c) elongation. Black markers refer to the AlSi7Mg alloy reported by Casari *et al.* [22]

Figure 4. 9 reports the Vickers microhardness measurements for both the as-cast and the T6 conditions as a function of Ni content. Indentations with a normal load of 0.1 N permitted to evaluate the hardness of the sole primary α-Al matrix.

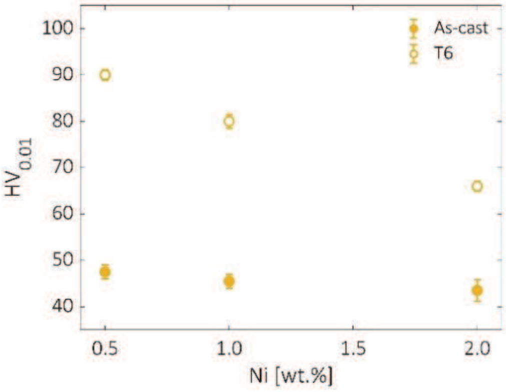

Figure 4. 9 – Vickers microhardness of as-cast and T6 heat-treated specimens

The microhardness remains constant as Ni increases for the as-cast specimens. After T6 heat treatment, as expected, microhardness values are higher. Nevertheless, a reduction of about 20 microhardness points occurs between the minimum and the maximum Ni contents.

Figure 4. 10 illustrates the fracture surfaces of the alloys containing 0.5, 1.0, and 2.0 wt.% of Ni in the as-cast and heat-treated conditions. Extended cleavage regions are evident in the as-cast samples, and Ni-based compounds are also detectable.

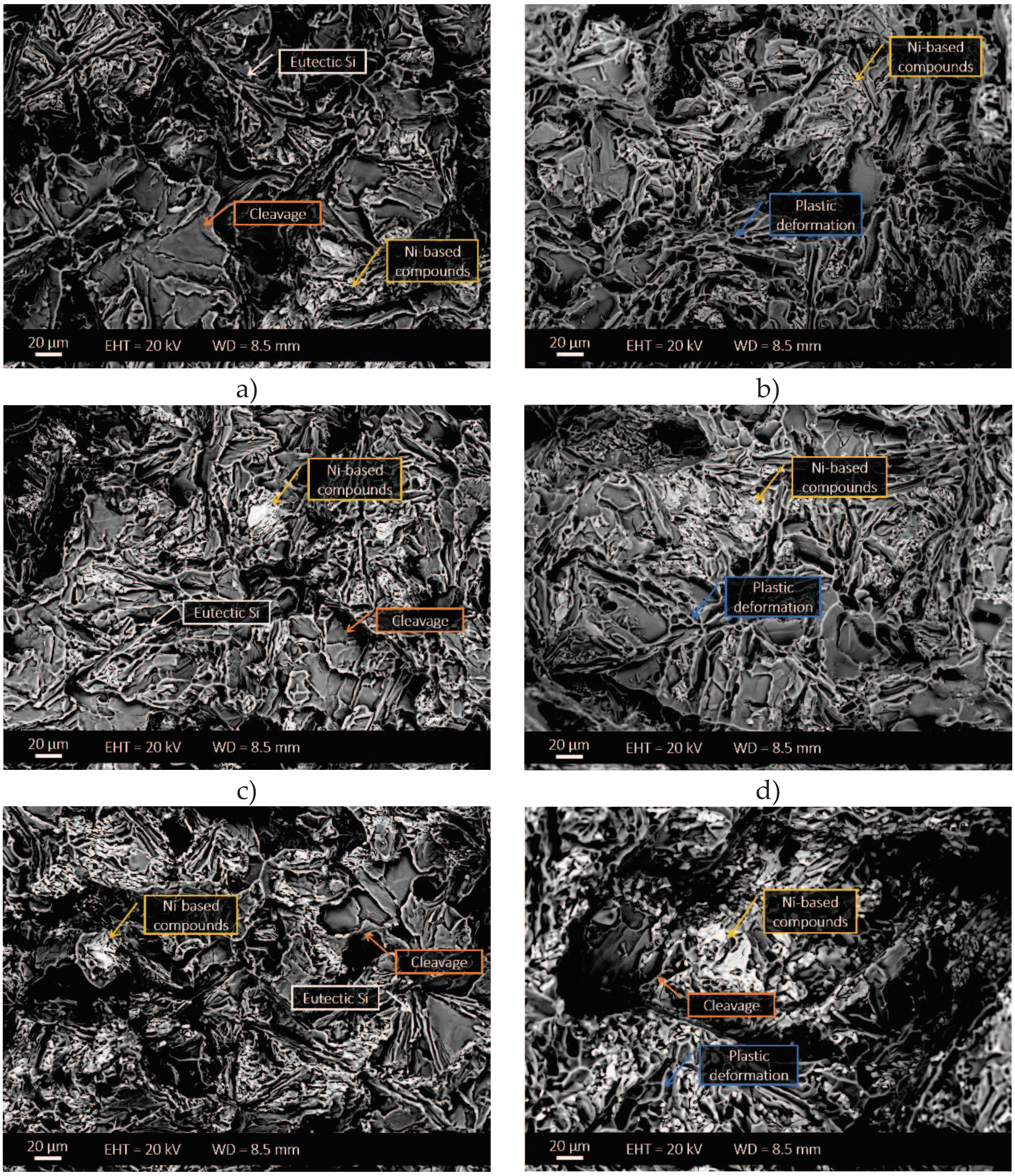

a) b) c) d) e) f)

Figure 4. 10 – Fracture surfaces of the alloys: a) Ni 0.5, as-cast; b) Ni 0.5, T6 heat treated; c) Ni 1.0, as-cast; d) Ni 1.0, T6 heat treated; e) Ni 2.0, as-cast; f) Ni 2.0, T6 heat treated

The presence of a large number of brittle phases on the fracture surface suggests that the crack originates and then propagates by rupture of such constituents. After T6 heat treatment, plastic deformation regions also occur on the fracture surface. These regions appear less frequently on the fracture surfaces with Ni concentration increasing from 0.5 to 2.0 wt.%.

4.4.3 Impact properties

Figure 4. 11 reports the peak force values of the alloys both in the as-cast and the heat-treated condition. The increasing amount of Ni in the as-cast alloys has a slight influence on the peak force. It remains stable around 2500 N within the interval 0.5 ÷ 2.0 wt.% of Ni. The same does not occur for the T6 heat-treated condition. For the alloy Ni 0.5, the heat treatment determines a significant increase of the maximum force, up to 4000 N. As the Ni content increases to 1.0 and 2.0 wt.%, its detrimental effect becomes evident. The as-cast and T6 trends of peak force are analogous to those of YS and UTS (Figure 4. 8).

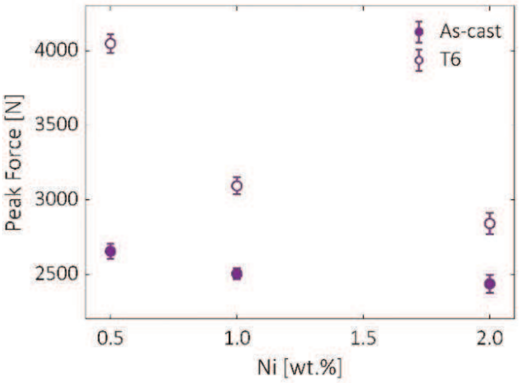

Figure 4. 11 – Peak force as a function of Ni content

Figure 4. 12 illustrates the trends of initiation (Figure 4. 12a) and propagation energy (Figure 4. 12b) with increasing Ni content. The influence of Ni on the initiation energy remains the same before and after heat treatment and determines a limited but continuous decrease. Similar observations are valid also for the propagation energy, with the only exception of alloy Ni 0.5. The as-cast condition presents for the alloy Ni 0.5 a higher value of propagation energy than the other alloys. After heat treatment, the alloy Ni 0.5 presents a significantly lower value than the as-cast one. Thus, the propagation energy trend after heat-treatment shows a maximum at 1.0 wt.% of Ni. The T6 heat-treatment determines a detrimental effect on the propagation energy only at the

lowest Ni content, while it does not present a significant influence as the Ni concentration increases.

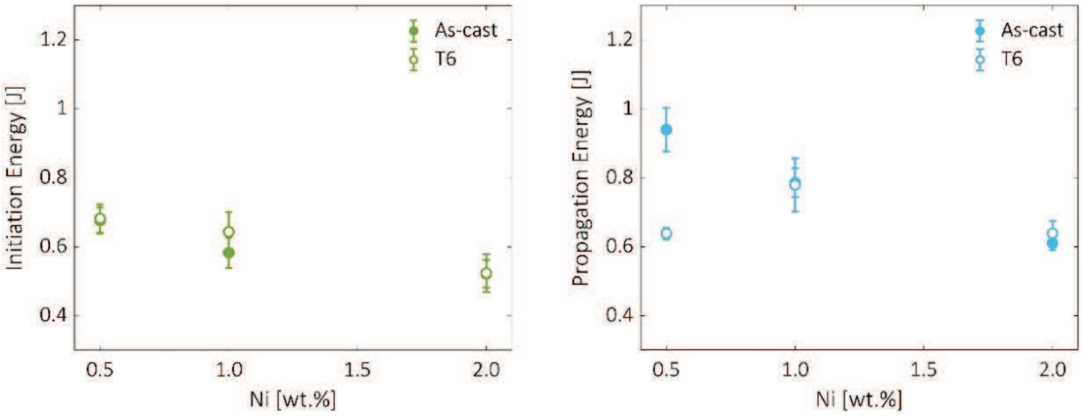

a) b)

Figure 4. 12 – Impact parameters as a function of Ni content: a) initiation energy and b) propagation energy

Figure 4. 13 depicts the principal features that characterise the fracture surface of impact specimens, in all the considered alloys. Cleavage of primary α-Al and debonding of Si particles are the main characteristics (Figure 4. 13a) and are equivalent to those observed on the fracture surfaces of tensile specimens (Figure 4. 10). Ni-based compounds appear fractured on the surface of cleavage planes (Figure 4. 13b), as evidence that the crack propagates across the brittle phases. Figure 4. 13c highlights the presence of narrow areas that contain a high number of small cavities that resemble ductile dimples. The EDS analysis does not detect a specific composition in these areas, that might be related to small gas porosities previously present in the sample. Shrinkage porosities also emerge on the surface, with the characteristic appearance of dendrite arm tips (Figure 4. 13d).

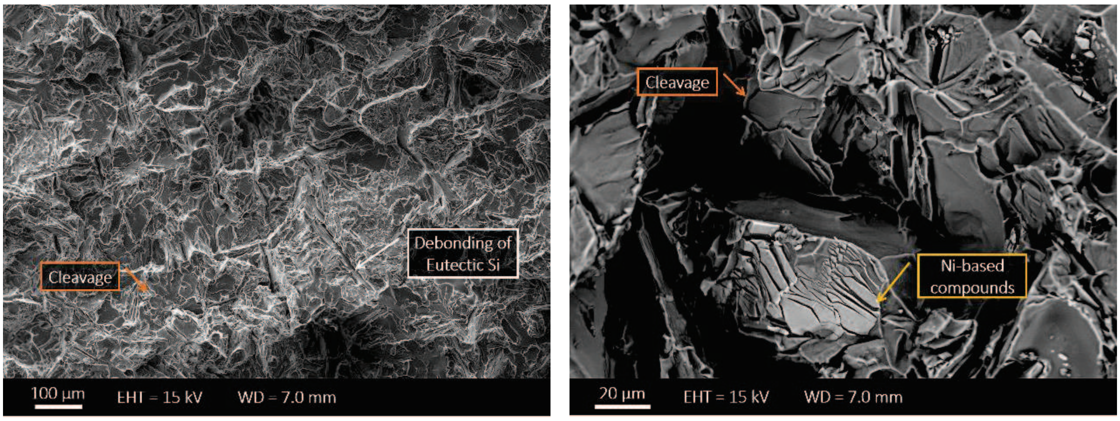

a) b)

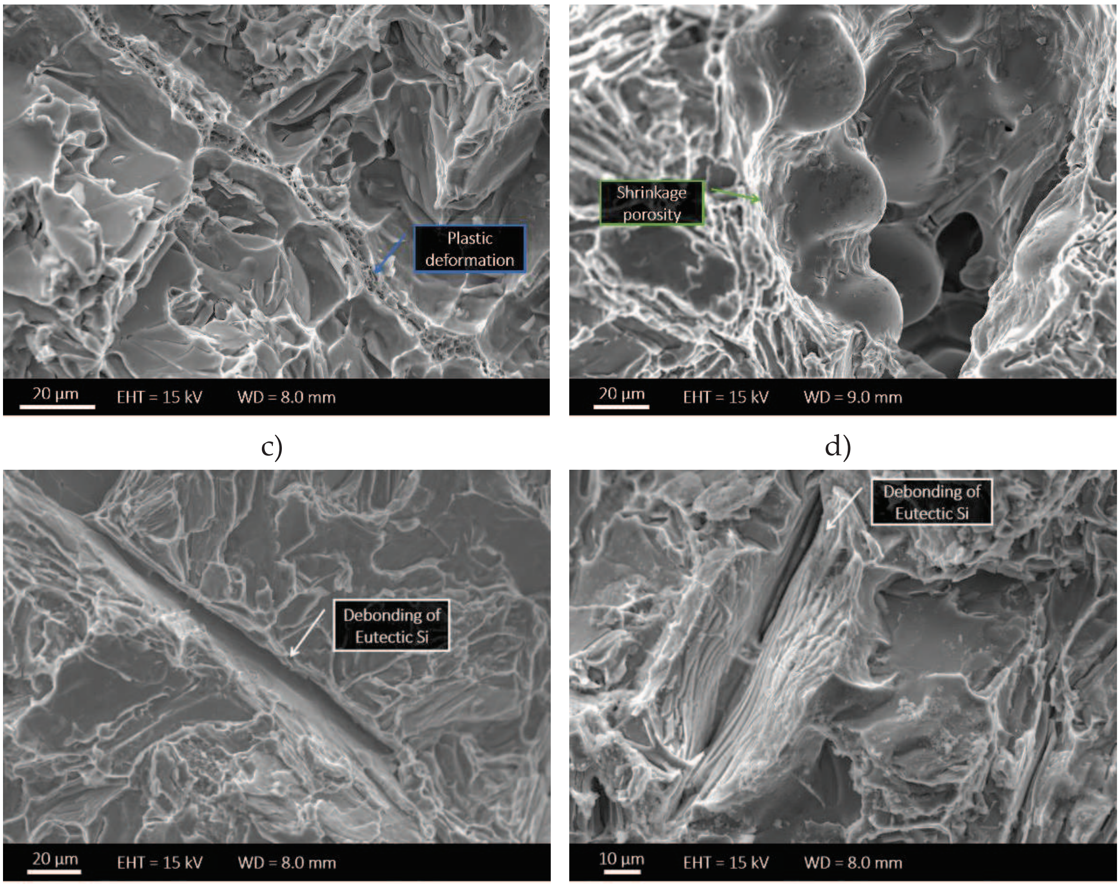

c) d)

e) f)

Figure 4. 13 – SEM images of fracture surfaces: a) cleavage and debonding features; b) fractured Ni-based intermetallic; c) small region of plastic deformation; d) shrinkage porosity; e, f) sites related to debonding of eutectic Si lamellae

Figure 4. 13e-f are close-up images of some debonding sites. In some cases, around the elongated cavity, where the Si lamella was located, the α-Al matrix appears deformed by the pull-out phenomenon that occurs during fracture. Some fragments of the Si lamella are retained in the cavity.

These observations lead to the conclusion that during crack propagation Si particles are preferentially debonded from the primary α-Al, while the Ni-based compounds result fractured. Despite thin regions that appear plastically deformed, the principal mechanism is a brittle fracture with large areas of cleavage.

4.5 DISCUSSION

4.5.1 As-cast condition

An Al-Si alloy can be considered as a composite material where the α-Al phase is the matrix that needs reinforcement, while the network of eutectic Si particles and Ni-based intermetallic compounds is the stronger phase acting as a reinforcement [5], [6], [13], [18]. When an external load is applied, there is a non-uniform distribution of stresses due to the different elastic properties of the matrix and the reinforcing phases. A load transfer occurs when the rigid phase network is continuous, and the matrix/reinforcement interface is significant. The rigid phase bears a large part of the load. Uggowitzer *et al.* [23] hypothesised that the continuity of the reinforcing phase improves as its volume fraction increases, up to an upper limit above which there is no more improvement of the network continuity. The addition of increasing quantities of Ni to the AlSi7Mg base alloy promotes the formation of Ni-based phases, and thus increases the volume fraction of the reinforcing phase.

Nevertheless, the trends depicted in Figure 4. 8 and Figure 4. 11 show that the resistance properties remain almost constant with increasing Ni content. YS and UTS are comparable with the value of the Ni-free AlSi7Mg alloy and, together with the peak force, remain almost constant as the Ni concentration in the alloy increases. This phenomenon relies on the fact that eutectic Si particles in the AlSi7Mg alloy already present good interconnectivity in the as-cast condition, as reported by Lasagni *et al.* [24]. Consequently, the addition of Ni does not determine an appreciable improvement in the bearing capability of the rigid reinforcing phase. The formation of an increasing amount of Ni aluminides does not exert any beneficial effect on the interconnectivity of the 3D network. Also, the phases that constitute the reinforcing network, eutectic Si and Ni phases, have a similar tendency to initiate and propagate the fracture [22], [25]. The increase of Ni content from 0.5 to 2.0 wt. % does not show a significant influence on the elongation (Figure 4. 8c), but it affects both initiation (Figure 4. 12a) and propagation (Figure 4. 12b) energies. The reason can probably be ascribed to the different role played by brittle phases in static and impact tests. In the first ones, the material can re-arrange and comply with the deformation, and this behaviour limits the deleterious effect of brittle phases. On the other hand, the impact tests exclude this possibility, and the presence of brittle compounds affect the mechanical response to deformation.

These considerations are consistent with fracture surface observations. Extended cleavage regions are evident on the fracture surfaces of as-cast alloys, both tensile (Figure 4. 10) and impact (Figure 4. 13) samples. The presence of several brittle phases and the lack of plastic deformation suggest that cracks initiate in brittle constituents, either eutectic Si or Ni-based compounds. The cracks can quickly propagate by cleavage of fragile phases or following the matrix/reinforcement interface. Furthermore, eutectic Si particles in the as-cast condition show a plate-like morphology that could easily originate a localised stress concentration region.

The equivalent diameter of Ni aluminides increases with the increasing Ni content from 0.5 to 2.0 wt % (Figure 4. 7a). The increased dimension of Ni-based compounds suggests enhanced interconnectivity of the reinforcing network, that improves the tensile properties. Nevertheless, the presence of Ni does not improve the connectivity of the 3D network, thus tensile (Figure 4. 8) and impact properties (Figure 4. 11) show an almost constant trend as Ni increases. For what concerns the SF, most of its values range from 1 to 3 for each Ni content (Figure 4. 7c), meaning that Ni particles show a similar morphology for the three investigated alloys. The potential stress concentration near intermetallic compounds is analogous in the alloys; thus, their detrimental influence on tensile properties is negligible. This phenomenon is another reason behind the trends of resistance properties (Figure 4. 8, Figure 4. 11).

The presented results indicate that in the as-cast condition fracture propagates either by cleavage through brittle phases, *i.e.* eutectic Si particles and Ni-based compounds, or by debonding of brittle phases from the α-Al matrix. The formation of a 3D network is not sufficient to determine an increase of tensile and impact properties of the alloys at room temperature.

4.5.2 Heat-treated condition

For what concerns the T6 heat-treated alloys, Figure 4. 8 and Figure 4. 11 show that Ni has an apparent detrimental effect on the resistance properties of the alloys. The composite material approach helps to explain the presented results. It relies on the mechanism of load transfer from the α-Al matrix to the reinforcement phases, as suggested by Moffat [25] and reproposed by Casari *et al.* [22]. This approach takes into account the empirical relation between hardness $H\ [GPa]$ and $UTS\ [MPa]$, reported in Equation (4. 1):

$$H = f(UTS) \tag{4. 1}$$

Besides, it assumes that rigid phases, as eutectic Si particles and Ni-bearing phases, have a linear elastic behaviour. Thus the deformation of fracture ε_{fr} can be expressed by Equation (4. 2):

$$\varepsilon_{fr} = f(UTS)/E \tag{4. 2}$$

where $E\ [GPa]$ is Young's modulus. Since an absolute relationship is not required, relative fracture strain $f(\varepsilon_{fr})$ results from Equation (4. 3), combining Equations (4. 1) and (4. 2):

$$f(\varepsilon_{fr}) = H/E \tag{4. 3}$$

Assuming homogeneity of the strain distribution for each phase, the values of H and E, found in literature and reported by Moffat [25] and Song *et al.* [26], can be used in Equation (4. 3) to determine the values of $f(\varepsilon_{fr})$, reported in Table 4. 3. Ni-rich compounds show a lower value of relative fracture strain compared to eutectic Si particles, and thus have a higher tendency to fracture.

Table 4. 3 – Values of H, E and related f(ε_{fr}) for eutectic Si and Ni-based compounds [26]

Phase	H [GPa]	E [GPa]	f(ε_{fr})
Eutectic Si	11.13	147.6	0.0754
T-Al_9FeNi	7.71	161.5	0.0477
ε-Al_3Ni	7.73 [26]	141.2 [26]	0.0548

These findings suggest the following fracture mechanism of the material: when the external stress is applied, the reinforcing network of eutectic Si and Ni aluminides bears the load. These phases show the highest tendency to fracture [22], leading to the formation of micro-cracks in the material. The specimen thus reaches YS for lower stress values. Furthermore, since micro-cracks can propagate without difficulty across brittle phases, the fracture rapidly propagates when there is high interconnectivity of the reinforcing 3D network. This phenomenon leads to the formation of extended de-cohesion regions that reduce the dimension of the resistant section. For this reason, UTS occurs at low-stress values.

In comparison with the mechanical properties of the heat-treated Ni-free AlSi7Mg alloy (Figure 4. 8), the addition of 0.5 wt.% Ni has a detrimental influence on the YS of the alloy since it yields a decrease of about 40 MPa due to the early fracture of brittle Ni-based compounds. Both the base AlSi7Mg alloy and the Ni 0.5 alloy exhibit a similar value of UTS. The Ni content does not maintain the 3D network after T6 heat treatment. Such loss of interconnectivity hinders the crack propagation by involving the more ductile α-Al phase in the fracture process, reasonably explaining the higher UTS average value than those of the alloys with 1.0 and 2.0 wt.% of Ni. In contrast, higher Ni concentrations limit the fragmentation and spheroidization of eutectic Si particles during T6 heat treatment [5], [6], [13], [18]. As a result, the 3D network maintains high levels of interconnectivity and fosters crack propagation through a much easier path. This phenomenon determines the low resistance values of both tensile (Figure 4. 8a,b) and impact (Figure 4. 11) properties. The decrease of YS and UTS is coupled with an increase of elongation (Figure 4. 8c), that remains in the range of 10 ÷ 12 % for the investigated Ni contents. This phenomenon clarifies that the decrease of mechanical strength is not related to a decrease of ductility, that can result from a higher concentration of brittle Ni compounds. Similar observations stem from the initiation (Figure 4. 12a) and propagation (Figure 4. 12b) energies, that have an almost constant trend with Ni increases and rule out the embrittlement due to Ni phases.

These hypotheses seem in line with fractographic observations of the alloys (Figure 4. 10). In Figure 4. 10b, the heat-treated alloy with the lowest Ni content presents not only cleavage regions and fractured brittle phases (mainly eutectic Si particles) but also plastic deformation of the α-Al matrix. On the other hand, in Figure 4. 10d and Figure 4. 10f a limited amount of plastic deformation can be detected, and it is possible to distinguish an increased number of either cleavage propagation or debonding sites.

Figure 4. 9 shows the detrimental effect of Ni content on the Vickers microhardness of the α-Al matrix after T6 heat treatment. The T6 heat treatment leads to the precipitation of the β-Mg_2Si phase in nanometric particles, which act as a reinforcement and increase the microhardness of the primary α-Al matrix. Nevertheless, microhardness is found to decrease with further Ni additions up to 2.0 wt.% (Figure 4. 9). This result mirrors the outcome of tensile and impact tests, and it indicates that the presence of Ni exerts a negative effect on the precipitation of reinforcing intermetallic compounds to some extent.

In summary, Ni aluminides cause a remarkable decrease in the room-temperature resistance properties and microhardness of the AlSi7Mg heat treated alloy. Even though the presence of Ni hinders the spheroidization effects of eutectic Si particles during T6 heat treatment, it also promotes the formation of a higher number of brittle phases that easily promote fracture propagation. On the other hand, the presence of Ni increases the percentage elongation in comparison with the Ni-free AlSi7Mg alloy, meaning that the presence of Ni-based compounds does not affect the ductility of the alloy.

4.6 CONCLUSION

As-cast specimens show a constant trend for resistance properties with increasing Ni content, as well as microhardness. Fracture surface characteristics and geometric parameters of Ni-based compounds suggest that fractures propagate either by cleavage through brittle phases or by debonding of such phases from the α-Al matrix. The three-dimensional network, composed of eutectic Si particles and Ni aluminides, is not sufficient to determine an increase of the mechanical properties of the alloys.

After T6 heat treatment, both tensile and impact properties exhibit a substantial decrease with increasing Ni content. On the other hand, elongation and both initiation and propagation energies have an almost constant trend with Ni content. Thus the decrease of resistance properties is not linked to the presence of brittle Ni-based compounds. The fracture mechanism involves cleavage and debonding of brittle phases and plastic deformation of the α-Al matrix in the alloy with 0.5 wt.% Ni. On the other hand, the crack propagation is increasingly characterised by cleavage and debonding at a Ni concentration up to 2.0 wt.%.

REFERENCES

[1] Z. Asghar, G. Requena, and G. H. Zahid, *Effect of thermally stable Cu- and Mg-rich aluminides on the high temperature strength of an AlSi12CuMgNi alloy*, Mater. Charact., vol. **88**, pp. 80–85, 2014

[2] F. Stadler, H. Antrekowitsch, W. Fragner, H. Kaufmann, and P. J. Uggowitzer, *Effect of main alloying elements on strength of Al-Si foundry alloys at elevated temperatures*, Int. J. Cast Met. Res., vol. **25**, no. 4, pp. 215–225, 2012

[3] D. Casari, F. Poli, M. Merlin, M. T. Di Giovanni, Y. Li, and M. Di Sabatino, *Effect of Ni additions on A356 alloy's microstructure and high-temperature mechanical properties*, Metall. Ital., vol. **6**, pp. 33–36, 2016

[4] A. J. Moffat, B. G. Mellor, I. Sinclair, and P. A. S. Reed, *The mechanisms of long fatigue crack growth behaviour in Al-Si casting alloys at room and elevated temperature*, Mater. Sci. Technol., vol. **23**, no. 12, pp. 1396–1401, 2007

[5] Z. Asghar, G. Requena, and E. Boller, *Three-dimensional rigid multiphase networks providing high-temperature strength to cast AlSi10Cu5Ni1-2 piston alloys*, Acta Mater., vol. **59**, pp. 6420–6432, 2011

[6] Z. Asghar, G. Requena, H. P. Degischer, and P. Cloetens, *Three-dimensional study of Ni aluminides in an AlSi12 alloy by means of light optical and synchrotron microtomography*, Acta Mater., vol. **57**, pp. 4125–4132, 2009

[7] P. K. Rohatgi, R. C. Sharma, and K. V Prabhakar, *Microstructure and Mechanical Properties of Unidirectionally Solidified Al-Si-Ni Ternary Eutectic*, Metall. Trans. A, vol. **6**, no. 3, pp. 569–575, 1975

[8] S. S. S. Kumari, R. M. Pillai, and B. C. Pai, *A study on the structural, age hardening and mechanical characteristics of Mn and Ca added Al-7Si-0.3Mg-0.6Fe alloy*, J. Alloys Compd., vol. **453**, pp. 167–173, 2008

[9] A. R. Farkoosh, M. Javidani, M. Hoseini, D. Larouche, and M. Pekguleryuz, *Phase formation in as-solidified and heat-treated Al-Si-Cu-Mg-Ni alloys: Thermodynamic assessment and experimental investigation for alloy design*, J. Alloys Compd., vol. **551**, pp. 596–606, 2013

[10] F. Meng, Y. Wu, K. Hu, Q. Sun, and X. Liu, *Evolution and Strengthening Effects of the Heat-Resistant Phases in Al-Si Piston Alloys with different Fe/Ni ratios*, Materials (Basel)., vol. **12**, no. 2506, 2019

[11] N. A. Belov, D. G. Eskin, and A. A. Aksenov, *Multicomponent Phase Diagrams*, Multicomponent Phase Diagrams, pp. 341–377, 2005

[12] C. Chen, A. Richter, and R. C. Thomson, *Investigation of mechanical properties of intermetallic phases in multi-component Al-Si alloys using hot-stage nanoindentation*, Intermetallics, vol. **18**, no. 4, pp. 499–508, 2010

[13] Z. Asghar, G. Requena, and F. Kubel, *The role of Ni and Fe aluminides on the elevated temperature strength of an AlSi12 alloy*, Mater. Sci. Eng. A, vol. **527**, pp. 5691–5698, 2010

[14] M. J. S. Mohamed, *Influence of Nickel Addition and Effect of Heat Treatment on Aluminium-Silicon Piston Alloys*, Int. J. Sci. Res., vol. **4**, no. 4, pp. 781–785, 2015

[15] N. E. Nwankwo, V. U. Nwoke, and E. E. Nnuka, *Effect of Ni-additions on the Microstructure and Mechanical Properties of Fe-based Chill-Cast Al-Si Alloys for Production of Pistons for Automobile Engine Applications*, Int. J. Sci. Res. Eng. Technol., vol. **1**, no. 2, pp. 21–24, 2015

[16] Y. Yang, K. Yu, Y. Li, D. Zhao, and X. Liu, *Evolution of nickel-rich phases in Al-Si-Cu-Ni-Mg piston alloys with different Cu additions*, Mater. Des., vol. **33**, pp. 220–225, 2012

[17] H. Yang, D. Watson, Y. Wang, and S. Ji, *Effect of Nickel on the Microstructure and Mechanical Property of Die-cast Al-Mg-Si-Mn Alloy*, J. Mater. Sci., vol. **49**, no. 24, pp. 8412–8422, 2014

[18] F. Stadler, H. Antrekowitsch, W. Fragner, H. Kaufmann, and P. J. Uggowitzer, *The Effect of Ni on the High-Temperature Strength of Al-Si Cast Alloys*, Mater. Sci. Forum, vol. **690**, pp. 274–277, 2011

[19] L. Fang, X. Zhang, H. Hu, X. Nie, and J. Tjong, *Microstructure and tensile properties of squeeze cast aluminum alloy A380 containing Ni and Sr addition*, Adv. Mater. Process. Technol., vol. **3**, no. 1, pp. 90–100, 2017

[20] J. A. Garcia-Hinojosa, C. R. González, G. M. González, and Y. Houbaert, *Structure and properties of Al-7Si-Ni and Al-7Si-Cu cast alloys nonmodified and modified with Sr*, J. Mater. Process. Technol., vol. **143–144**, pp. 306–310, 2003

[21] L. Lattanzi *et al.*, *Room temperature mechanical properties of A356 alloy with Ni additions from 0.5 Wt to 2 Wt%*, Metals (Basel)., vol. **8**, no. 224, 2018

[22] D. Casari, T. H. Ludwig, M. Merlin, L. Arnberg, and G. L. Luca, *The effect of Ni and*

V trace elements on the mechanical properties of A356 aluminium foundry alloy in as-cast and T6 heat treated conditions, Mater. Sci. Eng. A, vol. **610**, pp. 414–426, 2014

[23] P. Uggowitzer and H. P. Stuwe, *Plastizitat von ferritisch-martensitischen Zweiphasenstahlen*, Z. Met., vol. **73**, no. 5, pp. 277–285, 1982

[24] F. Lasagni, *Three-dimensional characterization of "as-cast" and solution-treated AlSi12 (Sr) alloys by high-resolution FIB tomography*, Acta Mater., vol. **55**, pp. 3875–3882, 2007

[25] A. J. Moffat, *Micromechanistic analysis of fatigue in aluminium silicon casting alloys*, University of Southampton, 2007

[26] J. M. Song, T. Y. Lin, and H. Y. Chuang, *Microstructural characteristics and vibration fracture properties of Al-Mg-Si alloys with excess Cu and Ni*, Mater. Trans., vol. **48**, no. 4, pp. 854–859, 2007

CONCLUDING REMARKS AND FUTURE DEVELOPMENTS

The present research set out to deepen the role of alloying elements and melt treatments on the microstructure of AlSi7Mg alloys. It is well-known that the microstructural features determine the mechanical response of the alloy, and it is fundamental to describe appropriately the treatments that lead to specific microstructures. This final section draws the concluding remarks and highlights possible future developments.

CONCLUDING REMARKS

Grain refining and fading

The study deepened the influence of holding time on the refining efficiency of AlTi5B1 rods and refining tab. The results highlight that the formers need a minimum activation time, but their refining efficacy remains constant up to 120 minutes of holding time at elevated temperature (~ 730 °C) in the ladle. The refiner tab determines after 10 minutes a significant level of grain refinement (AGS ~ 450 μm). Nevertheless, the average grain size increases with time, indicating that the beneficial effects of the refiner tab suffer a fading phenomenon.

Thermal analysis is a performing instrument that can substitute the microstructural analysis to assess grain refining. The efficacy of different grain refining products and conditions corresponds to specific changes in the thermal characteristics. These, in turn, mirror different grain dimensions, but they cannot be directly related to a numerical value of the grain size.

Sr interaction with alloying and trace elements

The addition of Ti, Mg and Cu to a binary AlSi7 alloy build up the most employed AlSi7Mg alloys. These alloying elements interact with the presence of Sr as a eutectic modifier. Mg and Cu increase the density of eutectic grains, and the eutectic Si particles result coarser than the ones in AlSi7 and AlSi7+Ti alloys at the same Sr content. The presence of Ti in the alloy does not determine ternary eutectic precipitation, unlike Cu and Mg. In the AlSI7+Ti alloy, the invariant Al-Si eutectic transformation is the last solidification event. Ti does not interfere with Sr modification mechanisms, and the morphology of Si particles is analogous to the one typical of the binary AlSi7 alloy.

The presence of limited amounts of Ca, less than 100 ppm, should not be underestimated in Sr-modified AlSi7Mg alloys. Even 40 ppm of Ca influence the precipitation of intermetallic compounds reducing the number of eutectic nuclei and the amount of Sr able to act as a modifier for Si particles. These phenomena affect modification, and the eutectic structure does not match the expectations.

Conversely, thermal analysis is not suitable to asses eutectic modification, especially when various alloying or trace elements are also present. The operator that is not aware of either the chemical composition of the alloy or the influence that each element of the alloy has on solidification can draw misleading conclusions from thermal analysis results. Thus, the observations related to the cooling curves have to be supported by micrographs to assess eutectic modification with a good grade of confidence.

Cu addition

The presence of Cu in the AlSi7Mg0.3 alloy lowers the solidification temperatures and leads to the precipitation of Cu-based intermetallic compounds. Besides, Cu strengthens the primary α-Al matrix via solid solution. These microstructural characteristics have a significant influence on the fatigue behaviour of the alloys. Crack propagation is trans-granular and trans-dendritic for Cu contents in the 0.5 ÷ 3.0 wt.% range. The strengthen α-Al matrix responds differently to deformation and hinders the stable propagation of the fatigue crack. Contrary to what expected, the presence of brittle Cu-based intermetallic does not control the crack path.

The DIC analysis based on a FIB milled pattern highlights the strained regions where crack can easily propagate, but in case of sudden failure, the software could not detect variations in strain regions.

Ni addition

The addition of Ni in the AlSi7Mg0.3 alloy determines the formation of Ni-based intermetallic compounds that nucleate in the same temperature range as the binary Al-Si eutectic. The interconnection between these constituents leads to the formation of a three-dimensional network that acts as a rigid reinforcement for the alloy. Since Ni limit the dissolution of Si during heat treatments, the reinforcing network gives excellent high-temperature resistance to the alloy and makes it suitable for applications that require such characteristics.

For what concerns room-temperature tensile and impact properties, as-cast specimens show a constant trend with increasing Ni content, as well as microhardness. Fractures propagate either by cleavage through brittle phases, eutectic Si and Ni-based compounds, or by debonding of such phases from the α-Al matrix. The 3D network is not sufficient to determine an increase of the mechanical properties of the alloys. After T6 heat treatment, mechanical properties exhibit a substantial decrease with increasing Ni content, while the ductility does not suffer from it. Fracture surface observations highlight a slight transition in the fracture mechanism as the concentration of Ni increases. Cleavage, debonding of brittle phases and plastic deformation of the α-Al matrix are the mechanisms in the alloy with 0.5 wt.% Ni, while cleavage and debonding occur more often with Ni concentration up to 2.0 wt.%.

FUTURE DEVELOPMENTS

In light of the topics faced during the PhD research work and the results presented in the present final thesis, promising future developments regard the Cu addition to the AlSi7Mg0.3 alloy in collaboration with the Jönköping University.

Since the addition of Cu to the alloy finds its reason in the subsequent heat treatment, it is fundamental to investigate the behaviour of the same alloys in the heat-treated condition, analogously to the research presented in Chapter 3. A behaviour similar to the alloy with 3.0 wt.% of Cu could occur with 1.5 wt.% of Cu after heat treatment, which determines the dissolution of intermetallic phases and the enrichment in Cu of the solid solution. Tailored heat treatments for the alloy with 0.5 wt.% of Cu can lead to an optimised microstructure, with a strengthened but yet not brittle primary α-Al matrix and a limited amount of well-dispersed Cu phases. Further investigations of heat-treated alloys will either clarify or contradict the present assumptions and will shed light on the topic. Also a more detailed investigation on the distribution of Cu atoms in the primary matrix is needed to clarify the role of Cu in influencing the crack propagation.

The FIB pattern employed in the present study comes from previous experiments on cast iron. The pattern for DIC can be optimised for Al alloys and down-sized to describe the strain field around sub-grain microstructural features, such as Si particles and Cu intermetallic compounds. Since the eutectic Si particles can constitute a built-in random pattern suitable for DIC, this procedure can become a valid alternative to avoid some drawbacks related to FIB milling. It results time consuming and can affect the surface of soft materials.